

EXPERIMENTAL AND NUMERICAL INVESTIGATION OF COAL
CLEAT IN LONGWALL MINES BASED ON
DISCRETE FRACTURE NETWORK ANALYSIS

A THESIS SUBMITTED TO
THE GRADUATE SCHOOL OF NATURAL AND APPLIED SCIENCES
OF
MIDDLE EAST TECHNICAL UNIVERSITY

BY

FIDAN JAFAROVA

IN PARTIAL FULFILLMENT OF THE REQUIREMENTS
FOR
THE DEGREE OF MASTER OF SCIENCE
IN
MINING ENGINEERING

MAY 2024

Approval of the thesis:

**EXPERIMENTAL AND NUMERICAL INVESTIGATION OF COAL
CLEAT IN LONGWALL MINES BASED ON
DISCRETE FRACTURE NETWORK ANALYSIS**

submitted by **FIDAN JAFAROVA** in partial fulfillment of the requirements for the degree of **Master of Science in Mining Engineering, Middle East Technical University** by,

Prof. Dr. Naci Emre Altun
Dean, **Graduate School of Natural and Applied Sciences** _____

Prof. Dr. Naci Emre Altun
Head of the Department, **Mining Engineering** _____

Assist. Prof. Dr. Ahmet Güneş Yardımcı
Supervisor, **Mining Engineering, METU** _____

Examining Committee Members:

Prof. Dr. Bahtiyar Ünver
Mining Engineering, Hacettepe University _____

Assist. Prof. Dr. Ahmet Güneş Yardımcı
Mining Engineering, METU _____

Assoc. Prof. Dr. Mustafa Erkayaoğlu
Mining Engineering, METU _____

Date: 28.05.2024

I hereby declare that all information in this document has been obtained and presented in accordance with academic rules and ethical conduct. I also declare that, as required by these rules and conduct, I have fully cited and referenced all material and results that are not original to this work.

Name Last name : Fidan Jafarova

Signature :

ABSTRACT

EXPERIMENTAL AND NUMERICAL INVESTIGATION OF COAL CLEAT IN LONGWALL MINES BASED ON DISCRETE FRACTURE NETWORK ANALYSIS

Jafarova, Fidan
Master of Science, Mining Engineering
Supervisor : Assist. Prof. Dr. Ahmet Güneş Yardımcı

May 2024, 106 pages

Fractures and joints are important structures that have a role in controlling rock behavior and its properties. In Longwall mines, coal cleats are having a great impact on stability and mechanical behaviors. By taking them into consideration during the modeling process of the rock samples, we can have more detailed and precise outputs regarding the parameters of a rock mass. DFN (Discrete Fracture Network) approach - described as a computational model that symbolizes characteristics of a fracture or fracture sets, is used to model geometrical properties of each individual fracture such as position, size, shape and direction. In our study, we performed the mentioned analysis method on coal-like material blocks with various 3D-printed joint networks. Later on, we implemented obtained test results to the field scale models. The cleat configurations differ in plane directions, network characteristics and connectivity types. Usage of mentioned technique in highly risked longwall mining - underground method for mining panel shaped coal deposits, can decrease the risk of failures and improve the stability. In this research, we compared different behavior of various internal joint network types in coal like material and their effect on stress conditions.

By that, the effect of coal cleats characteristics in longwall mines were studied and implemented to the larger scales by the application of DFN modeling of the samples.

Keywords: Coal Cleat, Longwall Mining, Numerical Analysis, Coal-like Material

ÖZ

UZUN AYAK MADENLERİNDE KÖMÜR KLİTLERİNİN AYRIK ÇATLAK AĞI ANALİZİNE DAYALI DENEYSEL VE SAYISAL İNCELENMESİ

Jafarova, Fidan
Yüksek Lisans, Maden Mühendisliği
Tez Yöneticisi: Dr. Öğr. Üyesi Ahmet Güneş Yardımcı

Mayıs 2024, 106 sayfa

Kırıklar ve yapısal çatlaklar, kaya davranışını ve özelliklerini kontrol eden önemli yapılardır. Uzunayak madenlerinde, kömür klitlerinin duraylılık ve mekanik davranışlar üzerindeki etkisi büyüktür. Bu etmenler göz önünde bulundurularak, kaya örneklerinin modellenmesi sürecinde kaya kütle jeomekanik özellikleri konusunda daha detaylı bilgiler elde edilebilir. Araştırma kapsamında çatlak ağı özelliklerini hesaplamalı modelleme çalışmasında temsil etmek amacıyla Ayrık Çatlak Ağı (AÇA) yöntemi kullanılmıştır. AÇA süreksizliklerin konum, boyut, şekil ve yön gibi geometrik özelliklerini modellemek için kullanılan bir yöntemdir. Bu yöntem 3D baskı yoluyla oluşturulan çatlaklara sahip kömür benzeri malzeme bloklarının modellenmesinde kullanılmış ve elde edilen sonuçlar saha ölçekli modelleremelere uygulanmıştır. Klit özellikleri düzlem yönleri, ağ oluşturma özellikleri ve bağlantı tipleri bakımından birbirinden farklılık göstermektedir. AÇA tekniğinin yüksek riskli uzun ayak madenciliğinde kullanılması, yenilme riskini azaltarak duraylılığı artırabilir. Araştırmada, kömür benzeri malzemedeki çeşitli çatlak tiplerinin farklı davranışlarını ve gerilim koşullarına etkileri karşılaştırılmıştır.

Böylece, uzun ayak madenlerinde kömür klitlerinin özelliklerinin kaya parametrelerine etkisi AÇA uygulaması ile saha ölçeğinde incelenmiştir.

Anahtar Kelimeler: Kömür Kliti, Uzun Ayak Madenciliği, Sayısal Çözümleme, Kömür Benzeri Malzeme

To all the women in my life,

ACKNOWLEDGMENTS

I would like to express my deepest gratitude to my supervisor, Assist. Prof. Dr. Ahmet Güneş Yardımcı, for all of his assistance, support, and profound dedication during this research project. His recommendations and encouragement have guided me throughout the challenging times and have significantly enhanced the quality of this work.

This work was funded by METU Scientific Research Projects Coordination Unit (ODTÜ Bilimsel Araştırma Projeleri Koordinasyon Birimi). I highly appreciate their assistance during the study.

I would like to express my gratitude to Prof. Dr. Bahtiyar Ünver and Assoc. Prof. Dr. Mustafa Erkayaoğlu, members of my thesis defense committee, for making my defense an amazing experience and for their helpful suggestions and comments.

I also want to thank Hakan Uysal for his invaluable assistance during the experimental stage of the study.

In addition, I want to express my deepest appreciation to my family members, especially to my mother and sister Aydan, for their priceless help, motivation, and moral support during this research project. Their belief in me have been a constant source of strength and inspiration.

Last but not least, I am grateful for my incredible friends Leyla Mammadova, Aytan Safarli, Nuray Damirchiyeva, Leyla Atakishiyeva, Eda Bahar Sarıbel and Ceyda Koca for their constant support and companionship.

TABLE OF CONTENTS

ABSTRACT.....	v
ÖZ.....	vii
ACKNOWLEDGMENTS	x
TABLE OF CONTENTS.....	xi
LIST OF TABLES	xiv
LIST OF FIGURES	xv
LIST OF ABBREVIATIONS	xix
LIST OF SYMBOLS	xxi
CHAPTERS	
1 INTRODUCTION	1
1.1 Research Motivation and Problem Statement.....	3
1.2 Research Objectives and Methodology	4
1.3 Contributions to the Literature.....	5
1.4 Structure of Thesis	6
2 LITERATURE REVIEW	7
2.1 Influence of Structural Discontinuities on Geomechanical Properties	7
2.2 Underground Coal Mining Regarding Structural Discontinuities	10
2.3 Geomechanical Modeling of Discontinuum	14
2.4 Mechanical Testing of Rock-like Materials.....	19
3 EXPERIMENTAL DESIGN AND PROCEDURES.....	29
3.1 Sample Preparation and Laboratory Tests	29
3.1.1 Blocked Structures	30

3.1.2	Complex Cubical Design.....	32
3.1.3	Angular Samples	34
3.1.4	Continuous Samples	35
3.2	Analysis of Experimental Outcomes	40
4	Numerical Analysis	49
4.1	Model Geometries and Construction.....	50
4.2	Modification of Input Parameters.....	53
4.3	Location of History Points and Execution of Simulations	55
5	RESULTS AND DISCUSSION.....	59
5.1	Analysis of Major Principal Stresses from the History Points Located Inside Coal Seam in Different Scenarios	59
5.1.1	Comparison of σ_1 Values Acquired from the History Point 5th_A from the Continuum and Discontinuum Models.....	59
5.1.2	Comparison of σ_1 Values Acquired from the History Point 10th_A from the Continuum and Discontinuum models	62
5.2	Analysis of Minor Principal Stresses from the History Points Located Above the Coal Slices (3 meters high on the immediate roof) in Different Scenarios.....	66
5.2.1	Comparison of σ_3 Values Acquired from the History Point 5th_B from the Continuum and Discontinuum models	66
5.2.2	Comparison of σ_3 Values Acquired from the History Point 10th_B from the Continuum and Discontinuum Models.....	70
5.3	Analysis of Minor Principal Stresses from the History Points Located Above the Coal Slices (center of the immediate roof) in Different Scenarios.....	73
5.3.1	Comparison of σ_3 Values Acquired from the History Point 5th_C from the Continuum and Discontinuum Models.....	73

5.3.2	Comparison of σ_3 Values Acquired from the History Point 10th_C from the Continuum and Discontinuum models.....	77
5.4	Analysis of Minor Principal Stresses at the Overburden and Deviatoric Stresses in Different Depths.....	81
6	CONCLUSIONS.....	85
	REFERENCES	89
APPENDICES		
A.	Analysis of Minor Principal Stresses from the History Points Located at Overburden (30 m high on the overburden) in Different Scenarios	103
B.	Analysis of Minor Principal Stresses from the History Points Located at Overburden (60 m high on the overburden) in Different Scenarios	105

LIST OF TABLES

TABLES

Table 3.1 Characteristics of different sample types	38
Table 3.2 Average values of obtained parameters for different sample types (data from extensometers)	41
Table 3.3 Axial/Lateral strain values(%) at failure moment (Extensometer versus Strain Gauge).....	47
Table 3.4 Lateral strain (%) at failure moment (Extensometer).....	48
Table 4.1 Elastic material properties assigned to the respective layers in discontinuum models.....	53
Table 4.2 Joint properties of discontinuities.....	53
Table 4.3 Modified material properties of coal layer in continuum models	55

LIST OF FIGURES

FIGURES

Figure 2.1. Schematic illustration of coal cleat geometries. (a) Cleat-trace patterns in plan view. (b) Cleat hierarchies in cross-section view (Laubach et al., 1998)	8
Figure 2.2. Schematic diagrams of three groups of numerical models: a) Numerical models with different cleat densities; b) Numerical models with different cleat quantities; c) Numerical models with different cleat angles. (Hou et al., 2020)	9
Figure 2.3. Categories of modeling and design approaches in rock mechanics problems (Jing and Hudson, 2002)	15
Figure 2.4. Original FDM apparatus drawing as presented by S. Scott Crump (Crump, 1992).....	22
Figure 2.5. Different arrangements to print specimens with different inclined angles (Fereshtenejad and Song, 2016).....	24
Figure 2.6. Process for preparing rock-like material sample (Tang et al., 2024) ...	26
Figure 3.1. (a) Printing stage of mold sides (b) connected version of molds (c) detachment of blocks from molds (d) comparison of fine and coarse blocks.....	31
Figure 3.2. (a) connectivity combination of coarse blocks in one layer (b) Coarse_BLL and Coarse_BLS samples	31
Figure 3.3. (a) bigger block constructed from the attachment of “layers” (b) Fine_BLL samples (c) Fine_BLS samples	32
Figure 3.4. (a) mold geometries (b) settled mixtures (c) respective pair of blocks (d) connected blocks	33
Figure 3.5. (a) bigger sized cubical block from which cylindrical samples were obtained, sample with fracture orientation of (b) 0°, (c) 30°, (d) 60°, (e) 90°	34
Figure 3.6. (a) cylindrical molds, (b) continuous samples.....	36
Figure 3.7. (a) samples LC_90, LC_0, Coarse_BLL, Coarse_BLS (from left to right) (b) samples HC_0, HC_90, HC_60, HC_30 (from left to right) (c) samples HC_C, LC_C, LC_30, LC_60 (from left to right) (d) samples Cubic, Fine_BLL, Fine_BLS (from left to right).....	39

Figure 3.8. (a) samples to which strain gauges were attached (b) sample Coarse_BLL with strain gauge attached to it (c) sample Fine_BLS with attached extensometers	40
Figure 3.9. Average Young Modulus (GPa) of experimental samples (from extensometer)	42
Figure 3.10. Average Poisson's ratio of experimental samples (from extensometer)	43
Figure 3.11. Average Uniaxial Compressive Strength (MPa) of experimental samples (from extensometer)	44
Figure 3.12. Average axial strain (%) at failure for different mixtures (from extensometers).....	45
Figure 3.13. Average lateral strain (%) at failure for different mixtures (from extensometer)	46
Figure 3.14. Axial strain values (%) of HC samples at failure (Extensometer versus Strain Gauge).....	47
Figure 3.15. Axial strain (%) of LC samples at failure (Extensometer versus Strain Gauge)	48
Figure 4.1. List of constructed 16 numerical simulations	50
Figure 4.2. Strata and model geometry of the Longwall Mine Simulation.....	51
Figure 4.3. Coal seams in discontinuum models with respective fracture orientation of (a) 0° (b) 30° (c) 60° (d) 90°	52
Figure 4.4. Dimensions of excavation zone divided into advancements of 10 m...	52
Figure 4.5. Modification of (a) E values (b) ν values for continuum models	54
Figure 4.6. History locations from (a) perspective view and (b) side view	56
Figure 4.7. (a) cutting planes of 5 th and 10 th panel slices (b) cross-sectional view of "nth" layer	57
Figure 5.1. Comparison of σ_1 values (Pa) from the history point located inside the 5 th coal slice (5th_A) in different discontinuous cases	60
Figure 5.2. Comparison of σ_1 values (Pa) from the history point located inside the 5 th coal slice (5th_A) in different continuous cases.....	61

Figure 5.3. Top view of maximum principal stress contours on the face of (a) 5 th and (b) 10 th coal slice in the discontinuum model having orientation of 60° (k=1)	63
Figure 5.4. Comparison of σ_1 values (Pa) from the history point located inside the 10 th coal slice (10th_A) in different discontinuous cases	64
Figure 5.5. Comparison of σ_1 values (Pa) from the history point located inside the 10 th coal slice (10th_A) in different continuous cases	65
Figure 5.6. Comparison of σ_3 values (Pa) from the history point located above the 5 th coal slice - 3 meters high on the immediate roof (5th_B) in different discontinuous cases	67
Figure 5.7. Comparison of σ_3 values (Pa) from the history point located above the 5 th coal slice - 3 meters high on the immediate roof (5th_B) in different continuous cases	69
Figure 5.8. Comparison of σ_3 values (Pa) from the history point located above the 10 th coal slice - 3 meters high on the immediate roof (10th_B) in different discontinuous cases	71
Figure 5.9. Comparison of σ_3 values (Pa) from the history point located above the 10 th coal slice - 3 meters high on the immediate roof (10th_B) in different continuous cases.....	72
Figure 5.10. Comparison of σ_3 values (Pa) from the history point located above the 5 th coal slice – the center of the immediate roof (5th_C) in different discontinuous cases	74
Figure 5.11. Comparison of σ_3 values (Pa) from the history point located above the 5 th coal slice – the center of the immediate roof (5th_C) in different continuous cases	76
Figure 5.12. Comparison of σ_3 values (Pa) from the history point located above the 10 th coal slice – the center of the immediate roof (10th_C) in different discontinuous cases	78
Figure 5.13. Comparison of σ_3 values (Pa) from the history point located above the 10 th coal slice – the center of the immediate roof (10th_C) in different continuous cases	80

Figure 5.14. Deviatoric stress (Pa) analysis of points with different depths (Continuum model with orientation of 60° and $k=1$)	83
Figure 5.15. Deviatoric stress (Pa) analysis of points with different depths (Discontinuum model with orientation of 60° and $k=1$).....	84

LIST OF ABBREVIATIONS

ABBREVIATIONS

3DP	3D Printed
BEM	Boundary Element Method
CAD	Computer-Aided Design
CBM	Coalbed Methane
CDEM	Combined Continuous-Discontinuous Element Method
Coarse_BLL	Blocked Samples with long-sided coarse blocks
Coarse_BLS	Blocked Samples with short-sided coarse blocks
DDA	Discontinuous Deformation Analysis
DEM	Discrete Element Method
DEM/DFN	Coupled Discrete Element Method and Discrete Fracture Network
DFN	Discrete Fracture Network
DLP	Digital Light Processing
EJRM	Equivalent Jointed Rock-mass Model
FDM	Fused Deposition Modeling
FEM	Finite Element Method
Fine_BLL	Blocked Samples with long-sided fine blocks
Fine_BLS	Blocked Samples with short-sided blocks
GSI	Geological Strength Index
HC	High Concrete Mixture Type
HC_0	High Concrete Samples Having Fracture Orientation of 0°

HC_30	High Concrete Samples Having Fracture Orientation of 30°
HC_60	High Concrete Samples Having Fracture Orientation of 60°
HC_C	High Concrete Continuous Samples (without any fractures)
LC	Low Concrete Mixture Type
LC_0	Low Concrete Samples Having Fracture Orientation of 0°
LC_30	Low Concrete Samples Having Fracture Orientation of 30°
LC_60	Low Concrete Samples Having Fracture Orientation of 60°
LC_90	High Concrete Samples Having Fracture Orientation of 90°
LC_90	Low Concrete Samples Having Fracture Orientation of 90°
LC_C	Low Concrete Continuous Samples (without any fractures)
Micro-CT	Micro-computed tomography
MJF	Multi-Jet Fusion
MTS	Material Testing System
PLA	Polylactic Acid filament
Q	Quality Index
RMR	Rock Mass Rating
SLA	Stereolithography
SLS	Selective Laser Sintering
UCS	Uniaxial Compressive Strength
UDEC	Universal Distinct Element Code

LIST OF SYMBOLS

SYMBOLS

k	Ratio of the horizontal stress to the vertical stress
E	Modulus of Elasticity
ν	Poisson's Ratio
σ_3	Minor Principal Stress
σ_1	Major Principal Stress
ε	Strain
m	meters
cm	centimeters
mm	millimeters
G	Shear Modulus
K	Bulk Modulus
Pa	Pascal
$^\circ$	Degree
R^2	The coefficient of determination

CHAPTER 1

INTRODUCTION

Coal - one of the most common fossil fuels on earth, has been essential to the production of energy for homes, businesses, and industries for centuries. Given that coal continues to be a significant energy source for our globe, its significance in the modern era is immeasurable. Coal cleats, also known as coal fractures or coal joints, are natural fractures that form within coal seams and are crucial for understanding how coal seams behave during mining operations. The development of those fractures is usually explained by factors such as the coalification process, thermal contraction, tectonic movements, sedimentary compaction, and other chemical/diagenetic processes. In basic terms, coal cleats are areas of weakness in the coal seam that allow fluids like water and gas to pass through. The angle or direction at which the cracks inside the coal seam are aligned is known as the cleat orientation. The coal seam's strength, permeability, and other characteristics are affected by the size of coal cleats, which can range from tiny fractures to more enormous fissures. Cleats are also important for coal excavation and quality of the produced coal as the particle size is influenced. Because they affect the stability of the coal seam, the effectiveness of extraction, and the safety of mining operations, coal cleats significantly impact mining techniques. For mining operations to be optimized and worker safety to be guaranteed, it is critical to comprehend the orientation, size, and distribution of coal cleats.

Longwall mining is still one of the main ways of extracting coal used worldwide. In-depth examination of the coal cleat structure is necessary to improve resource recovery, safety, and operating efficiency. The mentioned outcomes can be achieved by the detailed analysis of the mentioned cleat parameters because of their impacts

on stress distribution, face stability, development direction, yielding zones, and other topics.

When modeling the behavior of fractured and jointed rock masses, as those found in coal mining and other geological engineering applications, discontinuum modeling approaches provide a number of advantages. The DFN technique, which enables the study of stochastic fracture sets (random position, size, shape, and direction), was made possible by developments in computational geomechanics. Our goal in this study is to create an alternative testing methodology with a material that imitates coal and has cleat networks generated with the help of 3D Printing. The geomechanical properties and obtained experimental data trends will then be implemented in continuum and discontinuum numerical models at the field scale. Cleat setups containing various plane orientations, and connectivities will be compared regarding geomechanical behavior, stability issues at critical zones and mining direction. This research aims to improve our understanding of how cleat networks behave and affect the mechanical behavior of coal seams under longwall mining conditions by combining numerical models and experimental observations. Rather than employing the conventional continuum-based modeling approaches, discontinuum-based code will be used to examine the relationship between discontinuity characteristics and mechanical outputs. Also, accuracy of continuum modeling techniques will be tested in terms of representing behavior of fractured rock-like material. This study utilizes a multidisciplinary method that includes laboratory experimentation and numerical modeling to try and understand the complicated structure of coal cleat networks and their effects. More accurate and broad input parameters, which were acquired from the experimental part, enable us to analyze the mechanical processes within coal seams under various scenarios in longwall mines. As a result, relationships were obtained between coal cleat characteristics and coal seam behavior.

1.1 Research Motivation and Problem Statement

The main issue this study attempts to address is the lack of knowledge about coal cleat structure and how it affects longwall mining operations. Even after extensive studies on coal seam geology and mining methods, there is still insufficient information concerning the precise characterization and predictive modeling of cleat networks. Inadequate characterization, restricted predictive capability, safety and efficiency concerns are some of the main difficulties that arise from this information gap. The degree of accuracy and precision needed to fully capture the complex geometry and mechanical characteristics of coal cleat networks are frequently lacking from existing methods. The lack of a comprehensive understanding of coal cleat structure limits chances to optimize mining operations for increased efficiency and makes it more challenging to avoid safety threats, including roof falls, gas outbursts, and coal bursts. The face and the roof of a longwall mine are considered as two potential stress concentration zones. The existing computational models for simulating longwall mining processes frequently use oversimplified cleat network representations, which results in imprecise estimates of ground stability, gas migration patterns, and coal seam behavior.

The highlighted issues are mainly due to the disintegrating nature of coal material, which results in experimental inaccuracies. Additionally, not all distributions of coal cleat systems within the rock mass are accessible in nature for acquisition purposes of cylindrical samples by core drilling. This is particularly important for strength and deformability tests, which evaluate the elastic and plastic properties of rock materials and use those results in numerical simulations of mining operations. Also, because of the challenges mentioned above during the sample preparation stage, the outcomes of the simulations cannot be verified with real-life results. Therefore, in order to produce the best possible rock sample for mechanical tests, the sample preparation stage needs to be improved, or alternative methods need to be used.

1.2 Research Objectives and Methodology

By integrating numerical models and experimental data, this research aims to improve our understanding of how cleat networks behave and influence the mechanical behavior of coal seams under longwall mining circumstances. For that purpose, various methods for creating coal cleat networks with the utilization of 3D Printing and CAD environment were proposed, and later on, static deformability and uniaxial compressive strength tests were carried out on coal-like samples containing different cleat orientation, connectivity types, and sizes that imitate coal behavior. Two different mixtures containing various concentrations of cement, gypsum, coal ash, and water were poured into stochastically created fractured molds in order to compare strength patterns. As a result, a broad dataset, which includes geomechanical parameters such as UCS (Uniaxial Compressive Strength), Modulus of Elasticity, and Poisson's ratio, were obtained for the respective sample types. Results were compared, and later on, new relationships between the attributes of coal cleat networks, such as fracture orientation, cleat sizes, patterns, and respective outcomes of deformability tests, were found. Following this, acquired data was normalized and implemented to the real-life scaled numerical models of the longwall mine both in continuum and discontinuum mediums. Input parameters from obtained experimental data trends were used during the preparation of continuum models. By that, we were able to observe accuracy of the continuum techniques in terms of representing fractured materials and compare results to numerical outcomes of the discontinuum models. In order to simulate more accurate behavior of rock masses containing fractures or any type of discontinuities, the DEM/DFN method is used. Elastic analyses of different scenarios enabled us to obtain the relationship between the properties of coal cleat networks and the behavior of rock mass, more specifically, around the critical zones such as the face and roof. Undeniably, stress distribution in those zones is crucial during the safety assessment of mines. As a result, we can compare different scenarios and find the most effective advancing directions in terms of stability by examining stress-concentration zones, yielding

materials, and sudden changes during excavation stages in both continuum and discontinuum models. Therefore, an alternative technique for creating coal-like material was suggested in this paper, which allows us to examine the effects of coal cleat characteristics on the rock masses. Moreover, discontinuum-based code was used to verify those significant relationships in different longwall mine simulations and determine the safest and most efficient case scenario by comparing continuum and discontinuum models.

1.3 Contributions to the Literature

This study contributes to the literature firstly by offering a new approach to the creation of coal-like material in the laboratory environment. After testing out different 3D-printed stochastic patterns to imitate coal cleat structures, the most effective approaches are presented. Unlike other methods used for creating synthetic rock-like materials, utilized techniques did not include powder-based printing materials or roughly generated molds but focused on the generation of various fracture distributions that imitate coal behavior in more accurate and simplified ways. That enables us to obtain valid dependencies between the cleat characteristics and geomechanical parameters. As a result, we also contribute to the literature by comparing different longwall mine simulations that were constructed from real-life results with a broad range of input parameters. Another benefit of the proposed approach is that it directly predicts patterns of stress and deformation in the critical zones during longwall operations depending on the different cleat structures inside the coal seam. Also, limitations of the continuum techniques will be covered during the modeling of discontinuities. We believe that experimental and numerical studies in this work will contribute to both the theory and practice of coal mining by decreasing the risk of failures, improving production efficiency, and finding out the most effective approaches.

1.4 Structure of Thesis

This work involves total of six chapters and their roles will be shortly described in this part. The first chapter serves as an introduction point for the research by giving a short summary of the goals, methods, and contributions the study aims to have. It also covers the importance of the research problem in the field of mining engineering and emphasizes the necessity of the in-depth understating of coal cleat networks in underground mining operations. Additionally, the methodology, the scope of the work, and objectives are briefly reviewed in Chapter 1 as well. A critical review of the literature on coal cleat structures, the role of discontinuities in underground coal mining, and the testing of rock-like materials are some of the topics that were discussed in Chapter 2. The mentioned chapter also reveals gaps and limitations in the previous studies and offers the possible solutions that can be applied to the sample preparation stage of rock-like materials, as well as to the other stages of both experimental and numerical parts. The next chapter involves a detailed description of the preparation of samples, including the usage of CAD environment and 3D printing methods, experimental setups, and collected data. Chapter 3 also covers the discussion of outputs in the experimental part. Chapter 4 presents the application of the outcomes to the numerical longwall simulations using discontinuous-based code 3DEC. Moreover, how input paremeters were modified and models were constructed are the topics that were discussed in the same chapter as well. Discussion of the results and observations, understanding of the dependencies, and finding out the role of coal cleat structure in longwall mines by comparing continuum and discontinuum models are covered in Chapter 5. Finally, Chapter 6 summarizes the main conclusions, contributions, and outcomes of the study. The final chapter also provides suggestions for further development of the proposed techniques and approaches.

CHAPTER 2

LITERATURE REVIEW

The chapter on the literature review covers the wide range of research on coal cleat creation, behavior, and impacts on longwall mining operations. This study attempts to present a comprehensive understanding of the complex interactions between coal cleat formations and their effects on coal mining processes by looking at both experimental results and computational studies. The literature review also covers the influence of structural discontinuities on geomechanical properties, modeling of discontinuum, implementation of rock-like materials in studies, and other critical topics.

2.1 Influence of Structural Discontinuities on Geomechanical Properties

Fractures are the common structural features of geomaterials independent of the scale. The rock mass may exhibit discontinuities like joints, faults, or bedding planes, while mechanical microcracks or any mode of foliation like schistosity are available for rock material. A response of the rock mass to loading and unloading is anisotropic if it contains one or more sets of discontinuities. It is worth mentioning that the effect of that behavior can be observed during in-depth analyses of permeability, deformability, stability, strength, and other parameters of rock masses (Einstein et al., 1983; Chen et al., 2019; Ghazvinian and Hadei, 2012; Liu et al., 2021). Consideration of those discontinuities and their geometries can result in a more detailed understanding of rock mass behaviors and the acquisition of precise results.

Cleats are systematic small-scale discontinuities available specifically in coal. A particular cleat set often consists of two types of cleats: face cleats, which are dominant and generally produced initially, and butt cleats, which are orthogonal to the face cleats and into which they end. It is usually accepted that tectonic stress, fluid pressure, and intrinsic tensile force all contribute to the formation of cleats. Coal cleats may serve as naturally occurring weak points that facilitate coal extraction from the seam. Cleats can serve as passageways for gas, water, and other fluids, which may reduce pressure on the coal seam and facilitate mining. Additionally, their presence can improve ventilation and manage airflow in the mine. Coal cleats, however, can also cause difficulties in mining methods. They may produce unstable areas that make it challenging to preserve the integrity of the mine's walls and roof. Cleats can affect how the mining machinery functions, which can lead to roof and wall instability issues and ground control problems.

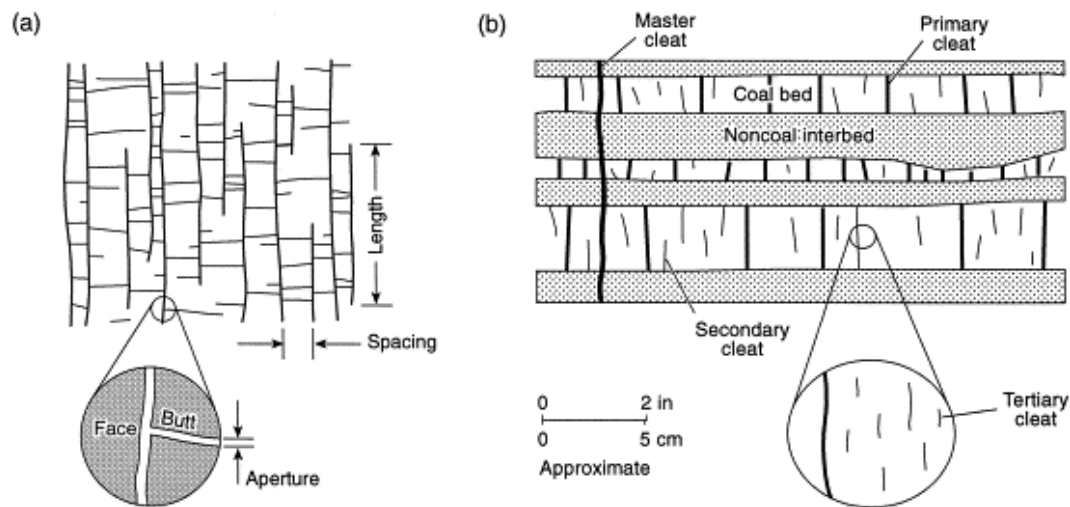


Figure 2.1. Schematic illustration of coal cleat geometries. (a) Cleat-trace patterns in plan view. (b) Cleat hierarchies in cross-section view (Laubach et al., 1998)

In their broad study, Laubach et al. (1998) illustrated coal cleat networks with detailed parameters such as (Figure 2.1); length – dimension which is perpendicular

to the fracture surface; height – vertical extension of opening parallel to the cleat surface and perpendicular to the bedding and aperture – width of opening that is perpendicular to the cleat surface. In addition to the mentioned characteristics, coal cleats can also be described with the spacing between them, developed frequency, mineralization along the opening, and other parameters.

The interrelationship between the coal cleat spacings, sizes, and shapes of cleat systems leads to the grouping of fractures depending on their connectivity types, distributions, and orientation. By comparing numerically established specimens with different cleat distributions, Cheng et al. (2021) determined that the strength of inhomogeneous coal specimens vary depending on the distribution angle of cleats. Also, an increase in the complexity of the coal cleat system results in a change in the geomechanical properties, such as a decrease in the values of Young’s modulus and the UCS of coal (Hou et al., 2020). Zhao et al. (2019) investigated the anisotropy of coal under uniaxial compression using both experimental and numerical techniques. They came to the conclusion that the directional distribution of microstructures affects the anisotropy of coal strength. The face cleats have a stronger impact on the mechanical qualities than the butt cleats, and bedding planes directly govern the coal's uniaxial compressive strength.

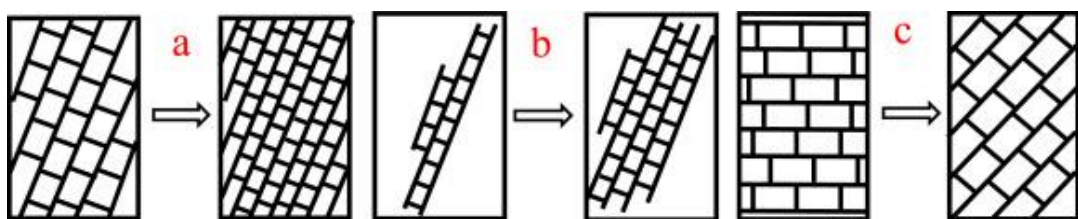


Figure 2.2. Schematic diagrams of three groups of numerical models: a) Numerical models with different cleat densities; b) Numerical models with different cleat quantities; c) Numerical models with different cleat angles. (Hou et al., 2020)

Comprehension of the natural fracture distributions and connectivities inside coal seams, which regulate natural coal permeability and, consequently, methane gas

deliverability, enables a deeper understanding of cleat trends and correlations. Generally speaking, the more the cleat density and size, the higher the permeability. Thus, in-depth analysis of cleat patterns and relationships has a massive role in the prediction of permeability, hydromechanical reactions, and stress-loading mechanisms throughout coal mining activities. Dawson et al. (2010) indicated that more precise predictions of cleat density and coal permeability can be made by knowing the relationship between cleat height and spacing for certain coals and the exact types of cleats within those coals.

Exact phenomena have been brought up in numerous studies, and more exact correlations were introduced. A finite element model by Cao et al. (2021), which can simulate the deformation of coal matrix, the shearing and dilatancy of coal cleats, the variation of cleat aperture, and shear and tensile-induced damage, was used to model the geomechanical and hydrological behavior of the fractured coal under various stress loading conditions. According to their results, coal mining at low-stress rates improves the stability of nearby coal seams and is preferable to coal mining in the same direction as the cleats. When it comes to the complex relations, Xu et al. (2016) showed that as stress increased, coal permeability and porosity decreased exponentially and linearly, respectively. While at greater stress levels, internal crushing and mechanical degradation would cause permanent changes to both porosity and permeability. It was also suggested that variations in fracture style, including the ones from opening-mode fractures to faults, may have an impact on cleat permeability in addition to size, intensity, and diagenetic variations as well (Laubach et al., 1998).

2.2 Underground Coal Mining Regarding Structural Discontinuities

Considering that structural features significantly impact the mechanical properties of rocks, in-depth study of discontinuities are unavoidable in underground coal mining and strata control. A comprehensive mine plan considering the relationship between the attributes of the mentioned discontinuities and mining direction has the potential

for effectively managing induced stress concentrations around crucial zones, which otherwise may result in instability problems. There have been numerous studies to investigate the effect of discontinuities such as faults and folds, which can lead to roof instability and pillar failure cases.

Previous numerical investigation by Wu et al. (2020) has shown that the probability of a fault activation increases with the increase in fault dip angle. Dynamic disasters such as rock bursts, mining earthquakes, bracket pressure, and others are more prone to occur on high dip faults. Prior physical studies have been conducted to assess the response of faults as mining operations were taking place (Wang et al., 2018; Jiang et al., 2019). A previous study by Jiang et al. (2019) has emphasized that while the hanging wall's overlaying structure is stable and fault activation is not easily observed, the footwall's fault activation is violent and somewhat active, increasing the danger of rock burst on the footwall relative to mining on the hanging wall. Similar outcomes were brought up by Wang et al. (2018), the cutting-down strata are compacted and slide along the fault plane after passing the fault. This can put a load on the hanging wall coal and increase its abutment stress; nevertheless, the hanging wall strata only move slightly in relation to the footwall.

A large number of existing studies in the broader literature have examined the distribution of stresses along the working face, roadway, and other critical zones as well (Zhou et al., 2023; Ma et al., 2011). Particularly, asymmetric distributions were seen in the plastic zone and stresses, and the closer the working face was to the fault, the greater the shear stress measured in the fault zone. Briefly, the existence of faults affects the deformation and movement of overburden strata and leads to asymmetry in stress, and displacement variations as well.

It is undeniable that faults and other discontinuities in longwall mining can lead to various instability and failure events. Weak zones may be created in the longwall panel's floor and roof by faults from which sudden collapses could occur. Also, such types of discontinuities may affect the stability of the pillars left between longwall panels. Stress concentrations around faults can lead to the deformation of the pillars.

Furthermore, issues such as subsidence on the surface, equipment damage, and gas outbursts can be related to the existence of faults.

A physical test by Wang et al. (2019) which was carried out with two fault structures, shows that more focus should be placed on the impact of overlaying strata movement above goaf between two faults because of the possibility of a rapid stress change during coal mining face excavation due to the extremely collapsed strata between the two faults. A similar numerical examination of the impact of several graben fault characteristics on rockburst potential reveals that none of them have a linear relationship with the magnitude of either static or dynamic stress (Cao et al., 2021). When the fault throw is between 6 and 8 m, the fault dip is greater than 65° , the mining height is greater than 6 m, and the coal pillar width is less than 50 m, it is observed that the longwall face has the largest risk of rock burst. This study proves the benefits of the numerical modeling one more time, as such accurate range of outcomes could not be observed with a physical models.

It is worth attention that the above-mentioned detailed outcomes were mostly obtained for the rock masses with moderately bigger discontinuities, such as folds, faults, and macrocracks. There remain key questions that are still not discussed in the literature about the more accurate effect of micro cracks or coal cleats with varying parameters. It is undeniable that coal cleats have a great impact on the stability of underground longwall mines. The mentioned method is a highly efficient underground mining method used to extract coal from deep seams or beds that are too thick for traditional mining methods. In longwall mining, stress is a crucial component since it can affect the stability of the mine and the safety of the employees. Stress in longwall mining is caused by the weight of the soil and rock above as well as by the removal of coal from the seam. The roof and walls of the mine may result in deformation or even collapse as the stress distribution in the rock surrounding it changes due to the removal of coal. In this technique, stress concentrations and deformations are highly associated with orientational and positional relationships of cleat networks and the mining direction (Song et al., 2021).

Longwall mining is an underground mining technique that is very effective in extracting coal or sedimentary deposits from the Earth's interior. It works especially well in the extraction of large, thick coal seams. Using this method, a panel or "longwall" of coal is completely extracted along a continuous face that can extend for hundreds of meters. Stress is one of the key factors that control stability in underground longwall mines (Durucan and Edwards, 1986; Meng et al., 2016; Yavuz, 2004). The role of coal cleats is undeniable in the distribution of stress and other parameters. Cleat orientation, size, and shapes that define zones for stress release, planes of weakness within coal seam, and influence the stability of roof support can be given as examples of this impact. Thus, the characteristics of coal cleats are crucial and should be taken into consideration during the design, excavation, and other steps of the mine cycle.

As the longwall mining method can result in geological disruptions and highly risky failure events, several authors have performed modeling of coal cleats and coal behaviors. For example, Song et al. (2017) researched stress and displacements in a typical longwall face. Their results showed that most of the failures occur at the roof of the opening, while most horizontal displacement occurs at the face, and most vertical displacement occurs near the roof of the coal face. It was also recognized that in some coal fields, the orientation of the face cleat in relation to the horizontal stress orientation affects the maximum coal seam permeability (Brook et al., 2016). As the excavation advances, redistribution of parameters in the zone nearest to the mining face, such as pore pressure and vertical and horizontal stress, could result in tensile failure if the permeability of coal is poor. A zone that may experience overpressure and desorption-induced energy failure may be observed ahead of the face in this case (Wang et al.,2013).

There have been numerous studies to investigate the effects of coal cleats on permeability and gas flow (Wang et al., 2021; Guo et al., 2012; Noack, 1998; Wang and Park, 2002). However, a closer look at the literature on this topic reveals a number of gaps, such as the usage of mostly numerical mediums and the lack of verification of real-life observations. Also, the influence of coal cleats in Longwall

mines on stress distributions, deformation, and failure states with physical sample verifications remains briefly addressed in the literature.

2.3 Geomechanical Modeling of Discontinuum

The safety, stability, and efficiency of mining operations heavily rely on accurately modeling the discontinuities present in the mining process. An in-depth comprehension of their impact is essential in the complicated mining environment, where excavations navigate through rock masses having a variety of discontinuities, including joints, fractures, and faults. Jing and Hudson (2002), in their broad review study on Numerical methods in rock mechanics, evaluated the most used numerical approaches of their time and categorized them into several groups by their purpose of usage (Figure 2.3). In general, the main types of numerical methods are Continuum, Discontinuum, and Hybrid methods. As our main interest in this study is the analysis of discontinuities, we will focus on the brief review of discontinuum methods - the ones that are utilized for modeling individual particles, fractures, or other discontinuities in the material. These techniques work effectively for modeling the behavior of materials in which the existence and interaction of discrete elements have a major impact on the reaction as a whole. Additionally, since then, newer hybrid techniques with the capability of solving more complex problems have been introduced, too.

The modeling technique should depend on the interrelationship between the fracture density and the model scale. Where fractures have a fine density so that no unique discontinuity exists to dominate the mass properties, the continuum approach is reasonable (Hosseini et al., 2021). Contrary to this, discrete methods require an explicit representation of the geometry and properties of discrete fractures. DEM technique, which was proposed by Peter A. Cundall and Otto D. L. Strack in 1979, is used to describe the mechanical properties of a rock on a scale of particle motion. They also describe the method as a numerical way that is used to monitor the interaction between particles and model their motion using an explicit numerical

scheme. To solve more complex problems, several other types of mentioned techniques have also been introduced since then: Generalized DEM (Williams et al.,1985), DDA (Shi, 1992), and others.

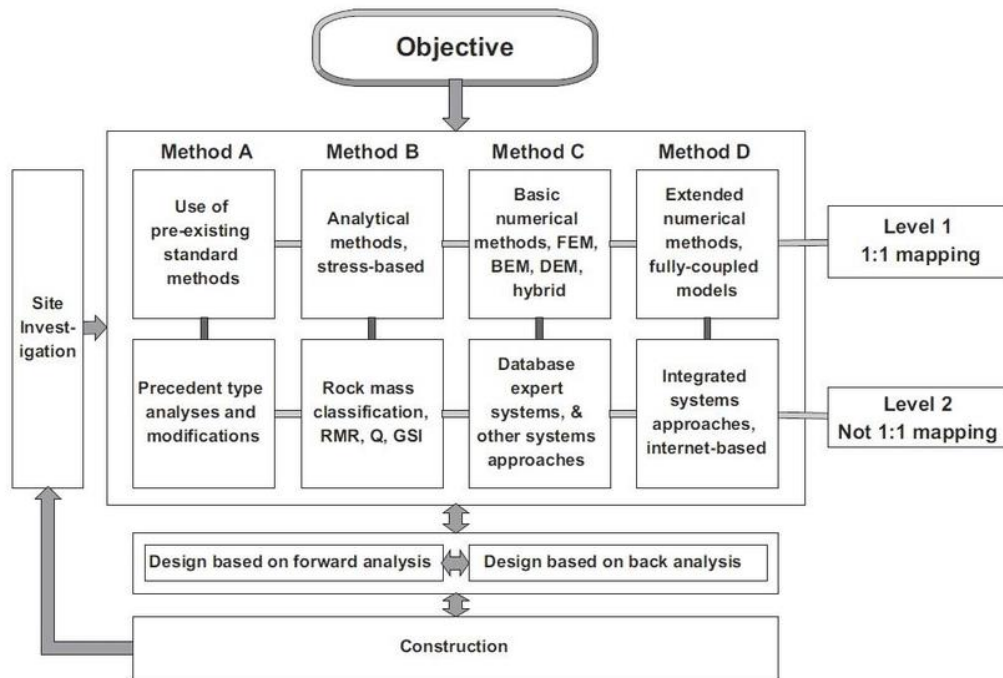


Figure 2.3. Categories of modeling and design approaches in rock mechanics problems (Jing and Hudson, 2002)

For safe and efficient production cycles in underground mines, accurate representation of fractures and cracks is crucial. Underground mining is a complicated and dangerous industry that highly depends on the selection of methods and equipment that aim to protect workers, maximize resource recovery, and follow laws and regulations. Numerical modeling is one such essential tool. The role of numerical modeling in safety assessment, stability analysis, support system optimization, mine planning, resource recovery, and environmental impact assessment is undeniable. Because of this reason, there have been numerous studies to investigate the effect of different factors numerically. The integrity of

underground structures in mining operations is largely dependent on the stability of rock masses. By taking into consideration ground conditions, support systems, and geological discontinuities, numerical modeling makes thorough stability studies easier.

A number of authors have recognized the limitations of the usage of certain discrete modeling techniques, so they proposed combined or hybrid approaches for assessing more complex cases. In order to assess the progression of the tunneling-induced fractures, the notable concentration of stress and compression deformation at the top of the rock roof and the bottom of the rock floor was computed efficiently by the application of CDEM models established by Ju et al. (2019). Shreedharan et al. (2016) performed a stability study on tunnels in the deep coal mines by utilization of 3DEC distinct element code. The results showed that rock mass cohesion, tensile strength, uniaxial compressive strength, and elastic modulus values, according to the back-analysis, are roughly 35–45% of the equivalent intact rock property values. Also, higher stability was achieved by the application of longer supports and floor bolting. Another hybrid method, EJRM, was applied to simulate the strata and surface movement in the Yanqianshan iron mine caused by mining under an open pit final slope (Xu et al., 2016) in order to better understand the failure mechanism of a roadway driven alongside an unstable goaf. An original numerical approach was presented by Gao et al. (2014), which combines a UDEC Trigon approach for simulating roadway damage with synthetic rock mass (SRM) modeling to get rock mass parameters. The use of DFN and DEM methods in mining is not limited only to rock and fracture analyses; they are also preferred when modeling mining equipment. Another branch in which the usage of numerical simulations is beneficial is mineral processing. Discontinuum modeling techniques greatly enhance the industry's capacity to function effectively, cut costs, and make well-informed decisions by optimizing comminution processes, improving material handling, enhancing separation efficiency, and resolving wear and maintenance issues (Zhao et al., 2020; Van Nierop et al., 2001; Quist and Evertsson, 2016).

The concept of DFN was firstly introduced by Long et al. in 1982 for solving numerical 2-D problems related to the flow fields in the fractures. They proposed that the technique has the potential to distinguish between two types of fractured systems: those that can be handled as a porous medium and those that must be treated as a collection of distinct fracture flow channels. Later on, more complex 3-D problems were analyzed (Long et al., 1985) and this approach was integrated into the simulations of the fluid flow (Andersson et al., 1987; Smith et al., 1984; Elsworth, 1986). Commonly, for DFN simulations, the aperture or transmissivity of a single fracture is either taken as constant or stochastically distributed (Moreno et al., 1988; Dershowitz & Einstein, 1988). Coupled DEM-DFN fracture mechanisms were applied to both laboratory-scale models (Karami and Stead, 2008) and to the large-scale rock masses as well (Elmo et al., 2011). One of the recent approaches is the application of coupled techniques to examine the response of tunnel excavation in jointed rock masses (Wang and Cai, 2020). The model uses equivalent continuum properties to represent small fractures implicitly, while only large and small fractures are explicitly considered in areas that are highly affected by excavation. The study also has shown that a few large fractures can be included in the model far from the tunnel boundary, depending on its location. By comparing the elastic continuum models and various DFN simulations with similar fracture characteristics, Min and Jing (2004) indicated that the equivalent mechanical properties may also provide a similar stress distribution. More detailed research was conducted as well in order to examine the nucleation and clustering behavior of rocks. Lavoine et al. (2020) observed the fracture size-position dependency in stress-induced samples, where small fractures are in connection with large fractures.

DFN (along with hybrid methods) is widely used in the mining industry for numerous purposes. Parameters that can affect stress distribution and propagation have been of interest in recent years. For example, induced stresses due to mining activities and stages of failure mechanisms were studied by Zhao et al. (2016). The DEM approach enabled them to model the pre-failure deformation characteristics and patterns. As a result, mining-induced rock movement was divided into four

stages: acceleration stage, constant movement stage, rapid movement stage, and deceleration and deposition stage. Another concept that was investigated in depth is the flow of fluids in the coal fractures as fracture systems in coalbed methane reservoirs control fluid transport properties in a fundamental manner. A model by Ma et al. (2020) shows that fluid behavior is affected by density, orientation, and fracture connectivity. Overall, the discrete fracture models allow us to study coal behavior in terms of different aspects more precisely and visualize bigger-scale environments in a more efficient way.

A solid understanding of the geological characteristics affecting coal extraction is necessary for the complex mining activities that take place in coal seams. Naturally occurring cracks found within coal seams, known as coal cleats, are one of these properties that are essential. Modern mining engineering is based on the fundamental application of numerical modeling to imitate the behavior of coal seams. Distinct research that is worth mentioning covers the relationship between the directional characteristics of cleats and coal bed methane exploration in the southeastern part of the Jharia Coalfield, India (Paul & Chatterjee, 2011). According to their analysis of maximum principal compressive horizontal stress direction, it is essential to have an in-depth understanding of cleat systems and how they relate to the stresses that are present close to the wellbore when choosing the best finishing technique for CBM wells. Meng et al. (2011), in their research about the Southern Qinshui Basin, pointed out that reducing cleat deformation may guarantee that the cleats and coal matrices are connected, allowing the coal matrices to transfer gas pressure to the cleats to maintain the cleat space. Cleats of different angles, different quantities, and combinations were compared numerically by Cheng et al. (2021), and they came to the conclusion that, whereas the failure mode of along cleats is easy to appear at the middle face cleat angles (45° ~ 75° , notably 60°), the failure mode of through cleats is easy to appear at the comparatively small or big face cleat angles (0° , 30° , and 90°). Furthermore, the strength of the specimens increases initially and subsequently diminishes with a turn at 60° with an increase in cleat angle. Using the UDEC Trigon method, the impact of pre-existing discontinuities on the strength of coal masses and

energy release under uniaxial compression was investigated by Vardar et al.(2019). The total energy release and the number of cleats per sample width were shown to have a nonlinear relationship, which suggests that as cleat density increased, failure intensity and energy release decreased.

As can be observed, there is no extensive research on the effect of coal cleat properties and there remains to be a research gap. Advances in computational DFN technique that allow for the investigation of stochastic fracture sets (random position, size, shape, and direction) and their verification with real-life outcomes will be the main interest of this research.

2.4 Mechanical Testing of Rock-like Materials

It is frequently necessary for researchers to replicate real-world rock formations or investigate particular geological processes in a controlled setting. Experiments and simulations are performed with synthetic rocks that resemble real-life rocks, which may not be possible with genuine rocks due to their nature, rareness, composition, or other factors. Materials that resemble artificial rocks can be designed to have particular qualities, which makes them perfect for testing and analysis in laboratories(Gell et al., 2019; Zhang and Zhao, 2013). This makes it possible for scientists to study these materials' mechanical, thermal, and chemical properties in controlled environments. Materials that are synthetically made to resemble rocks are frequently used in the mining industry as well in order to study the characteristics, fragmentation, and behavior of materials under different conditions. The mentioned application contributes to the enhancement of safety precautions, resource extraction efficiency, and mining process improvement. Further examples of their benefit include imitation of different geological conditions for material testing and equipment calibration, controlled environment for training development, simulation of safety challenges, and so on.

When it comes to our area of interest – coal samples, discrepancies in coal sample preparation due to the easily disintegrating nature of coal material impose experimental inaccuracies and lead to material loss. Commonly used cylindrical samples are prepared by core drilling and surface grinding techniques that may heavily disturb the mechanical properties of samples. This is even more critical for strength and deformability tests in which elastic and plastic rock material properties are determined and used in numerical simulations of mining activities. Other challenges resulting from the nature of rock can be moisture absorption, difficulties in handling, and safety concerns. Because of the above-listed reasons, the usage of an artificial material that imitates the properties of coal will be more beneficial in terms of efficiency and accuracy. Referred issues in the coal sample preparation were also observed during the experimental studies of other materials. That being the case, the application of numerous methods for the creation of rock-like materials was reported in the literature.

The methods that aid the creation of rock-like materials include but are not limited to mixing and casting, foaming and solidification, 3D printing, approaches including the usage of polymers, and others. While reviewing the literature, it can be seen that the mixing method is applied broadly in the studies where fracture and joint behaviors are examined. A research of Zhang et al. (2013) takes the attention on understanding of shear deformation, failure, and energy dissipation of joints in the artificially created samples from a mixture of lime, sand, and water with three kinds of artificially created joint surfaces. Results of direct shear tests in both numerical and physical medium showed that the distribution of microcracks, particularly tensile microcracks, and the concentration of compression stress are in good agreement, which is consistent with the production of compression-induced tensile cracks. One of the most detailed studies on this topic was done by Song et al. (2021) using 3DEC numerical modeling software. They have analyzed the influence of joint connectivity ratios and joint spacing from the experimental data of coal-like physical samples and the results of the numerical model. It was observed that maximum face displacement was decreased when both face-cleat angles and cleat spacing were increased. In the

work by Tang and Wong (2015), the fabrication of the joints was achieved by replicating the joints that were originally created to represent splitting rock blocks by the application of the Brazilian indirect tensile test technique. Different roughness parameters were tested, which were controlled by the proportions of cement, sand, and water. Results showed that for softer material interfaces, the shear behavior of rock joints was affected by the loading rate during direct shear test results. The normal loading rate increased, and the peak shear strength decreased.

Techniques that involved the preparation of whole cylindrical specimens was also used by numerous authors, for example in the study by Huang et al. (2015). Cement, quartz sand, and water were mixed for the creation of specimens with two unparallel fissures, which were generated by inserting steel during the molding stage. Rock-like material used in their study showed physical mechanical properties and failure modes that were consistent with brittle rock materials.

In the field of rock mechanics, additive manufacturing, or 3D printing, has various advantages. Since its beginnings in the 1980s, additive manufacturing, commonly known as 3D printing, has undergone substantial development. Rapid prototyping was the original use of 3D printing, but it has since spread to a number of sectors, including rock mechanics, aircraft, healthcare, and the automotive industry. The first technology to enable the layer-by-layer construction of three-dimensional objects by employing ultraviolet light to cure photopolymer resin, stereolithography (SLA) was developed by Charles Hull in 1984. This innovation laid the groundwork for the development of 3D printing (Hull, 1986). SLA established the groundwork for later advancements in the industry. Using a heated nozzle to extrude thermoplastic material, Scott Crump invented (Figure 2.4) fused deposition modeling (FDM) in 1989. The process deposits the material layer by layer (Crump, 1992) and prototyping, low-cost manufacturing of functioning parts are all common uses for this technique in a modern world. Other methods such as Selective Laser Sintering (SLS), Digital Light Processing (DLP), Multi-Jet Fusion (MJF) were also proposed afterward. While SLS technique involves usage of a laser to fuse particles together

to form solid layers, DLP method works by projecting each layer as a single picture and curing complete layers at once.

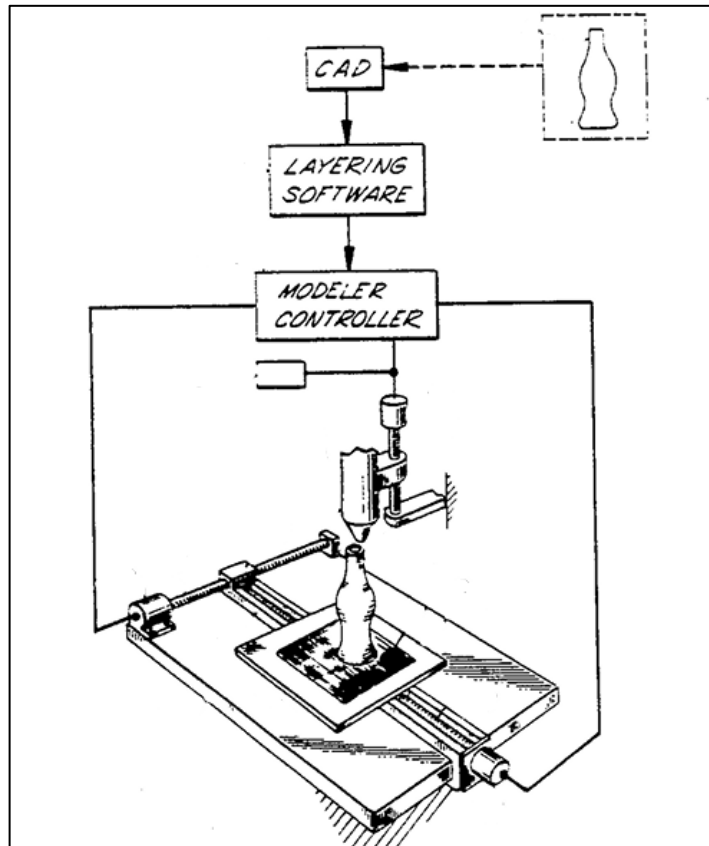


Figure 2.4. Original FDM apparatus drawing as presented by S. Scott Crump (Crump, 1992)

There are various stages involved in 3D printing rock samples, starting with digital design and ending with the printed final result. Digital modeling, material selection, printing itself, post-processing, testing, and analysis are among the crucial phases. Using software for design, researchers can develop precise digital models of the rock structures they want to analyze. The digital model can contain geomechanical parameters, like porosity, permeability, and fracture patterns. The choice of materials is important since the printing materials need to replicate the mechanical characteristics of real rocks. Common options include resin composites, polymers,

and gypsum. The digital model is first divided into thin layers, which the 3D printer will then produce one after the other. Softwares enable us to transfer obtained layered prototypes into STL formats that can be read by most of the commercial printers. Also, printing parameters such as printing temperature and speed, layer thickness and filling density can be selected in this software. Depending on the material and required qualities, a variety of printing techniques are used, that were mentioned above. FDM is an widely used technology for producing detailed and long-lasting models because it builds the model by layering heated material extrusion. However, printing of whole specimens or rock-like samples that accurately mimic the variety of characteristics seen in real rocks is still a challenge. Gao et al. (2021) in their broad review of 3D printing in rock mechanics, mentioned that while mechanical properties of 3D-printed rock, such as the stress-strain curve and failure mode, are similar to those of real rock; on the other hand, the majority of 3D-printed rock analogues typically have high ductility, low strength, and low stiffness. They also cover the limitations of current printing techniques such as limitations of printed materials and printing accuracy during the creation of complex internal structures of the natural rocks. Niu et al. (2023) also mentioned that printing materials shows properties such as strong ductility, low brittleness, and strength, and there is still a gap with the mechanical qualities of natural rocks. However, they also add that among 2 mostly used methodologies: printing of casting molds and printing of whole specimens, first one gives higher accuracies compared with traditional casting mold methods.

The recent developments in printing enable us to create complex rock-like structures with various fracture networks and to physically interact with physical scale models of rare geological formations by the creation of detailed replicas. However, while reviewing the literature, it can be observed that previous studies have almost exclusively focused on mimicking the material itself – printing the whole specimens or connecting printed layers. In that case, proper imitation of rocks is limited due to the differences between the real nature of the material and the artificial ones (Hodder et al., 2018). Also, some of the previous works have relied on the utilization of powder-based printers. Different printing settings were compared in the study by

Fereshtenejad and Song (2016), and they concluded that various printing layer thickness values had no mentionable effect on the strength of the specimens. Also, they noticed that there were a number of differences in the UCS between the specimens printed under comparable circumstances, such as printing angle (Figure 2.5), some of which were unsuitable for use in the field of rock mechanics.

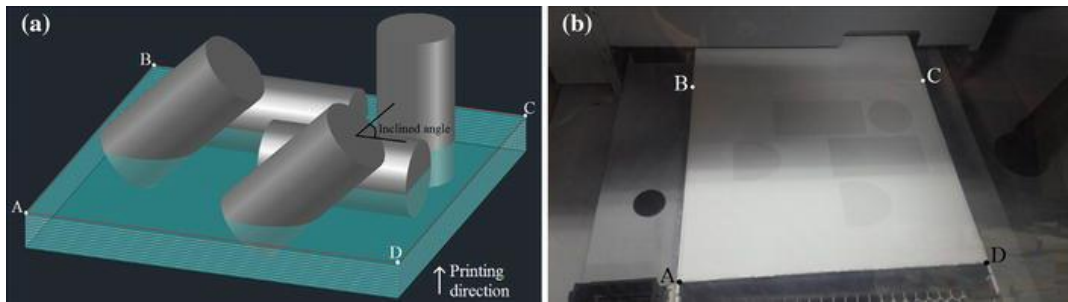


Figure 2.5. Different arrangements to print specimens with different inclined angles (Fereshtenejad and Song, 2016)

To improve the strength and stiffness of the 3DP gypsum powder samples and replicate the mechanical behavior of the severely stressed soft rock, the vacuum infiltration approach was suggested by Z.Vu et al. (2019) as a post-treatment method. It was found that post-treatments affect stress-strain behaviors and failure modes immensely. As a result of another research that focuses on pore analysis of 3DP gypsum samples shows that only very weak, fine-grained sandstone pairs well with 3DP gypsum-like material due to the restrictions of printing material and resolution (Kong et al., 2018). In addition, the authors proposed new classification categories for the relation between pore shapes and fractures, such as intrapore micro-fracture, interpore micro-fracture, and micro-fracture perforating pores.

Gell et al. (2019), in their broad review of the use of artificial specimens, discussed the advantages and disadvantages of both 3D printing and molding techniques. After inspecting numerous studies, they also came to the conclusion that the primary issue with synthetic materials is that they are not able to adequately simulate the mechanical properties of rock. The authors mention the importance of the correct

selection of printing materials and settings and propose some solutions, such as the availability of new printing materials and techniques.

When it comes to the effect of used material, PLA printed specimens showed brittle behavior in tension and a tendency to be plastic when compressed (Jiang and Zhao, 2014). Also, powder-based 3DP specimens showed highly ductile behavior and failed at very low compressive stress, making them unsuitable for simulating ordinary hard and brittle rocks (Zhou and Zhu, 2017). Jiang et al. (2015) brought up some limitations of the 3D Printing technique - for instance, the compressive strength of the rock-like specimens that are currently printed using sand powder material is only less than 10 MPa. They also add that the majority of printers on the market today can only print one or two materials since they only have one or two printing nozzles. In contrast, the mechanical characteristics of genuine rock masses vary widely.

Combined application of 3DP and numerical modeling techniques have also been previously reported in the literature. One of them is a physical simulation constructed from the 3DP sandstone model by Jiang et al. (2020), which was presented for evaluation of the safety of the multi-tunnel system. In order to study the mechanical and fracture properties of rocks under both static and dynamic loading conditions, a paper by Zhu et al. (2018) reports on the replication of internal defects of natural rocks using the SLA (stereolithography apparatus) 3DP method and numerical method in conjunction with X-ray micro-CT. It was confirmed that the resin-based 3DP rocks could be used to study the mechanical and fracture properties of brittle rocks, such as volcanic and porous rocks, by comparing their compressive strength, dynamic tensile strength, Poisson's ratio, and fracturing properties favorably with those of the prototype natural rocks. Using a combination of laboratory testing and numerical techniques, the effects of joint intensity (Figure 2.5) and joint connectivity on the strength of rock-like material with complicated discrete joints were examined by Tang et al.(2024). Numerical simulation results indicate that when the joint intensity of a rock-like material is low, the joint connectivity has a substantial impact

on the material's strength. However, as the joint intensity increases, the impact of the joint connectivity on strength decreases.

Several studies were focused on the utilization of new printing techniques, more precisely re-designed machinery that can print cementitious materials layer by layer using extrusion printhead (Gosselin et al., 2016; Kazemian et al., 2017). The recently developed method by Feng et al. (2019) showed that water segregation and rapid solidification were the two main drawbacks of using geological material for 3D printing. The issues mentioned above could be prevented by using a setting retarder and a water-retaining agent. However, these modifications can not be made to most of the 3D printers as their working principle usually is limited to heating and moving of the selected material.

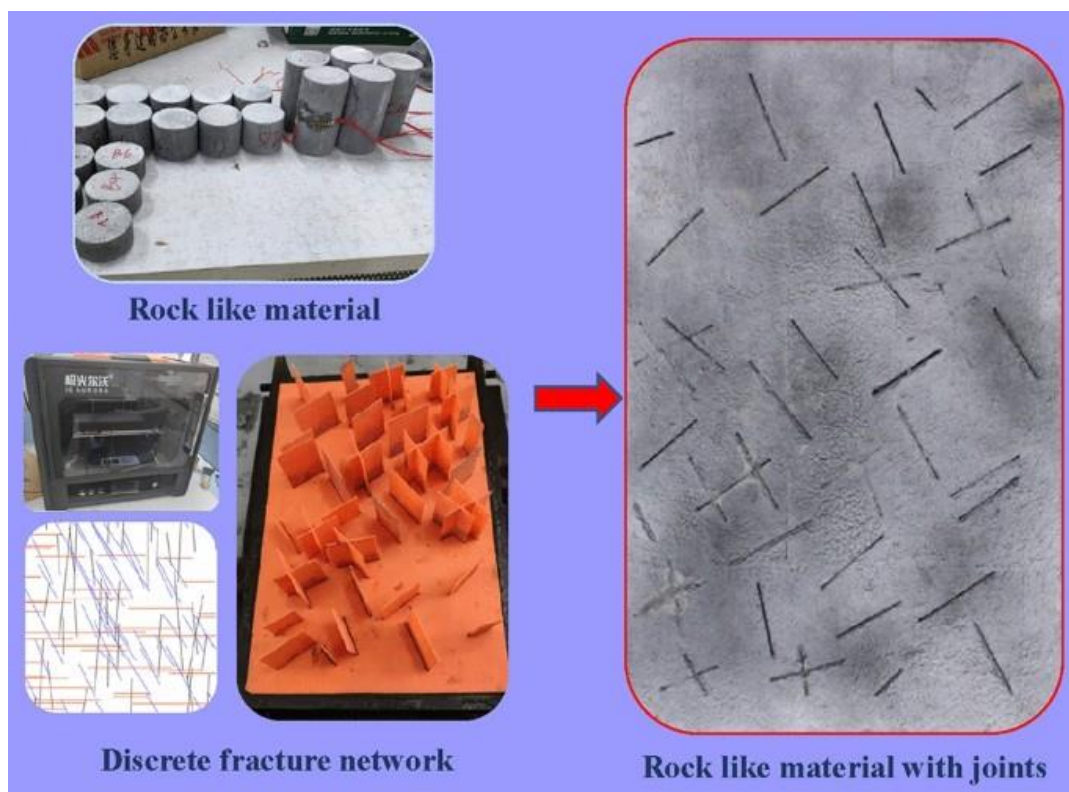


Figure 2.6. Process for preparing rock-like material sample (Tang et al., 2024)

After reviewing the literature, it can be seen that there are some potentially open questions about the validity of most used powder-based printing methods. Although there are many studies, previous research depend on rough models prepared by molding large blocks and creating the cleat-like discontinuities explicitly by hand made fractures. However, this study will be the first attempt to create cleat networks with 3D-printed planes, which will provide more realistic networks. The combined use of 3D printing for the creation of molds with different fracture networks and mixture pouring can be considered a strong alternative to the fracture creation process.

CHAPTER 3

EXPERIMENTAL DESIGN AND PROCEDURES

3.1 Sample Preparation and Laboratory Tests

This chapter covers coal cleat connectivity types and distributions and different techniques that were tested out for imitating the coal cleat structures during the study. For that purpose, the fractured nature of coal was approached like the connection of blocks with the weak bonding material along the discontinuities. The blocks were created using the molds that were originally printed in the 3D printer. The design of the molds was created in the CAD environment and later on transferred to the slicer software. Obtained files in STL format, were later sent to the Creality Cermoon D1 commercial printer. By using the extrusion method, which involves forcing molten plastic through a nozzle by heating it to the range of 200-220° – PLA+ type in our case, the printer starts printing by depositing the material layer by layer. Standard printing quality with a layer height of 0.2 mm was selected in our case, and the infill density of the prototypes was modified to be as minimum as possible (10-20%). In order to improve bed adhesion and facilitating easy removing of shapes, adhesive glue was applied to the printer bed. Also while separating shapes from the bed, some of the parts got stuck and their removal was achieved by simply heating the bed itself. Final products were polished in order to obtain smoother surfaces. Molds were filled with mixtures containing different ratios of cement, gypsum, coal ash and water. After the molds were removed, samples were prepared by connecting obtained blocks with different connectivity combinations. Some of the molds had created difficulties during the removal process, so we applied heat to their surfaces in order to soften the plastic material. Later on, the uniaxial compressive strength test and static deformability test were carried out and relationships were obtained. Obtained

experimental data trends were modified and used as input parameters during the modeling of continuum longwall mine simulations.

3.1.1 Blocked Structures

The first technique enables us to prepare samples with two different block geometries, which can also be reviewed as a representation of coal cleat dimensions of a rock-like material. Those two types of blocks have a height of 6 cm, but they differ from one another by their side lengths: 1 and 2 cm, respectively, as shown in Figure 3.1.d. Based on the sizes of blocks, we categorize samples as Fine Blocked and Coarse Blocked ones. Numerous pairs of two adjacent faces of rectangular prism-shaped molds were printed and, later on, glued to one another with the adhesive (Figure 3.1.a and Figure 3.1.b). A mixture containing a 1:2:3:4 ratio (HC mixture type) of coal ash, gypsum, cement, and water was mixed and poured into the molds.

The primary purpose here is to create two bigger blocks, as shown in Figure 3.3.a, containing attached coarse/fine pieces that connect with each other by a weaker bonding material and later obtain numerous samples from them. Figure 3.2.a illustrates one “layer” of combined blocks onto which the same type of several “layers” will be connected, and a final bigger rock sample will be obtained. For example, in the creation of such bigger cubical rock block with dimensions of 24 cm x 13 cm x 7 cm, approximately 350 fine pieces were used. The bonding material in all types of samples is a mixture of gypsum and water with respective ratios of 3:2. Other mixture ratios were also tested for this purpose, however they end up being too diluted or concentrated. In those cases, blocks were not able to attach to one another properly, or application of the bonding material were very challenging due to its saturation. It can be also added that, for further studies effect of bonding material and its other characteristics can be also studied and various connectivity options can be tested out.

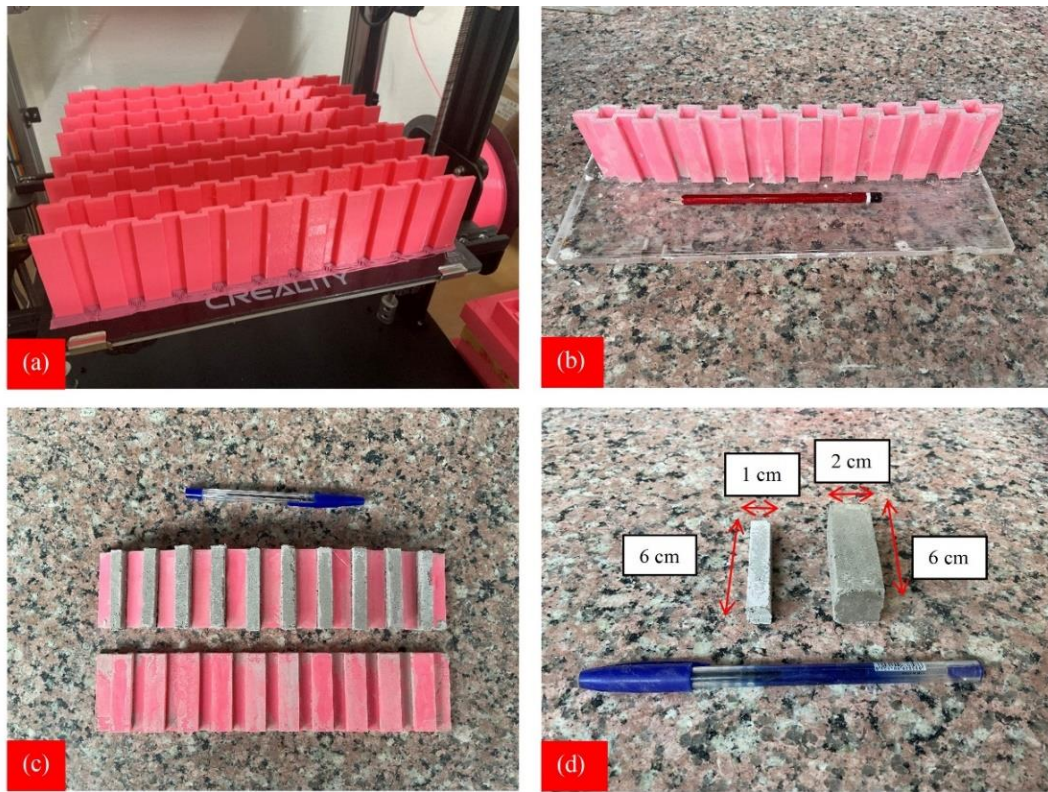


Figure 3.1. (a) Printing stage of mold sides (b) connected version of molds (c) detachment of blocks from molds (d) comparison of fine and coarse blocks

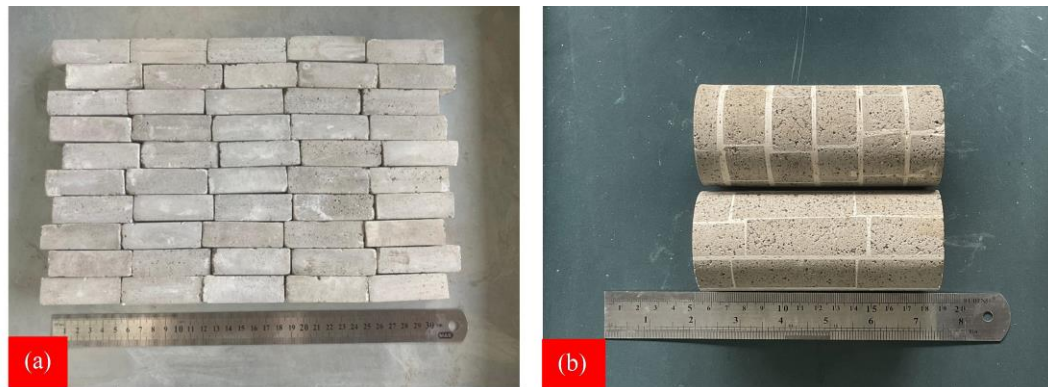


Figure 3.2. (a) connectivity combination of coarse blocks in one layer (b) Coarse_BLL and Coarse_BLS samples

Two types of samples were obtained from each of the blocks depending on the respective core drilling direction of 0° and 90° ; they were briefly named Block Long

(BLL) and Block Short (BLS). In general, four general types of blocked samples were categorized: Fine_BLL, Fine_BLS, Coarse_BLL, and Coarse_BLS (Figure 3.2.b, Figure 3.3.b, Figure 3.3.c).



Figure 3.3. (a) bigger block constructed from the attachment of “layers” (b) Fine_BLL samples (c) Fine_BLS samples

3.1.2 Complex Cubical Design

Another approach is the direct imitation of connection surfaces inside the coal by printing those patterns in the shape of molds via a 3D printer. Each mold has its own respective pair from which the opposite adjacent component with conforming patterns will be detached. In this case, building bigger blocks was not possible due to the fragile nature of the mixture and shape of the models. Because of the mentioned reasons, molds were designed in sizes that enable us to generate a cubic sample directly from connecting them. For that purpose, mold geometries in Figure 3.4.a with sizes of 8x8 cm that contain 16 rectangles of 2x2 cm were printed out. Overall design pattern was introduced to the CAD software, while the height of the

smaller rectangles was randomly generated from the range of 0-2 cm by the functions of the software. Rectangles represent the connection between the face and butt cleats. The sides of the prototypes were closed with plexi-glass, which was detached after the mixture settled. To make the detaching procedure effortless and obtain blocks without any cracks, molds were covered with the grease. A mixture of coal ash, gypsum, cement, and water with ratios of 1:2:3:4 (HC mixture) ratios was mixed in the mixer and poured into the molds (Figure 3.4.b).

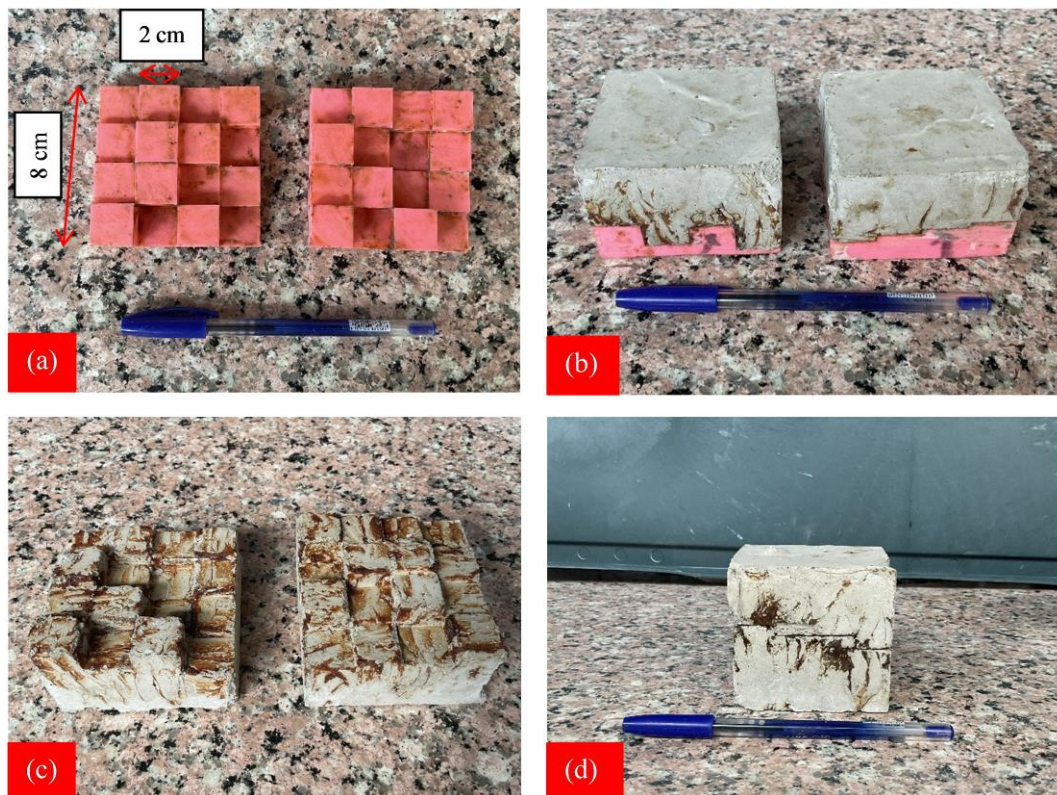


Figure 3.4. (a) mold geometries (b) settled mixtures (c) respective pair of blocks (d) connected blocks

Figure 3.4.c shows a block, and its own adjacent pair, which were later attached to one another with bonding material – a mixture of gypsum and water with ratios of 3:2. The approximate height of the connected blocks was between 3-3.5 cm (Figure 3.4.d), and four of those pieces or two pairs, were used in making of single cubical sample.

3.1.3 Angular Samples

In the creation of samples that contain various fracture orientations, the usage of the 3D printing method was not necessary. Layers with a height of 3 cm were created by simply pouring the mixture into ordinary plastic/wooden boxes. One aspect that differentiates these samples was the testing of two different mixtures that had different cement and gypsum concentrations.



Figure 3.5. (a) bigger sized cubical block from which cylindrical samples were obtained, sample with fracture orientation of (b) 0°, (c) 30°, (d) 60°, (e) 90°

For the first mixture, the ratio of coal ash, gypsum, cement, and water was 1:2:3:4 (HC mixture). For the second one, concentrations of gypsum and cement were

switched, and a ratio of 1:3:2:4 (LC mixture) was selected. After attaching 6-7 of those slices by the mixture with ratios of 3:2 gypsum and water, we were able to obtain a “cake-shaped” block from which samples were taken, which is shown in Figure 3.5.a. The basic approach here is to modify the angle of penetration for core drilling so that obtained samples have discontinuities with the orientations of 0°, 30°, 60° and 90° (Figure 3.5.b, Figure 3.5.c, Figure 3.5.d, Figure 3.5.e). Comparison of 2 different mixtures will enable us to observe how the concentration of cement and gypsum in the mixture impacts the strength and behavior of samples. It is worth mentioning that when cylindrical samples were obtained by the drilling process, the machinery's high vibration rate resulted in cracking at some parts of the samples. Because of this reason, the mentioned parts were reattached to the samples with the help of bonding material in as accurate a way as possible.

3.1.4 Continuous Samples

In this methodology, samples without any type of discontinuities were created in order to compare them with the fractured samples. For that purpose, adjacent sides of molds with cylindrical shapes were printed out and glued to one another (Figure 3.6.a). Their inner dimensions were 13 cm in height and 5.4 cm in diameter. During the preparation, two types of mixtures with higher (HC) and lower (LC) cement concentrations, which were mentioned before, were used for this stage as well.

Overall, we were able to prepare 2 to 4 samples for each type of design and approach (Table 3.1). In general, total of approximately 50 samples were utilized during the experiments. It is undeniable that some inaccuracies during the mixture pouring stage caused minor differences in the dimensions of the samples, which are supposed to be around 12 cm in length and 5.4 cm in diameter. Samples were cured at room temperature of 20-25°C for 28 days. We ensured that samples remained moist by spraying them with water or using wet covering sometimes due to the dihydrating nature of the gypsum. Static deformability and uniaxial compressive strength tests were carried out on samples, and lateral and axial deformations along the samples

were recorded by extensometers of the MTS. Additionally, values of UCS, E, ν , Bulk and Shear Modulus, as well as Stress-Strain graphs, were calculated for each group of samples. More accurate values of axial and lateral strain were recorded by the Testbox 1001 data acquisition system and by the application of 120 Ohm Strain Gauges in quarter bridge configuration, as shown in Figure 3.8.a. While recording axial strain in most of the samples, strain gauges were attached exactly to the center of the sample and parallel to the loading direction, while for some of the cases – for the ones with fracture orientation of 0° and Coarse_BLS (Figure 3.8.b) samples more specifically, it was unable to do so.



Figure 3.6. (a) cylindrical molds, (b) continuous samples

As there were fractures passing through the center of the sample, the strain gauge was glued to the center of the smaller piece, which was located above the center of the sample. Also, for some of the Continuous and Coarse_BLL/Coarse_BLS sample types, lateral strain data was also acquired by attaching strain gauges perpendicular to the loading directions. It must be noted that, for some types of samples, it was not

possible to attach strain gauges at all. Those samples were Cubic ones and their whole surface was covered in gypsum. Strain gauges could not be attached properly due to the easily disintegrable nature of the gypsum. Other ones were Fine_BLL/Fine_BLS samples, in which fracture positions on the surface were so dense that strain gauges were not attached as they would not be able to measure the accurate data from the material itself. Illustrations of the obtained samples and their preparation details are given on the Figure 3.7 and Table 3.1.

Table 3.1 Characteristics of different sample types











Sample Types	Mixture Ratios	Design Types	Sample picture	Bonding material
LC_C	Cement:Gypsum:Coal Ash:Water(2:3:1:4)	Continuous		Gypsum:Water (3:2)
LC_0	Cement:Gypsum:Coal Ash:Water(2:3:1:4)	Angled		Gypsum:Water (3:2)
LC_30	Cement:Gypsum:Coal Ash:Water(2:3:1:4)	Angled		Gypsum:Water (3:2)
LC_60	Cement:Gypsum:Coal Ash:Water(2:3:1:4)	Angled		Gypsum:Water (3:2)
LC_90	Cement:Gypsum:Coal Ash:Water(2:3:1:4)	Angled		Gypsum:Water (3:2)
HC_C	Cement:Gypsum:Coal Ash:Water(3:2:1:4)	Continuous		Gypsum:Water (3:2)
HC_0	Cement:Gypsum:Coal Ash:Water(3:2:1:4)	Angled		Gypsum:Water (3:2)
HC_30	Cement:Gypsum:Coal Ash:Water(3:2:1:4)	Angled		Gypsum:Water (3:2)
HC_60	Cement:Gypsum:Coal Ash:Water(3:2:1:4)	Angled		Gypsum:Water (3:2)
HC_90	Cement:Gypsum:Coal Ash:Water(3:2:1:4)	Angled		Gypsum:Water (3:2)
Coarse_BLL(HC)	Cement:Gypsum:Coal Ash:Water(3:2:1:4)	Coarse Blocked		Gypsum:Water (3:2)
Coarse_BLS(HC)	Cement:Gypsum:Coal Ash:Water(3:2:1:4)	Coarse Blocked		Gypsum:Water (3:2)
Fine_BLL(HC)	Cement:Gypsum:Coal Ash:Water(3:2:1:4)	Fine Blocked		Gypsum:Water (3:2)
Fine_BLS(HC)	Cement:Gypsum:Coal Ash:Water(3:2:1:4)	Fine Blocked		Gypsum:Water (3:2)
Cubic Design(HC)	Cement:Gypsum:Coal Ash:Water(3:2:1:4)	Complex Cubical Design		Gypsum:Water (3:2)



Figure 3.7. (a) samples LC_90, LC_0, Coarse_BLL, Coarse_BLS (from left to right)
 (b) samples HC_0, HC_90, HC_60, HC_30 (from left to right) (c) samples HC_C,
 LC_C, LC_30, LC_60 (from left to right) (d) samples Cubic, Fine_BLL, Fine_BLS
 (from left to right)

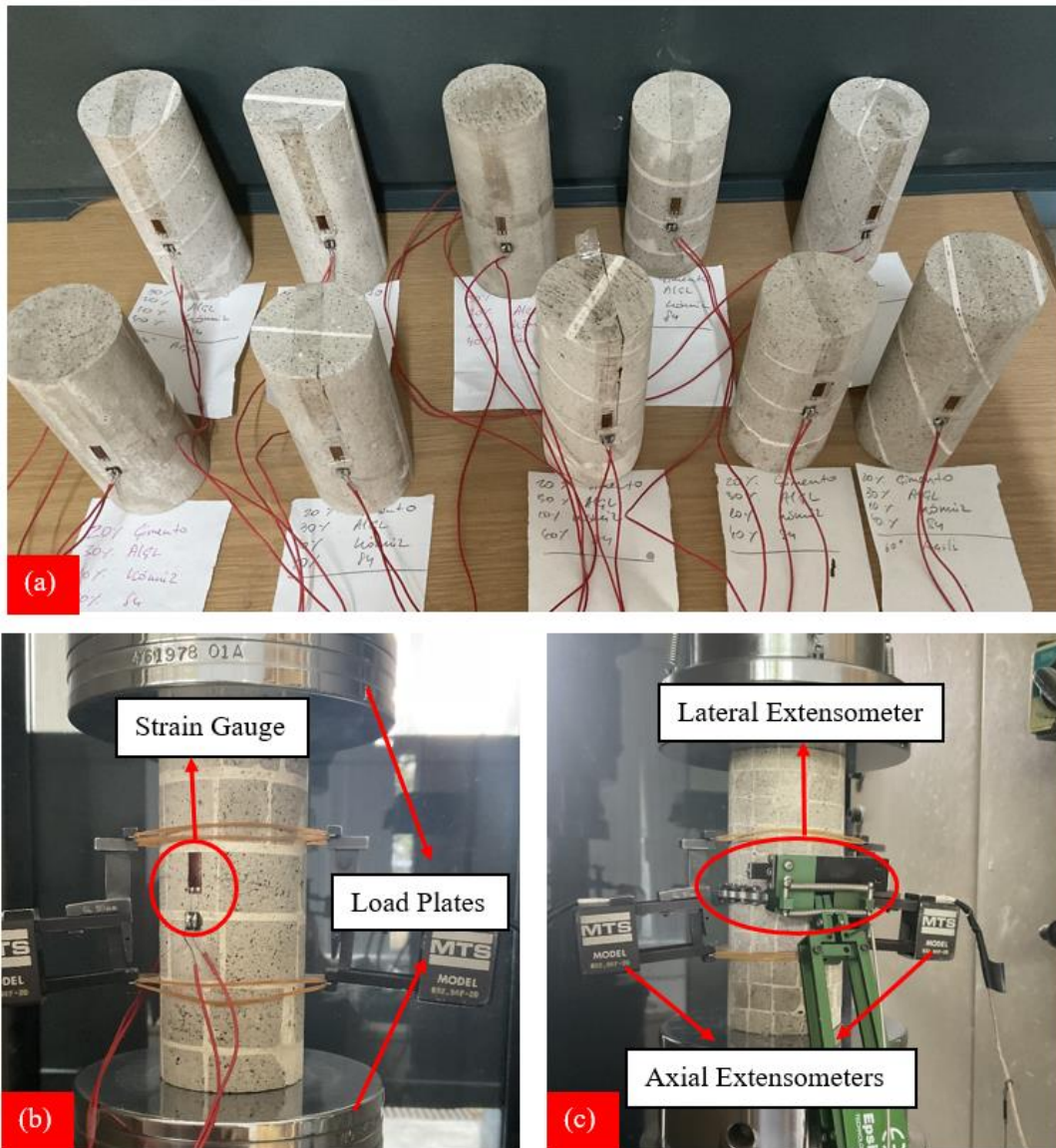


Figure 3.8. (a) samples to which strain gauges were attached (b) sample Coarse_BLL with strain gauge attached to it (c) sample Fine_BLS with attached extensometers

3.2 Analysis of Experimental Outcomes

Results of static deformability and uniaxial compressive strength tests were obtained, and recorded lateral/axial deformation, axial force, and dimensional data of samples were used during the calculations of E , ν , UCS, and Axial/Lateral Strain at Failure.

In order to examine the data, respective values from the Table 3.2 were plotted on a scatter graph. The primary goal is to compare the mixtures, design types, orientations, and other factors.

Table 3.2 Average values of obtained parameters for different sample types (data from extansometers)

Sample types	Avg. UCS (MPa)	Avg. Elastic Modulus, E (GPa)	Avg.Poissons ratio, ν	Avg. Axial Strain(%) at Failure	Avg.Lateral Strain(%) at Failure
LC_C	1.7	1.23	0.13	0.15	0.03
LC_0	2.8	1.39	0.1	0.32	0.05
LC_30	2.7	1.33	0.12	0.34	0.11
LC_60	2	1.81	0.11	0.18	0.05
LC_90	2.8	1.82	0.12	0.23	0.11
HC_C	1.2	0.97	0.14	0.14	0.03
HC_0	5.9	3.1	0.08	0.31	0.06
HC_30	4.9	2.31	0.12	0.43	0.07
HC_60	2.5	2.9	0.11	0.09	0.01
HC_90	5.9	4.54	0.21	0.15	0.22
Coarse_BLL(HC)	4.2	2.53	0.11	0.32	0.43
Coarse_BLS(HC)	3.9	1.76	0.07	0.3	0.19
Fine_BLL(HC)	3.4	2.7	0.11	0.12	0.02
Fine_BLS(HC)	2.5	1.9	0.34	0.18	0.19
Cubic Design(HC)	0.9	-	-	-	-

Correlation functions were fitted to represent the relationship between the fracture orientations and mentioned parameters, from which trendlines were obtained afterwards. Continuous and blocked samples were not taken into consideration for this analysis to maintain a reasonable correlation. In Figure 3.9, it can be observed that for angled samples that contained a higher concentration of cement, most of the parameters showed higher values than the ones with lower cement concentration. For example, HC samples that had a fracture of 90° showed 2.5 times higher results of average E when compared with LC samples of the same fracture orientation. While for the HC samples, the data trend of the Modulus of Elasticity was fitted into a degree polynomial function, for LC samples, it was a linear function.

The sharp decrease from 3.1 GPa to 2.3 GPa can be observed around 30° for HC samples, which continues with the increase at the following degrees. In general, both types of BLS samples had lower values when compared with their respective BLL

pairs. For blocked samples, both Coarse_BLL_Avg_E/Coarse_BLS_Avg_E and Fine_BLL_Avg_E/Fine_BLS_Avg_E ratios were equal to 1.45.

For the trends representing Poisson’s ratio, it was the vice-versa: linear function for the HC samples and second-degree polynomial for LC samples (Figure 3.10). The most noticeable difference belonged to the samples having fracture orientation of 90°, as it was also the case among the E values. HC samples showed 1.75 times higher results of average ν value than the LC ones.

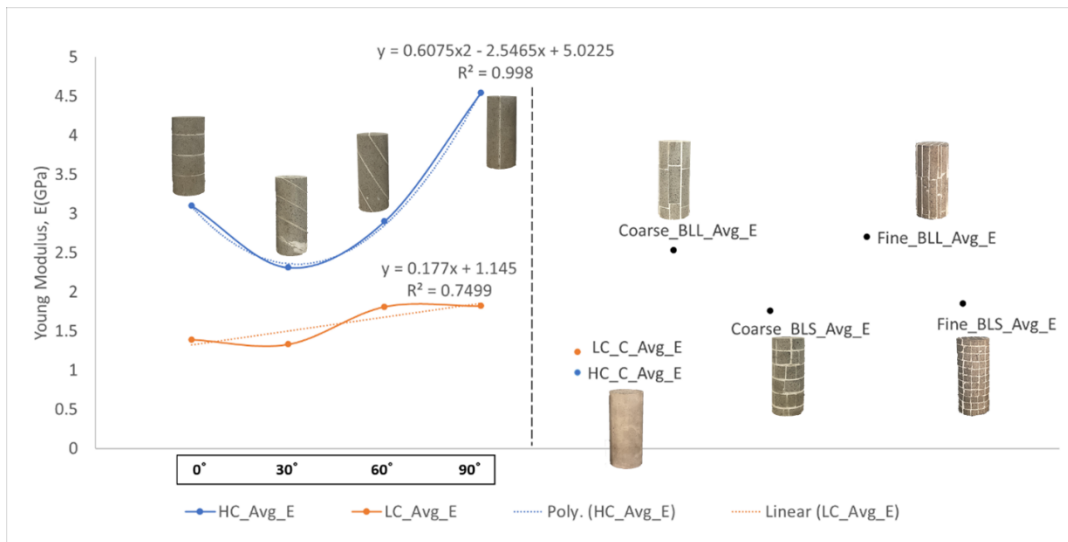


Figure 3.9. Average Young Modulus (GPa) of experimental samples (from extensometer)

When comparing average Poisson’s ratios of blocked samples, BLL ones for both fine and coarse ones was equal to 0.11. On the contrary, Fine_BLS samples showed higher average value than Coarse_BLS ones. From the mentioned result, it can be interpreted that for BLS-type blocked models, fracture density affects Poisson’s ratio.

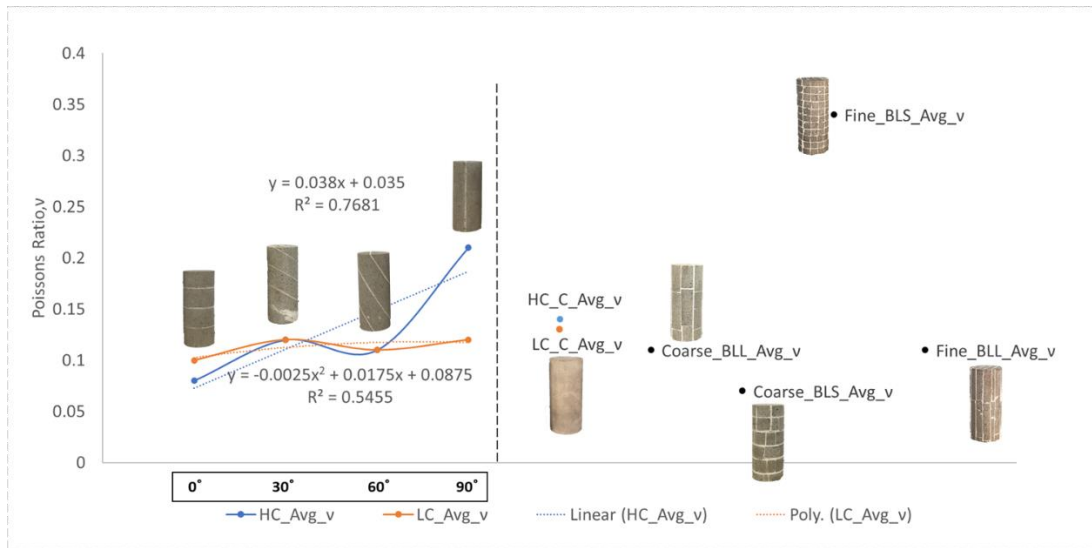


Figure 3.10. Average Poisson's ratio of experimental samples (from extensometer)

Trend lines representing average UCS data for both LC and HC samples were fit into second-degree polynomial functions (Figure 3.11). A sharp decrease can be seen at around 60° , which can be explained by the failure type of the samples with respective degrees. The samples with fracture orientation of 60° got fragmented along the discontinuity surface, which can be considered as weaker zones during the compression test. Another notable point is that UCS values for 0° and 90° were the same for both LC and HC examples. It means that the rock samples with fractures positioned parallel and perpendicular to the compression direction show similar strength behavior by having UCS values of 5.9 MPa for HC samples and 2.8 MPa for LC samples.

Average UCS results also demonstrate that, in general, fine blocked samples got deformed at lower compression rates rather than the coarse blocked ones. For the BLL samples, coarse blocked versions had an average UCS value of 4.2 MPa, which was 23% higher than the ones of finer samples. When it comes to the BLS samples, the mentioned difference percentage was equal to 56%.

Exceptional relationship between the continuous samples of HC and LC mixtures can be seen, as their different parameters are either having very close values to one another or values of LC samples are bigger than the ones of HC unlike the other cases. From that relation, we can say that when there is no occurrence of fractures along the rock sample, the decrease in the concentration of cement results in the increase of sample's strength. When it comes to the comparison of Coarse_BLL and Coarse_BLS samples, in general, average values of all studied parameters show bigger results in BLL ones with respect to BLS ones.

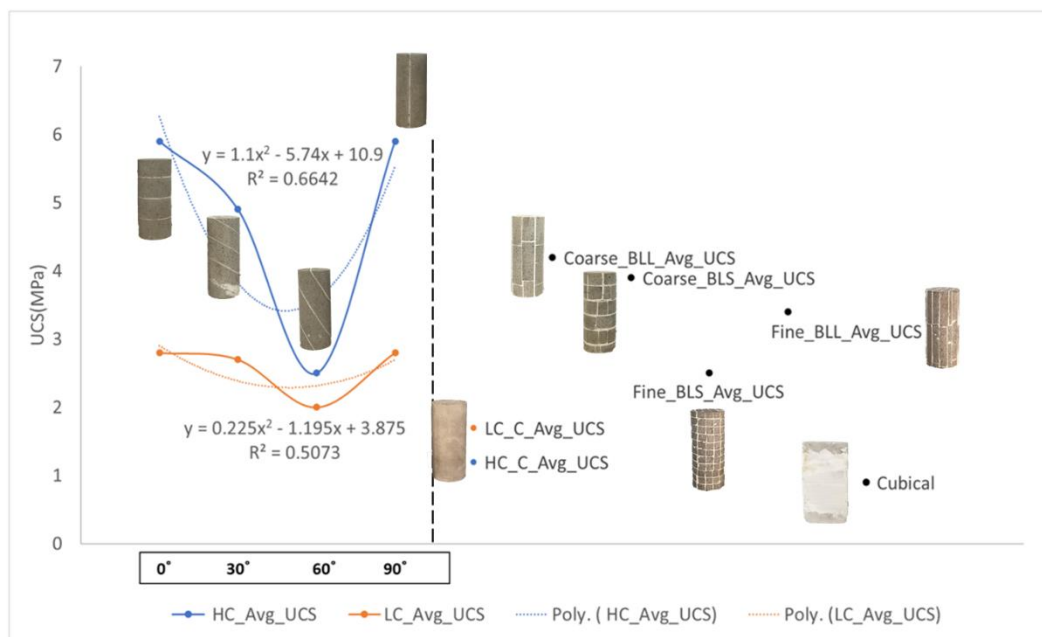


Figure 3.11. Average Uniaxial Compressive Strength (MPa) of experimental samples (from extensometer)

Results of average axial and lateral strain percentages from 100% at the moment of failure were represented in the following graphs (Figure 3.12, Figure 3.13). It is worth noting that, data trends show the average values, which were calculated from the outputs recorded by axial and lateral extensometers. While the axial strain trendline representing the dependency from an angle for HC samples was a second-degree polynomial function, for LC samples, it was a linear function. For the lateral

strain functions, there was a second-degree polynomial relationship for HC samples and a third-degree polynomial relationship for LC samples, respectively. It is also clearly shown that strain data of the continuous samples at the moment of failure were similar for both of the mixture types: 0.15% for the axial strain and 0.03% for the lateral strain. While axial strain outputs of Coarse_BLL and Coarse_BLS were pretty close to one another by having values of 0.3%, lateral strain values of Coarse_BLL ones show two times bigger results of 0.4% in comparison with the Coarse_BLS samples that have the result of 0.2%.

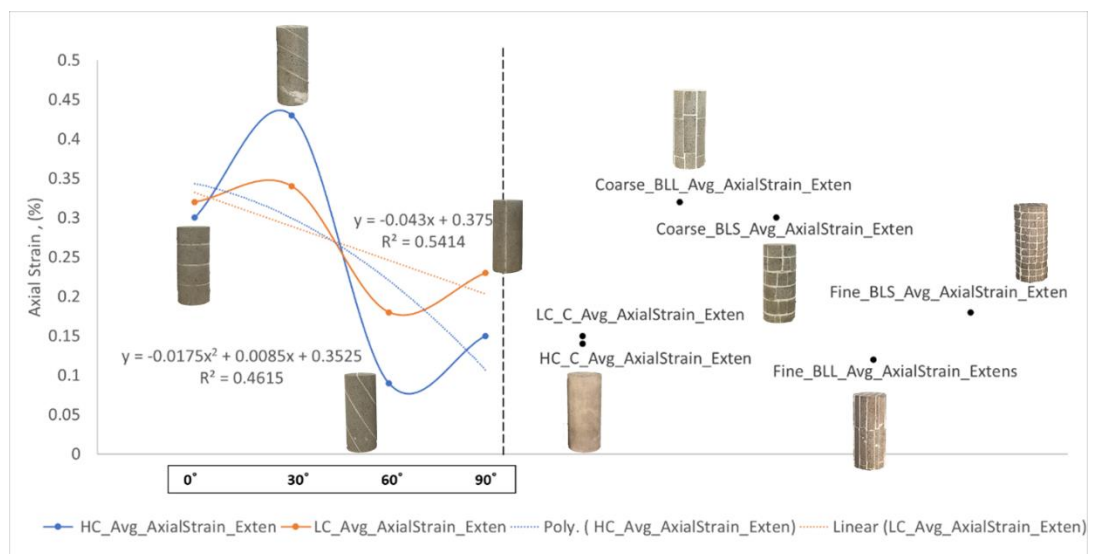


Figure 3.12. Average axial strain (%) at failure for different mixtures (from extensometers)

Next section includes the comparison of axial strains at the moment of failure acquired from both extensometers and Strain gauges (samples with strain gauges coded as SG_1). For more clear demonstration, samples with different cement ratios are given in separate graphs (Figure 3.14 and Figure 3.15). It is worth mentioning that, due to the errors and inaccuracies during the preparation of the samples with strain gauges, experiments did not take place for HC samples with fracture orientations of 30° and 60° (Table 3.3).

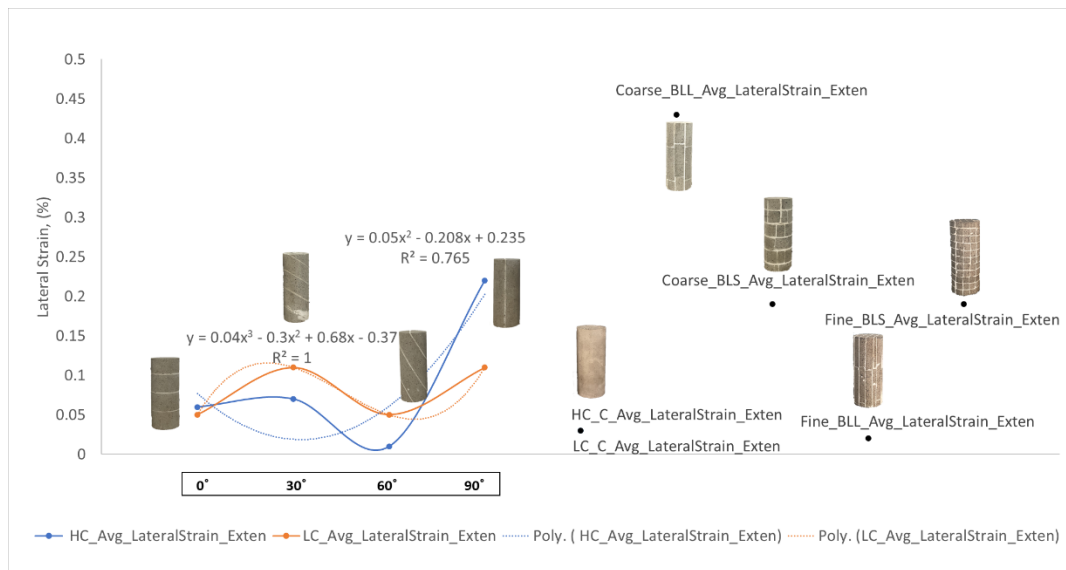


Figure 3.13. Average lateral strain (%) at failure for different mixtures (from extensometer)

Also, samples to which strain gauges were not attached were not mentioned in the graph. Observations show that for most of the samples, data acquired from both systems had very close values, which clarifies the accuracy of experiments. Results that demonstrate notably different values can be seen in the respective values of samples with an orientation of 0° (Figure 3.14, Figure 3.15). This difference provides an explanation for the strain variations based on their recording locations as the particular sample, the position of extensometers and strain gauges differed. While extensometer data were acquired exactly from the midpoint of the sample, strain gauges were attached to the center of the upper half of the sample. Interpretations prove that axial strain concentrates around the center of the sample 1.5-2 times more with respect to the points located far away from the midpoint. Despite this relationship, there were also samples in which data acquisition points were the same for both of the systems, but outputs slightly differed from one another.

Table 3.3 Axial/Lateral strain values(%) at failure moment (Extensometer versus Strain Gauge)

Samples with strain g.	AxialStrain_Extensometer(%)	Axiale StrainGauge(%)
HC_0_SG_N1	0.27	0.16
HC_30_SG_N1	0.55	-
HC_60_SG_N1	0.09	-
HC_90_SG_N1	0.17	0.17
Coarse_BLL_SG_N1	0.18	0.19
Coarse_BLS_SG_N1	0.16	0.22
HC_C_SG_N1	0.1	0.08
LC_0_SG_N1	0.31	0.2
LC_30_SG_N1	0.21	0.19
LC_60_SG_N1	0.06	0.07
LC_90_SG_N1	0.16	0.04
LC_C_SG_N1	0.15	0.12

Those inaccuracies can be explained by mentioning difficulties in the sample preparation stage or flaws that can result in errors during experiments. Table 3.4. demonstrates lateral strain values that were recorded by the utilization of strain gauges at the moment of failure. It was not possible to compare the mentioned results with the ones from extensometers because the position of strain gauges limited the space for the attachment of extensometers.

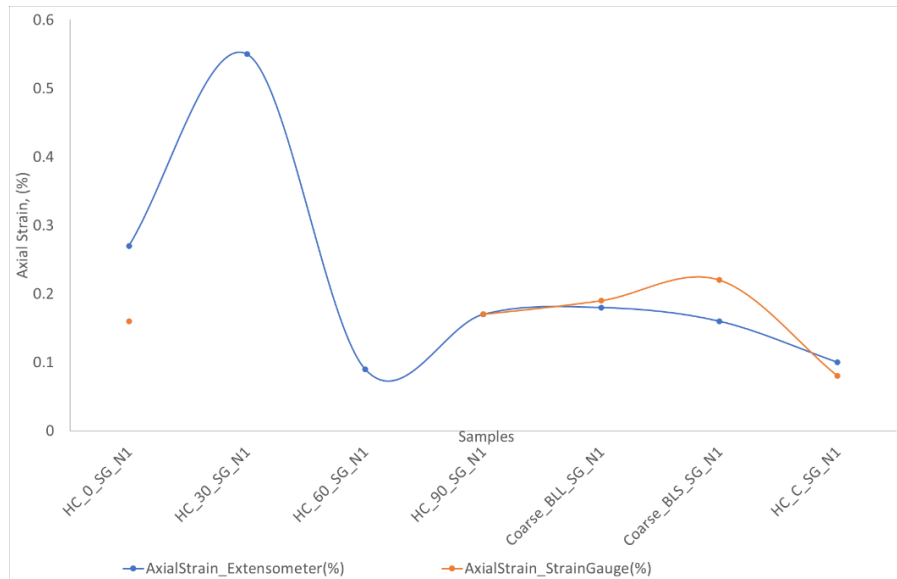


Figure 3.14. Axial strain values (%) of HC samples at failure (Extensometer versus Strain Gauge)

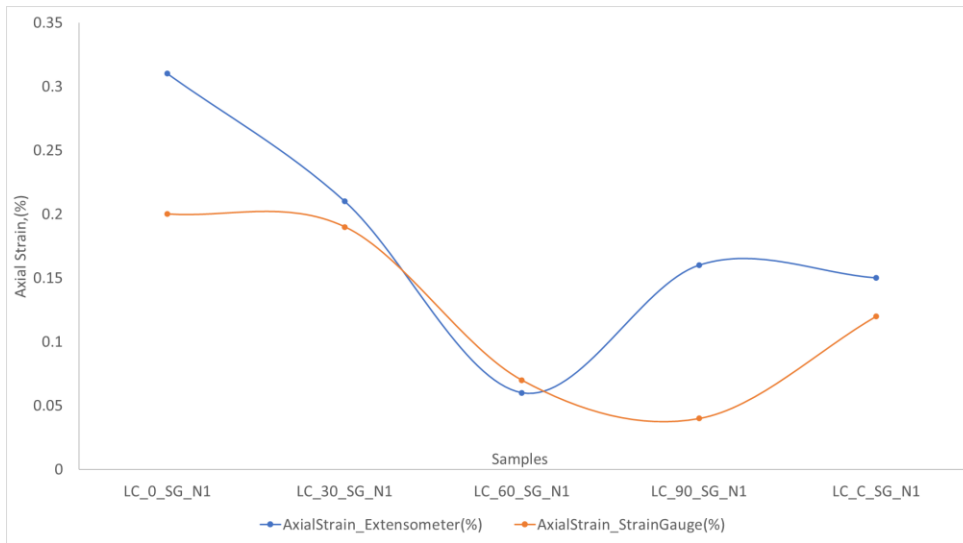


Figure 3.15. Axial strain (%) of LC samples at failure (Extensometer versus Strain Gauge)

Table 3.4 Lateral strain (%) at failure moment (Extensometer)

Samples with strain g.	LateralStrain_StrainGauge(%)
HC_C_SG_N1	0.03
LC_C_SG_N1	0.04
Coarse_BLL_SG_N1	0.03
Coarse_BLL_SG_N1	0.16

CHAPTER 4

Numerical Analysis

In this chapter, we will briefly discuss input parameters, geometries, and other information essential for constructing numerical models. Two groups of numerical models, continuum and discontinuum ones, will be constructed, and we will mention details about the generation of 16 different longwall mine models simulated in the ITASCA 3DEC software. Models differ from each other by several factors. While the first 8 of them were modeled in discontinuum media, where longwall panel consists of cleat networks with different orientation of 0° , 30° , 60° and 90° , the other 8 models are continuum models. In that case, parameters that were acquired from the testing of corresponding samples with the same cleat orientations in the previous chapter were modified and used as input data during the modeling of continuum models. In other words, obtained data trends from experimental part were utilized during the selection of input parameters for continuum models. For each case, two different simulations were modeled that differ from one another by stress conditions, which will be later described in more detail. The main objective here is to review how accurate numerical modeling illustrates the real-life behavior of rock masses with fractures and discontinuities. Especially stress patterns and stability issues along critical zones, such as the face and roof in longwall mines, are the main topics of interest. Also, we will be able to compare two different numerical modelling techniques and observe how accurately continuum media can represent fractured rock-like material. For that reason, the effect of cleat orientations inside the coal seam will be studied for various examination points along the different layers of the elastic models as excavation goes on.

Figure 4.1 lists the characteristics of all models that differ from one another by their numerical analysis approach, stress conditions, and present/imitated coal cleat angle.

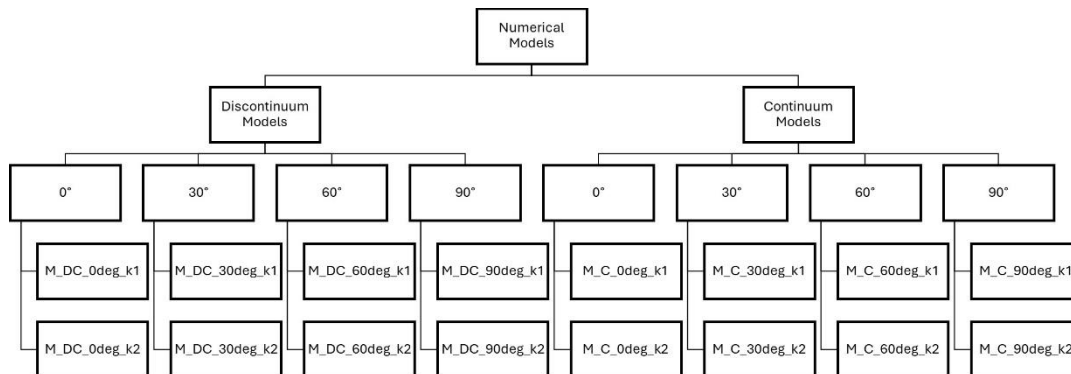


Figure 4.1. List of constructed 16 numerical simulations

4.1 Model Geometries and Construction

Models represent the typical Longwall Mine and surrounding layers with the help of rectangular prisms. It is worth noting that the dimensions of the corresponding layers, Floor, Coal Seam, Roof, and Overburden, stayed the same for all of the models. Origin is located in the bottom-left corner of the body, and the dimensions are 240 m in the x-direction and 200 m in the y-direction, respectively. The overall thicknesses of the models equal 254 m, as shown in Figure 4.2. For the discontinuum models, roofs were divided into randomly generated blocks with the help of DFN templates. As mentioned before, fracture sets with orientations of 0°, 30°, 60° and 90° degrees were defined for the coal seams of discontinuum simulations (Figure 4.3) as well, while for continuum models no discontinuities were defined. For all of the models, the excavation area was defined with respective dimensions of 120 m in the x direction and 140 m in the y direction. The mentioned excavation zone in Figure 4.4 was divided into 14 called “Coal Slices” that represented excavation stages with the advancement of 10 m. The mesh size of 10 m was set for Floor and Overburden, with a more dense value of 5 m for the Coal seam and Roof.

After the input parameters were modified and entered (discussed in part 4.2), velocity boundary conditions were set for all faces of the models except the upper side, which represents the topographical surface. Each model has its own modified version, which differs from the original one with the stress condition; the first one has a hydrostatic in-situ loading with 4 MPa ($k=1$), and in the second one, horizontal stress values were doubled to 8 MPa, for $k=2$. Gravitational forces were applied for all of the elastic models.

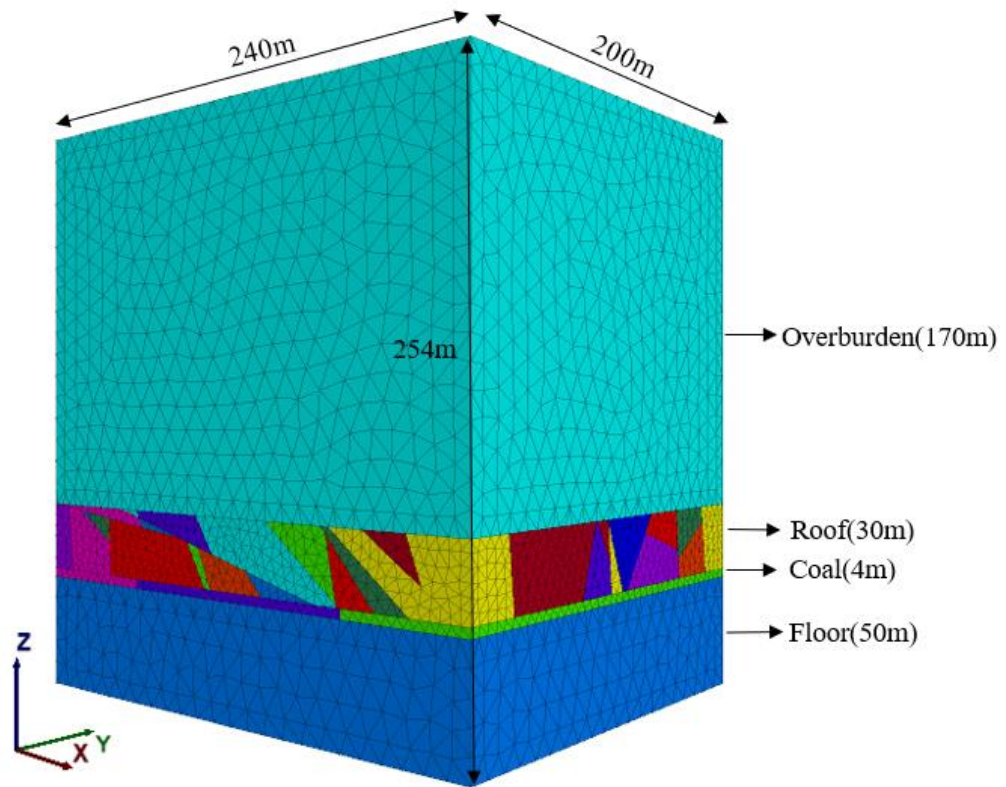


Figure 4.2. Strata and model geometry of the Longwall Mine Simulation

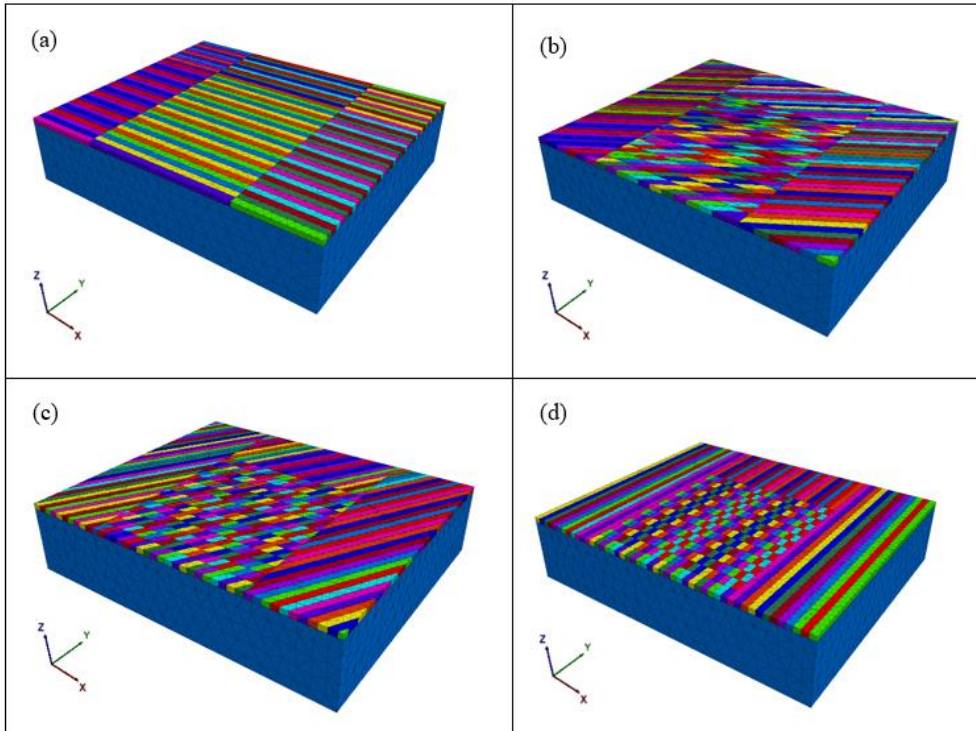


Figure 4.3. Coal seams in discontinuum models with respective fracture orientation of (a) 0° (b) 30° (c) 60° (d) 90°

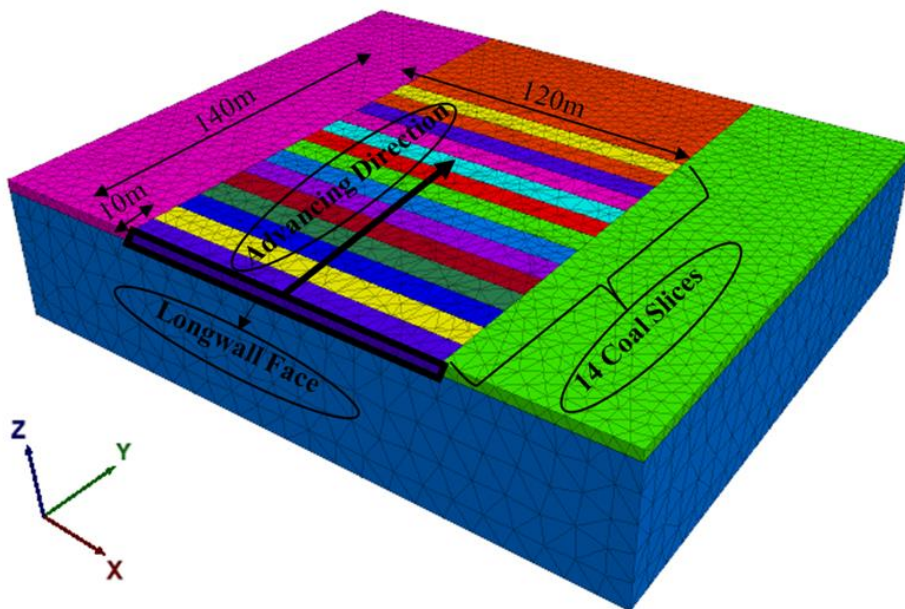


Figure 4.4. Dimensions of excavation zone divided into advancements of 10 m

4.2 Modification of Input Parameters

Elastic material properties for the layers and joint properties for discontinuum models were acquired from the literature and were adjusted for our model characteristics (Table 4.1 and Table 4.2). To obtain the input parameters for the continuous models, some modifications were made to the functions of the Modulus of Elasticity and Poisson's ratio of the HC samples.

Firstly, scatter graphs were lowered to the range of Coarse_BLL and Coarse_BLS values, as we assumed that discontinuum models represent the closest behavior to the coarsely blocked samples, and they could be taken as reference points (Figure 4.5).

Table 4.1 Elastic material properties assigned to the respective layers in discontinuum models

Layers	Modulus of Elasticity, E (GPa)	Poisson's Ratio, ν	Bulk Modulus, K (GPa)	Shear Modulus, G (GPa)	Density, kg/m^3
Floor	3.50	0.25	2.33	1.40	2800
Roof	2.50	0.25	1.67	1.00	1750
Overburden	2.00	0.25	1.33	0.80	2400
Coal	1.50	0.25	1.00	0.60	1400

Table 4.2 Joint properties of discontinuities

Joint Properties	Normal Stiffness (GN/m)	Shear Stiffness (GN/m)	Cohesion (kPa)	Angle of friction ($^\circ$)
Discontinuities and DFN	5	3	300	30

Later on, trendlines were generated for edited versions, and new results were calculated. The best-fitted options, such as linear and polynomial functions, were selected. Also, normalization factors that were derived from the relationship between parameters of Coarse_BLS samples and the ones of the Coal seam in the discontinuum model were applied to the outcomes. Material properties of all other layers stayed the same as the ones of discontinuum models. Mechanical parameters depending on fracture orientation were calculated from experimental trends. The

main concept here is to observe how rock-like fractured material will behave while being modeled by the continuum approach. It will be done by assigning input parameters from obtained experimental data trends to the continuum longwall mine models (Table 4.3). As was mentioned, experimental data trends represent the correlation between the geomechanical properties of the rock-like material and fracture orientations. Outcomes will be later compared with the directly simulated

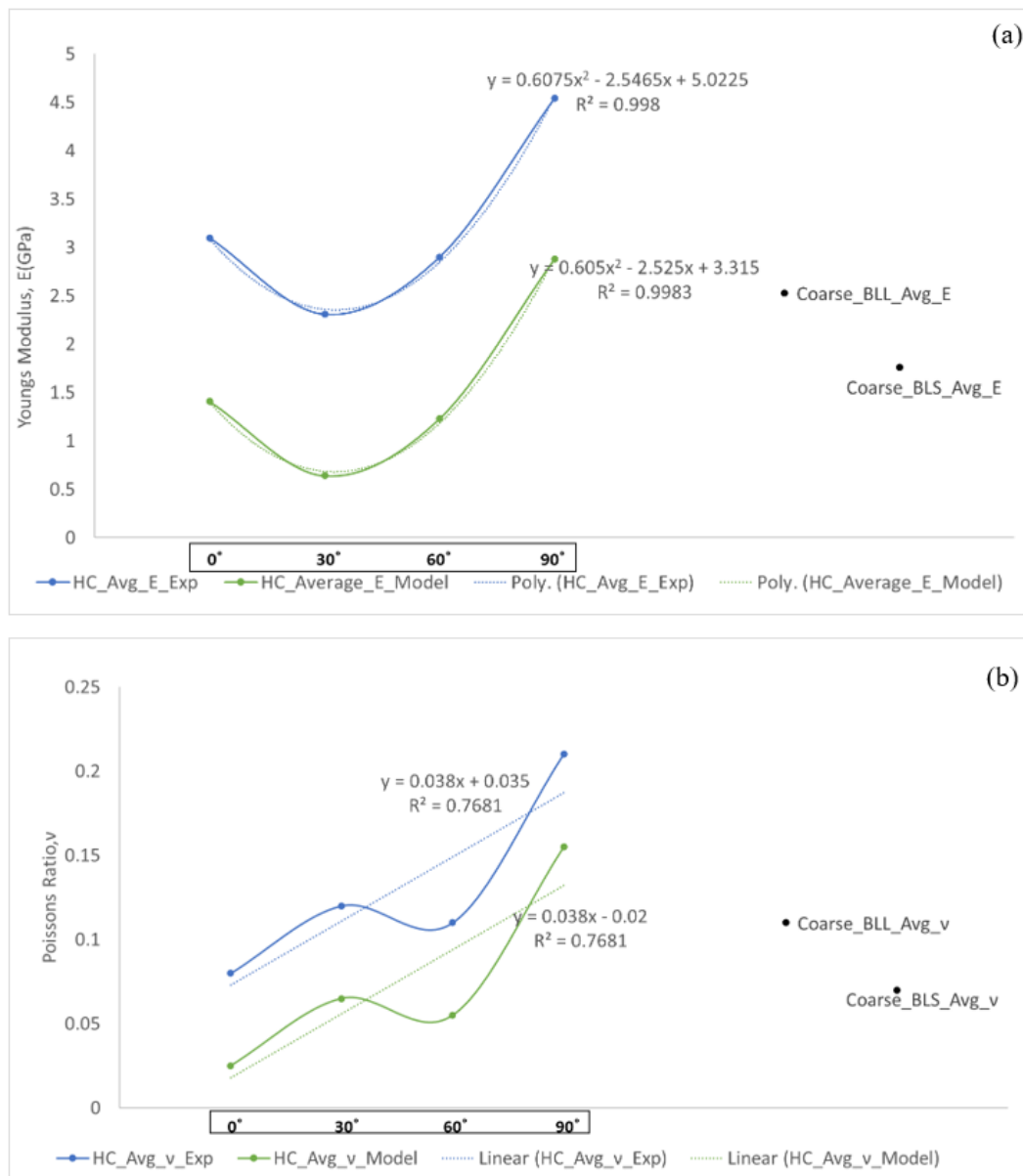


Figure 4.5. Modification of (a) E values (b) v values for continuum models

discontinuum models, and differences will be found. It will enable us to observe the accuracy of the continuum simulations in terms of representing the fractured material.

Table 4.3 Modified material properties of coal layer in continuum models

Imitated Fracture Orientation	Modulus of Elasticity, E (GPa)	Poisson's Ratio, ν	Bulk Modulus, K (GPa)	Shear Modulus, G(GPa)	Density, kg/m^3
Coal(0°)	1.19	0.10	0.49	0.54	1400
Coal(30°)	0.58	0.20	0.32	0.24	1400
Coal(60°)	1.01	0.34	1.02	0.38	1400
Coal(90°)	2.46	0.47	14.26	0.84	1400

4.3 Location of History Points and Execution of Simulations

In order to observe stress changes in the different points of respective layers as excavation stages were conducted, history points were positioned inside different locations. All the history points can be observed in Figure 4.6. Major principal stress values were recorded from the history points located in the center of each respective “Coal Slice” with 10 m space-between. Right above those particular points, history locations that were set to 3 meters high on the immediate roof of respective coal slices traced minor principle stress values. Other points that recorded minor principle stress values were centered on the midpoint of the roof. Additionally, the other two sets of history points were placed inside the overburden, more specifically, the ones located 30 meters high on the overburden and the others located 60 meters high on the overburden. The closest grid element was used by the software to allocate the history points. As each slice was excavated, 5000 iterative simulation solution steps passed in order to achieve the state of balance before the next excavation stage. After each time step goes by, values of the mentioned parameters from 70 history points were stored for in-detail analysis. It took a total of approximately 80000 steps for all of the 14 excavation stages to finish.

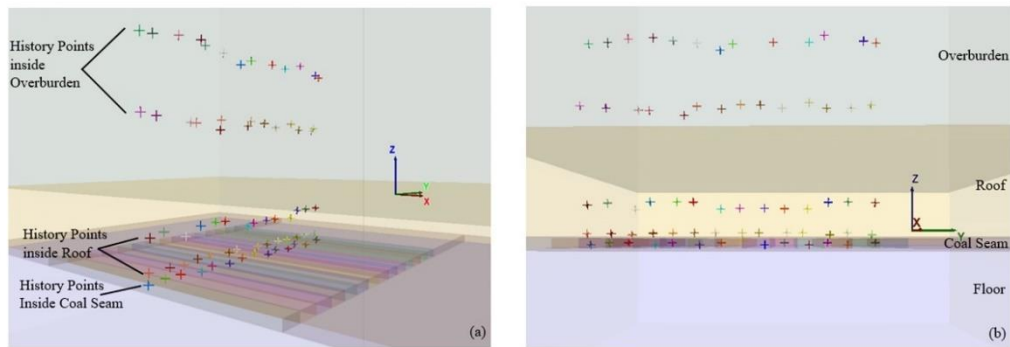


Figure 4.6. History locations from (a) perspective view and (b) side view

Values obtained from the history points related to two of the coal slices; the 5th and 10th coal slices will be the main focus of the results and discussion chapter. To understand the sequence of history points around them, the cross-sectional planar view that crosses from the midpoint of the nth slice is given in Figure 4.7.

Mentioned history point that positioned in the center of the coal seam is labeled as “nth_A”, while the ones in the immediate roof and center of the roof are labeled as “nth_B” and “nth_C” respectively. The remaining history points, located 30 m and 60 m above the overburden, are named “nth_D” and “nth_E”. There are no additional points above the selected locations because the effect of excavation stages could not be observed properly as we get far away from the deformation zones. A detailed analysis will be done by plotting principal stress data to the graphs obtained from the historical points that were brought up. Data from points that were located on the cross-sectional plane of the 5th and 10th coal slices, or in other words, above the 5th and 10th coal slices, will be examined. How excavation stages influenced the stress behavior in the face, immediate roof, and overburden in the different models with various fracture types and modeling approaches will be found at the end.

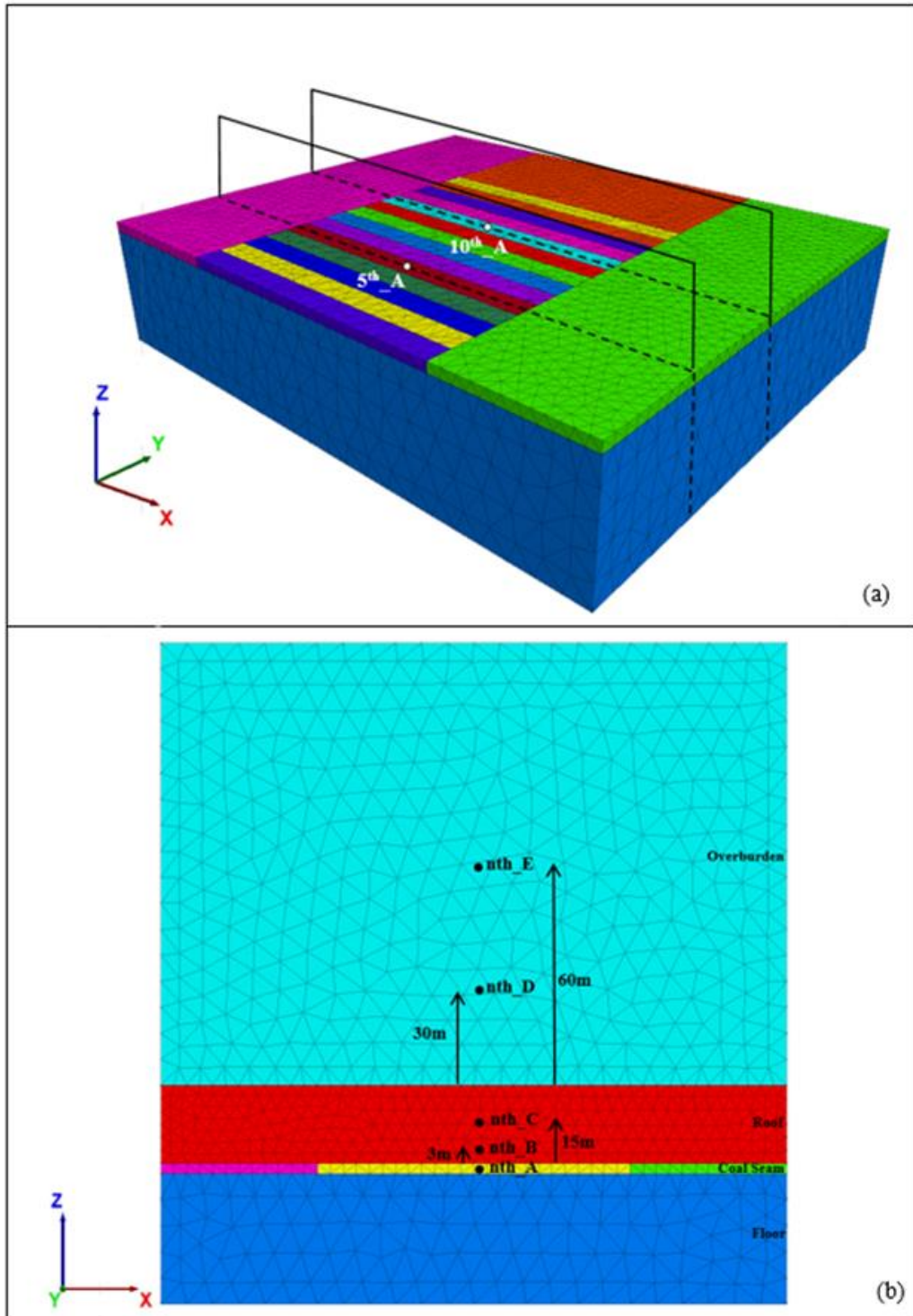


Figure 4.7. (a) cutting planes of 5th and 10th panel slices (b) cross-sectional view of “nth” layer

CHAPTER 5

RESULTS AND DISCUSSION

As mentioned before, we will analyze major and minor principal stress values obtained from the history points related to the 5th and 10th coal slices in both continuum and discontinuum models. It is worth noting that continuum models did not include any type of discontinuities or fractures inside them, but they imitate the discontinuum behavior by having input parameters of respective angled samples from the experimental stage. By that, we will be able to compare outcomes of the discontinuum model that actually contains a coal seam with a certain fracture orientation - 60°, for example, and the continuum one that has coal mass imitating discontinuum characteristics of the rock-like sample having 60° degree fractures. It is worth mentioning that the orientations inside the coal seam can also be reviewed in the advancement direction through the panels. As the excavation advances, stress behavior inside the coal seam, immediate roof, roof, and overburden will be studied.

5.1 Analysis of Major Principal Stresses from the History Points Located Inside Coal Seam in Different Scenarios

5.1.1 Comparison of σ_1 Values Acquired from the History Point 5th_A from the Continuum and Discontinuum Models

Firstly, major principal stress data acquired from point 5th_A, in other words, from the history point located in the center of the 5th coal slice in 8 different discontinuum models, is given in Figure 5.1. Among the models to which hydrostatic stress condition was applied, the least σ_1 accumulation during the preliminary excavation stages can be observed in the model bearing coal fractures oriented with 60°. This was the case until we reached the face of the 5th coal slice itself, where the order of

σ_1 accumulation from the least to the most concentrated changed. The model having fracture orientation of 90° ends up having the highest σ_1 concentration of 5.8 MPa. While talking about safety aspects in the face, among all simulations with hydrostatic stress conditions, the model M_DC_30deg_k1 can be mentioned as the safest case by having 5 MPa of major principal stress. It is also worth mentioning that, history point inside the mentioned coal slice could not record the further excavation stages as it was also removed after the 5th excavation stage.

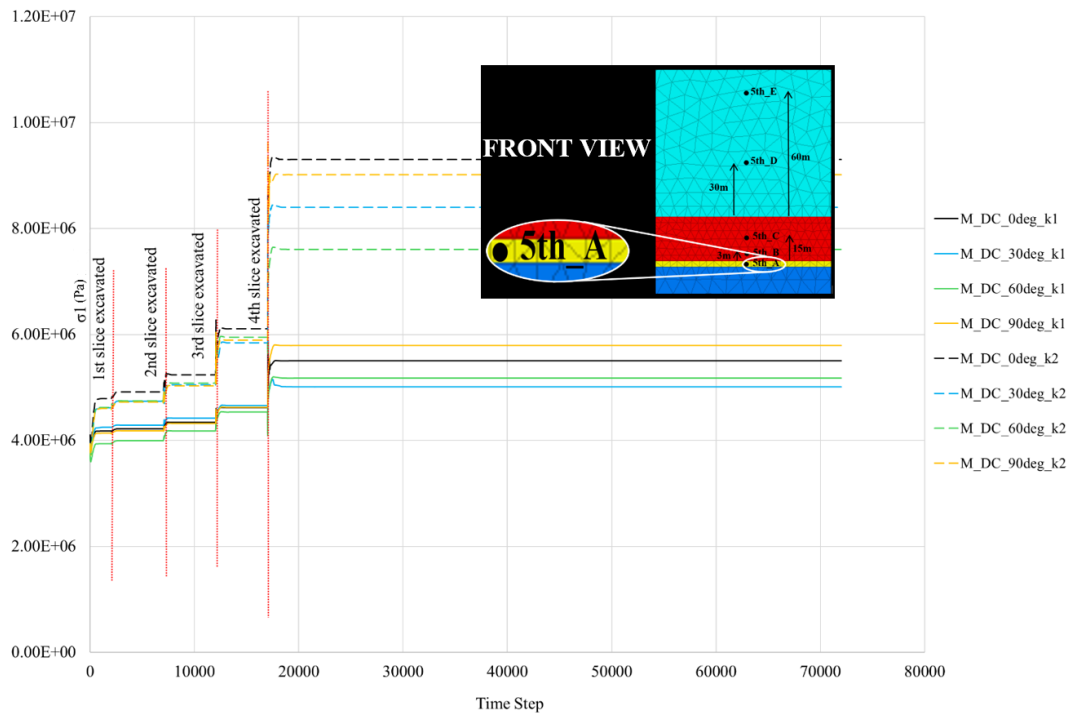


Figure 5.1. Comparison of σ_1 values (Pa) from the history point located inside the 5th coal slice (5th_A) in different discontinuous cases

For the second set of models, where k ratio was equal to 2, data recorded from the 5th_A was highest in the model M_DC_0deg_k2 for all of the excavation stages. Additionally, a sharp increase of 1.5 times from 6.1 MPa to 9.3 MPa can be seen in the last stage – where the 4th slice was excavated, and we reached the face of the 5th panel slice. The poorest increase was observed for the 60° degree model - an increase of 30% approximately, which makes it the safest option regarding face problems.

When it comes to the continuum models, it can be clearly seen from Figure 5.2 that ordering from the least to most concentrated stress-bearing cases in the models with hydrostatic stress conditions stays the same during all of the excavation stages. Moreover, the major principal stress concentration increases with an increase in the represented orientations of the coal cleat systems. However, after the advancement of 40 meters, there was a sharp increase of 30% in higher degreed models – specifically in M_C_90deg_k1 while models M_C_0deg_k1 and M_C_30deg_k1 preserved their trend. In fact, this type of sudden spike can also be observed during the earlier stages in the model with the representation of an orientation of 90° when the 3rd slice was excavated, σ_1 values got elevated with a rate of 35% from 4.75 MPa to 6.4 MPa.

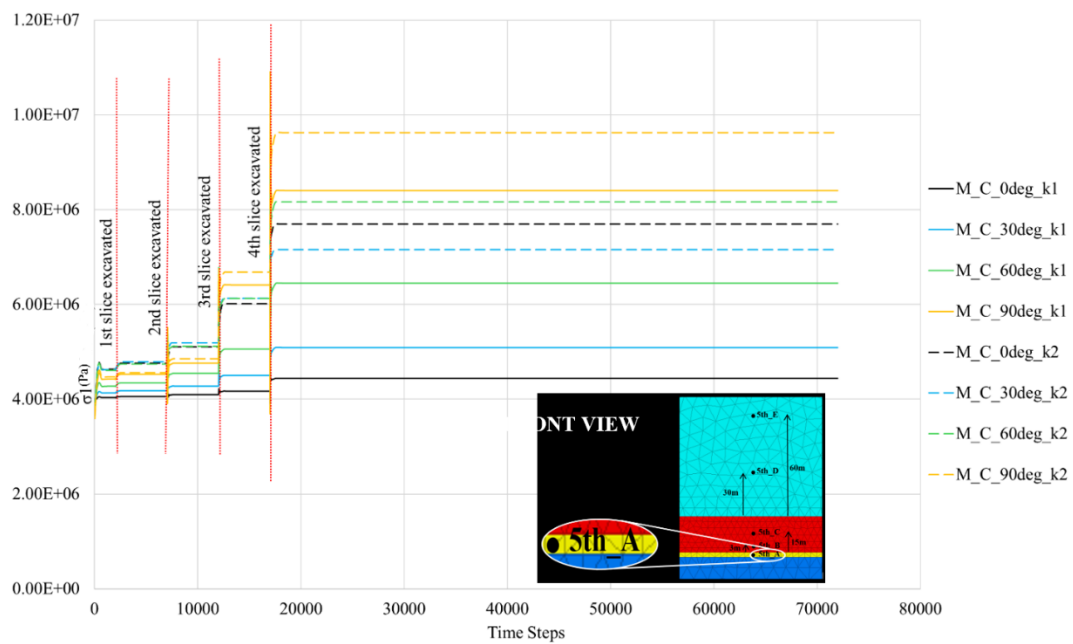


Figure 5.2. Comparison of σ_1 values (Pa) from the history point located inside the 5th coal slice (5th_A) in different continuous cases

For the models in which k=2, model M_C_90deg_k2 showed a similar behavior. After 30 meters of advance, data from σ_1 history point inside the 5th slice increased at a rate of 38%, and for the next 10 meters, it became 43% and reached a final value of 9.6 MPa. However, this was not the case for previous excavation stages; even that

specific model showed the poorest major principal stress trend for excavation of the first three panel slices. One specific thing that stays the same for both sets of models with two different stress conditions is that the recorded highest stress values as we excavated 4th last slice correspond to the models representing coal orientation of 90°. It was also the case with the discontinuum models with hydrostatic stress condition. Another point that is worth attention is that for the same stage, the lowest stress rate was observed in the model representing cleat structures with 30°.

5.1.2 Comparison of σ_1 Values Acquired from the History Point 10th_A from the Continuum and Discontinuum models

As the excavation advanced, major principal stress results from the history point 10th_A, which was located in the center of the 10th coal slice, were also plotted in the graph (Figure 5.4). For the discontinuum models with $k=1$, it can be seen that the model with M_DC_60deg_k1 accumulates the stress the most at all stages of the excavation until we reach the face of the 10th panel slice itself. While comparing these outcomes with the exact results obtained from the history point 5th_A, it is important to highlight that the model having fracture orientation of 60° showed the lowest rates of stress concentration in contrast to point 10th_A. This finding reports that while face problems in that exact model are less likely to occur during the excavation of preliminary panels, their chance of occurrence increases with the advancement of excavation in the further coal slices. For more detailed analysis, top view of maximum principal stress contours on the face of 5th and 10th coal slice of discontinuum model with angle of 60° ($k=1$) can be observed in the Figure 5.3.

At that mentioned advancement of 90 m, the ordering of stress patterns changed, and the model M_DC_30deg_k1 showed a sharp increase of approximately 40% and ended up having the highest stress concentration of 6.8 MPa, while the model M_DC_60deg_k1 showed only 13% change as shown in Figure 5.4. The lowest change belonged to the model having a fracture orientation of 90°.

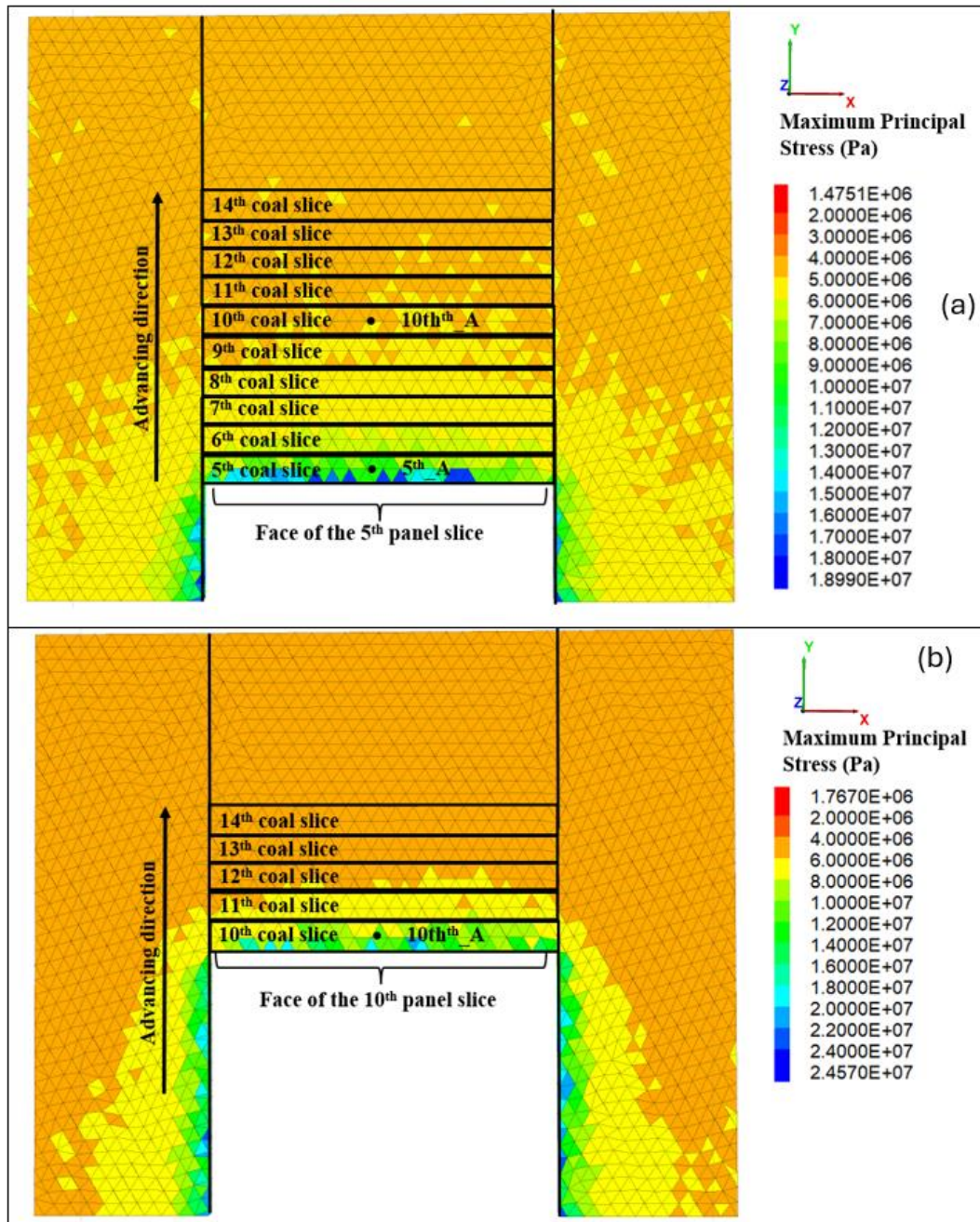


Figure 5.3. Top view of maximum principal stress contours on the face of (a) 5th and (b) 10th coal slice in the discontinuum model having orientation of 60° (k=1)

For the second set of models with k=2, the trend of the model with 60° shows similar behavior until the advancement of 80 m. In that particular moment, the highest concentration of major principal stress corresponds to the model M_DC_30deg_k2.

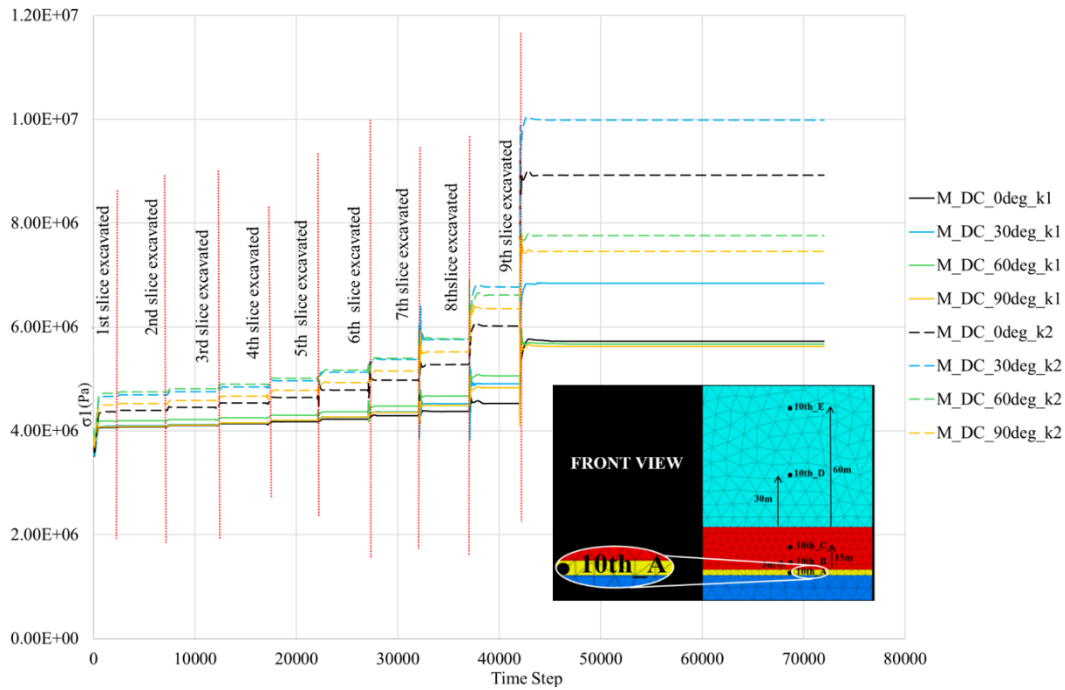


Figure 5.4. Comparison of σ_1 values (Pa) from the history point located inside the 10th coal slice (10th_A) in different discontinuous cases

After the excavation of 10 additional meters, when the face of the 10th was reached, a M_DC_30deg_k2 maintained its trend and continues to be the riskiest scenario in terms of face problems by reaching 10 MPa. Stress increase for that model at the end of the last stage was approximately equal to 50%, while for the most secure model with an angle of 90°, it was only equal to 17%. From the results, it is clear that the most and least safe options stay the same for discontinuum models despite the in-situ stress conditions of the two groups.

Regarding the continuum models, it can be seen from Figure 5.5 that for the models with hydrostatic stress conditions, stress concentration increases with the increase in the imitated fracture orientation. This means that, in all excavation stages, the highest data recorded from point 10th_A belonged to the model M_C_90deg_k1 and, respectively, the lowest to the model M_C_0deg_k1. It is worth noting that it was also the case for the data acquired from the point 5th_A for the models with the same stress conditions. When the face of the 10th panel slice was reached, the highest

incrementation was also observed in the model M_C_90deg_k1, which was equal to 53%, recording the change from 6.9 MPa to 10.5 MPa at the last stage.

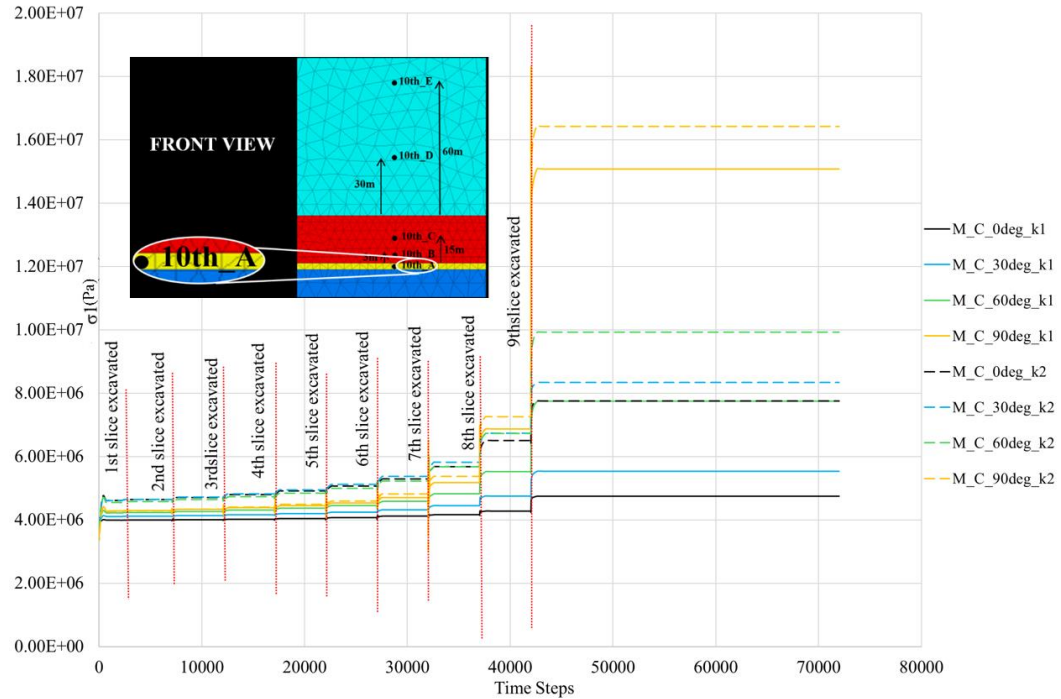


Figure 5.5. Comparison of σ_1 values (Pa) from the history point located inside the 10th coal slice (10th_A) in different continuous cases

At the same time, the poorest increase belonged to the model M_C_0deg_k1, which was equal to 11%. This analysis also revealed that the higher the imitated coal cleat degree, the higher the occurrence rate of face problems in the continuum models with hydrostatic stress conditions. However, different patterns were achieved in the models having a horizontal-to-vertical stress ratio of 2. For the first eight excavation stages, or in other words, for the advancement of 80 meters, the model M_C_90deg_k2 showed the lowest stress concentration while the other models showed very close results to each other. After the 8th slice was excavated, a sharp increase of 35% can be observed, which was followed by an increase of 2.25 times at the next stage. While for the other models, for example, the model M_C_0deg_k2 that increase was only equal to 19% while the face of 10th slice was reached. In the

end, we can say that for both sets of models with two different stress conditions, the lowest and highest stress accumulations on the face of the focused slice corresponded to the same degrees of 0° and 90°, respectively.

While comparing data acquired from the history points inside the 5th slice and 10th slices in the continuum models, it can be seen that for the both stress conditions, the highest stress-bearing model stay the same despite the point from where data was recorded. It means that, for the initial and last excavation stages, the most concerning case in terms of face problems is the model which imitates coal cleat with an orientation of 90°. However, these results did not overlap with the all of the results from the discontinuum models. For the further coal slices, riskiest scenario belonged to the model M_DC_30deg_k1. Only M_DC_90deg_k1 among the discontinuum models was the most concerning case when the face of 5th panel slice reached. While comparing that exact model with its respective continuous pair, it can be observed that while maximum stress of 5.8 MPa was recorded for discontinuous model, this value was equal to 8.4 MPa in continuous simulation. Results demonstrate that when fractured material was modeled in the continuous media, there is a difference rate of 45%. We can also conclude that for the coal layer, continuum simulations demonstrate more accurate results for the preliminary stages of excavation.

5.2 Analysis of Minor Principal Stresses from the History Points Located Above the Coal Slices (3 meters high on the immediate roof) in Different Scenarios

5.2.1 Comparison of σ_3 Values Acquired from the History Point 5th_B from the Continuum and Discontinuum models

In this section, an analysis of minor principal stress data collected from the points located on the immediate roof of the 5th and 10th slices in continuum and discontinuum media will be carried out. For now, we will compare recorded results

from point 5th_B for two different stress-conditioned sets of discontinuum models, as illustrated in Figure 5.6.

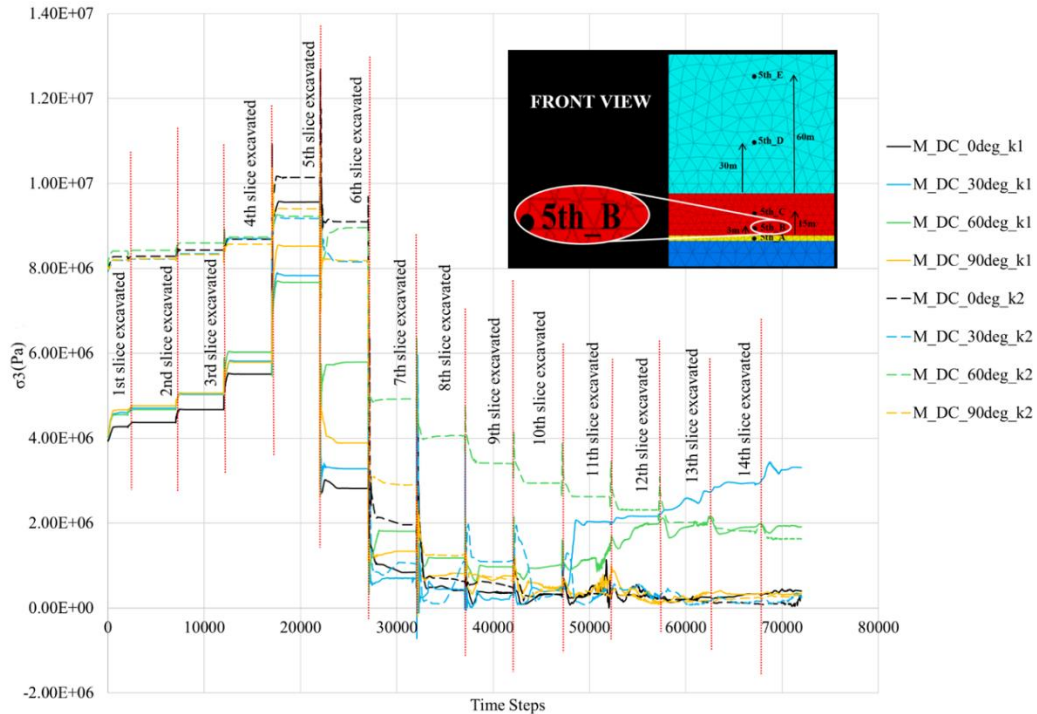


Figure 5.6. Comparison of σ_3 values (Pa) from the history point located above the 5th coal slice - 3 meters high on the immediate roof (5th_B) in different discontinuous cases

When hydrostatic stress condition was applied, the least σ_3 accumulation on the immediate roof of the 5th panel slice was observed in the model having fractures with an orientation of 0°. It was the case until the advancement of 40 m, where the face of the 5th slice was reached. At that exact time, that model showed the sudden increase of 73% and risk of rock burst on the immediate roof occurred. After we excavated the panel slice beneath the history point 5th_B, a sharp decrease from 9.5 MPa to 2.8 MPa can be observed in the values of σ_3 of that exact model. After the excavation of the 7th slice, the drop in confinement stress can be explained by the fact that the mined coal seam no longer supports the rock mass above it. Consequently, the immediate roof experiences less confining pressure due to the weight of the

overlying rock being excavated and ends up being deformed. While the model M_DC_60deg_k1 showed the most dangerous behavior after the advancement of 30 m, an increase of only 28% was recorded when we reached the face of the 5th slice, which made it the safest option in terms of rock burst problems in the immediate roof. For that exact model, decrease of 25% can be observed after the panel slice beneath the history point 5th_B was excavated. For the models having a k ratio of 2, a similar pattern of the minor principal stress concentration can be observed when we reach the face of the 5th slice itself. A model with coal cleat orientation of 0° showed an increase of 16%, which was not as sharp as in the previous set of models with k=1. When the panel slice beneath the mentioned history point was excavated, confinement stress was conserved as it decreased from 10.1 MPa to 9.1 MPa, but it still remained the riskiest case because of the highest σ_3 accumulation in the immediate roof. After the advancement of another 10 meters, stress behavior changes to tensile one, as the unloading process took place after the excavation of the 6th slice.

Among the continuum models, model M_C_90deg_k1 had the lowest concentrations of σ_3 during the preliminary excavation stages, while model M_C_30deg_k1 showed the highest stress accumulation. When the face of 5th panel slice was reached, sharp increases until 7.8-8 MPa can be observed in Figure 5.7 for all of the models having k ratio of 1. The highest incrementation belonged to the model M_C_90deg_k1, with an increase rate of 47%. It is worth mentioning that, history point inside exact model experienced the poorest decrease of 35% when the coal slice beneath 5th_B was excavated. At that same stage, a noticeable unloading of 47% belonged to the model M_C_30deg_k1, which was followed by another decrease of 43% after the advancement of 10 m. Models having a horizontal-to-vertical stress ratio of 2 did not demonstrate very sharp stress changes during the preliminary excavation stages. After the advancement of 40 m, the highest σ_3 change can be observed in the data of model M_C_30deg_k2. While the mentioned model showed an increase of 21%, M_C_90deg_k2 was the model that had the poorest increase of 15%.

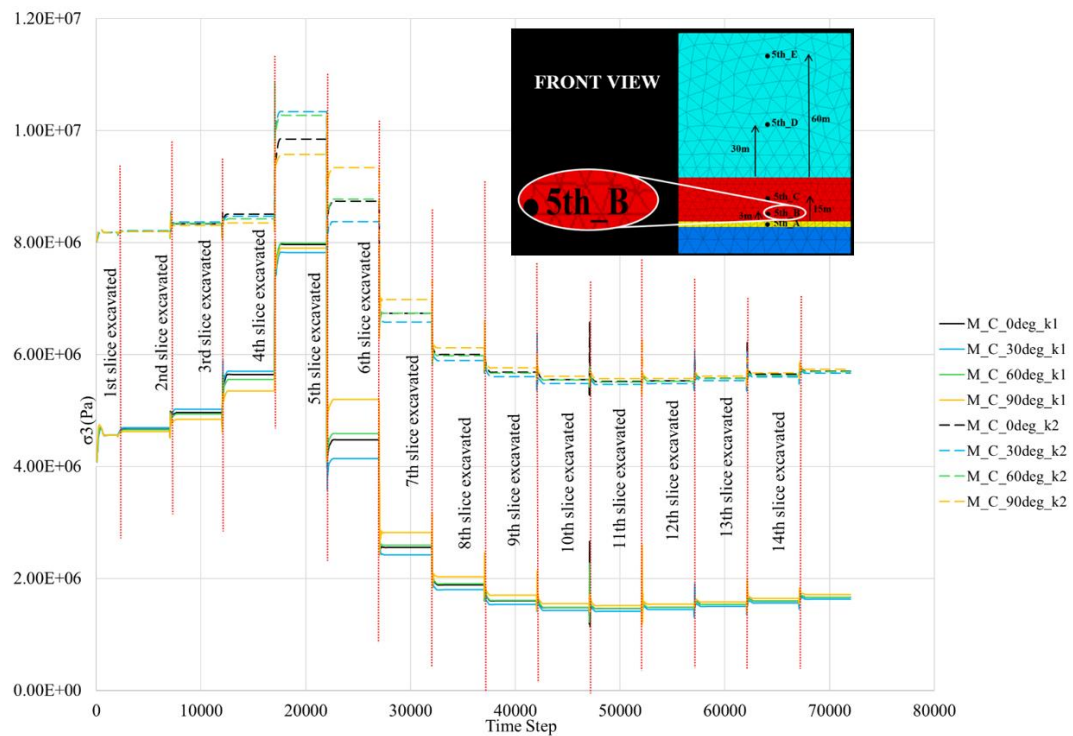


Figure 5.7. Comparison of σ_3 values (Pa) from the history point located above the 5th coal slice - 3 meters high on the immediate roof (5th_B) in different continuous cases

It is worth noting that M_C_90deg_k2 did not show a sudden decrease in the σ_3 data after the excavation of the 5th slice itself. In fact, it almost preserved its trend by only changing from 9.6 MPa to 9.35 MPa, while M_C_30deg_k2 experienced a decrease of 19%. More noticeable change of 25% in the data of M_C_90deg_k2 can be seen after the advancement of another 10 m - after the excavation of 6th panel slice. As a result, we can mention that for the second set of models having k=2, the model imitating coal cleats of 90° can be considered the safest option as it did not undergo a sudden reduction in confinement stresses after the 5th slice was excavated. In general, both sets of models with different stress conditions did not show any important changes in the data obtained from history point 5th_B after the advancement of 70-80 meters.

5.2.2 Comparison of σ_3 Values Acquired from the History Point 10th_B from the Continuum and Discontinuum Models

Now, we will compare the results obtained from the immediate roof of the 10th panel slice, in other words, from the point 10th_B. Until the face of the 10th slice was reached, all of the models showed very close values to one another among the ones to which the hydrostatic stress condition was applied. At that exact stage, the model M_DC_90deg_k1 showed the biggest change of 40%, which can be observed in Figure 5.8, and was increased to 9.7 MPa. At that stage, the model that had the poorest increase of 11% was the one that had coal cleats with a degree of 60°. From the mentioned conclusions, we can observe that when the face of the 10th slice was reached, the model with cleats of 90° was the most concerning one in terms of stability problems on the immediate roof, while the safest patterns belonged to M_DC_60deg_k1. As the 10th slice of coal itself was excavated, we can see that the biggest change in the data of minor principal stress belonged to the model M_DC_30deg_k1. The values dropped from 8.25 MPa to 2.25 MPa, showing a decrease of 3.65 times, which can result in deformation in the immediate roof as confinement stresses decrease sharply. Outcomes of the models with k=2 demonstrate that there was no strong accumulation of σ_3 during excavation stages as it was in the previous set of models. However, the highest increase in the values of stress can be observed in the model M_DC_90deg_k2 among this group of models as well when the face of the studied 10th slice was the topic of interest. While compared with the model which had k=1, this increase is only limited to the rate of 12%. The safest option was also the model with the same cleat orientation as was in the models with k=1, which corresponds to the degree of 60°. But that exact model showed the sharpest decrease when the coal slice beneath the history point 10th_B was excavated. It decreased 2.1 times by changing from 8.1 MPa to 3.8 MPa, while confinement stresses were preserved in other models. After the advancement of another 10 meters, confinement stress values of other models also decreased, and the yieldability of the immediate roof increased. The results also lead to the conclusion

that while for the models having $k=1$, sharper increases were observed in the data of point 10th_B as we came closer to the 10th slice, for the models having $k=2$, σ_3 changes were not that important.

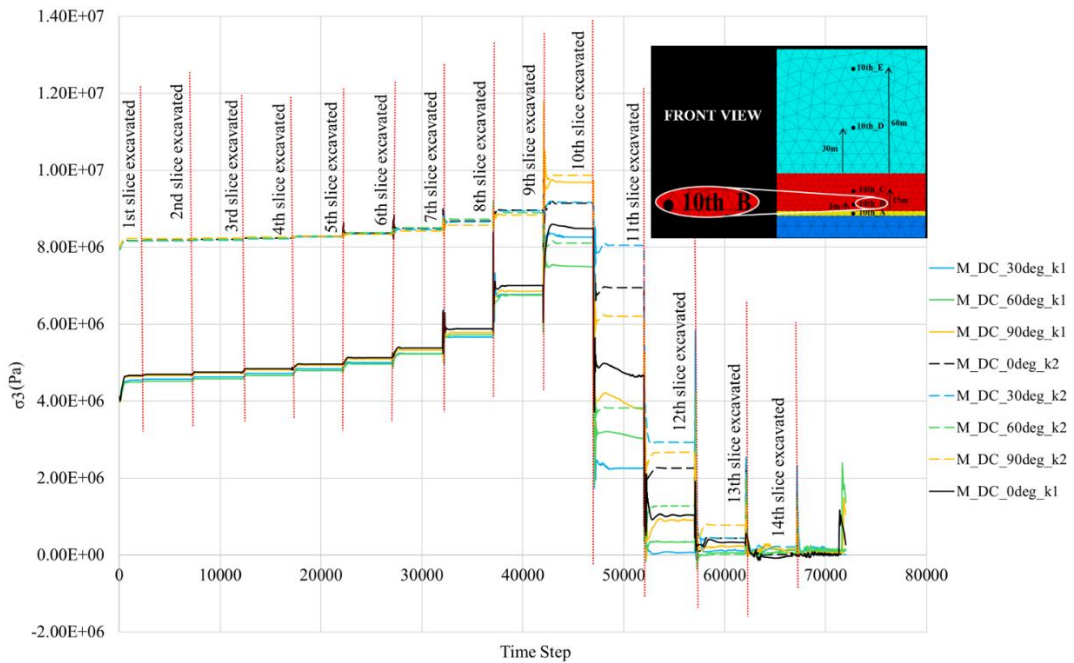


Figure 5.8. Comparison of σ_3 values (Pa) from the history point located above the 10th coal slice - 3 meters high on the immediate roof (10th_B) in different discontinuous cases

A similar type of behavior can be seen in Figure 5.9 for the continuous models with hydrostatic stress conditions. The concentration of minor principal stress values increased noticeably by around 20% for almost all of the models after the advancement of 80 m. When one more slice was excavated, the behavior of the model M_C_deg90_k1 differed from the rest by having the highest incrementation rate of 45%. Because of this sharp increase, this model can be interpreted as the riskiest case regarding the safety problems in the immediate roof when the face of the 10th slice was reached. On the other hand, the model imitating coal cleat structures with a degree of 30° showed an increase of 22% and was positioned in the lowest position among the models. These two models preserved their places as

the most and least concerning cases during the next stages as well. After the 10th slice was excavated, σ_3 values decreased by approximately 32% for both of the models, which can be explained by the absence of the rock mass beneath the history point 10th_B.

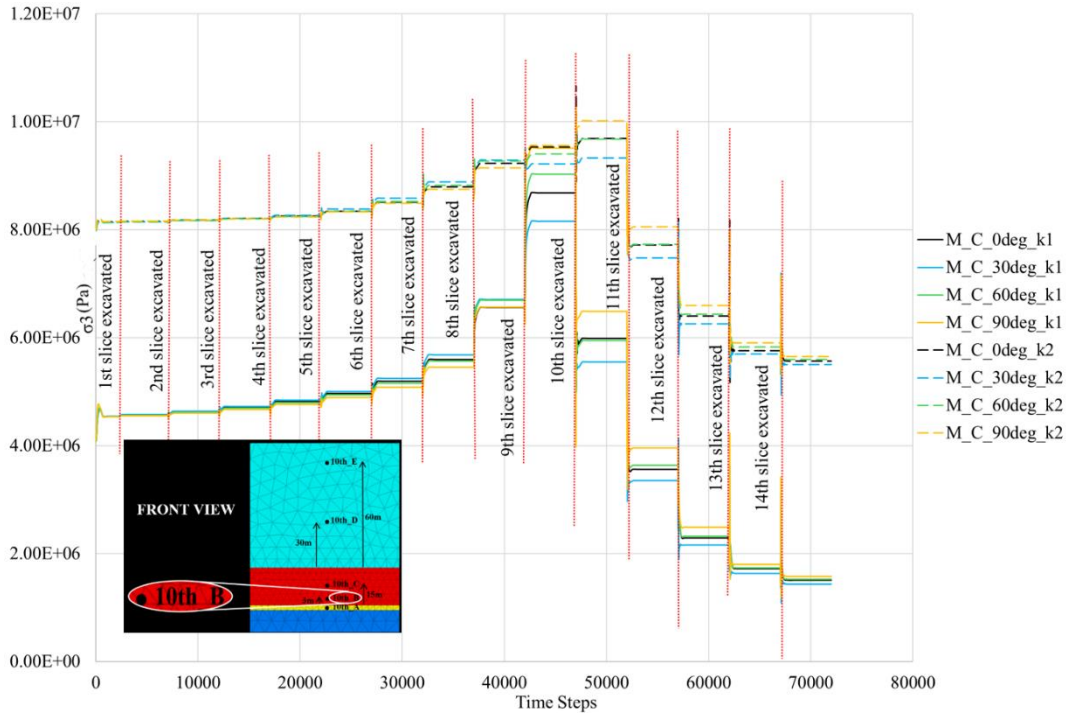


Figure 5.9. Comparison of σ_3 values (Pa) from the history point located above the 10th coal slice - 3 meters high on the immediate roof (10th_B) in different continuous cases

Meanwhile, there was no sharp increase in any of the models, with a horizontal-to-vertical in-situ ratio of 2 when the face of the focused slice was reached. The highest increase of only 5% was recorded from the model M_C_90deg_k2. In fact, data did not decrease as was in the previous set of simulations with k=1 after the excavation of the 10th slice itself. This means that the yieldability of the immediate roof was not decreased either, despite the fact that the rock slice beneath it was excavated. The safest and the most dangerous cases were also the same as the previous set of models, models representing coal cleats of 30° and 90°, respectively. This phenomenon continued with further advancements of 20-30 m. For the most concerning model,

the sharpest decrease was recorded after the 11th excavation stage, and it was approximately equal to 20%. From the comparison of 2 sets of models with different stress conditions, it can be said that while the immediate roof of the 10th slice showed immediate deformation when the slice beneath it was excavated for the models having $k=1$, models having $k=2$ demonstrated preservation of confining stress and did not change in sharp rates, in general.

Observations about the data from immediate roof demonstrate that, for the further development stages continuum models represent the behavior of fractured rock more accurately. It can be proven by the fact that after the excavation of 9th slice, most concerning cases in both discontinuum and continuum models was the models with fracture orientation of 90°. Also, for both discontinuum and continuum cases, models having $k=2$ conserved confining stresses even after the panel slice beneath them was excavated. Additionally, discontinuum models demonstrated sharp changes after the excavation stages compared with continuum simulations.

5.3 Analysis of Minor Principal Stresses from the History Points Located Above the Coal Slices (center of the immediate roof) in Different Scenarios

5.3.1 Comparison of σ_3 Values Acquired from the History Point 5th_C from the Continuum and Discontinuum Models

The history point recording the minor principal stress values, which will be analyzed in this section, is located closer to the surface. Data obtained from points 5th_C and 10th_C in different continuum and discontinuum models will be compared. Those points are located in the center of the roof above the 5th and 10th coal slices, more specifically, 15 meters above the coal seam.

While looking at the discontinuum models having a ratio of $k=1$, it can be observed in Figure 5.10 that after the advancement of 30 m, models having fracture

orientations of 30° and 90° showed an increase of 13% and 15% at their σ_3 data, respectively. When the face of the 5th slice itself was reached, the highest increase of 25% can be observed in the model with a cleat angle of 30°. While this model can be viewed as the most problematic one in terms of the roof problems, another concerning case was the model with an orientation of 90° that had an increase rate of 11%. At the same stage, the poorest increase from 5.1 MPa to 5.5 MPa belonged to the model M_DC_60deg_k1, which can also be considered the least concerning model.

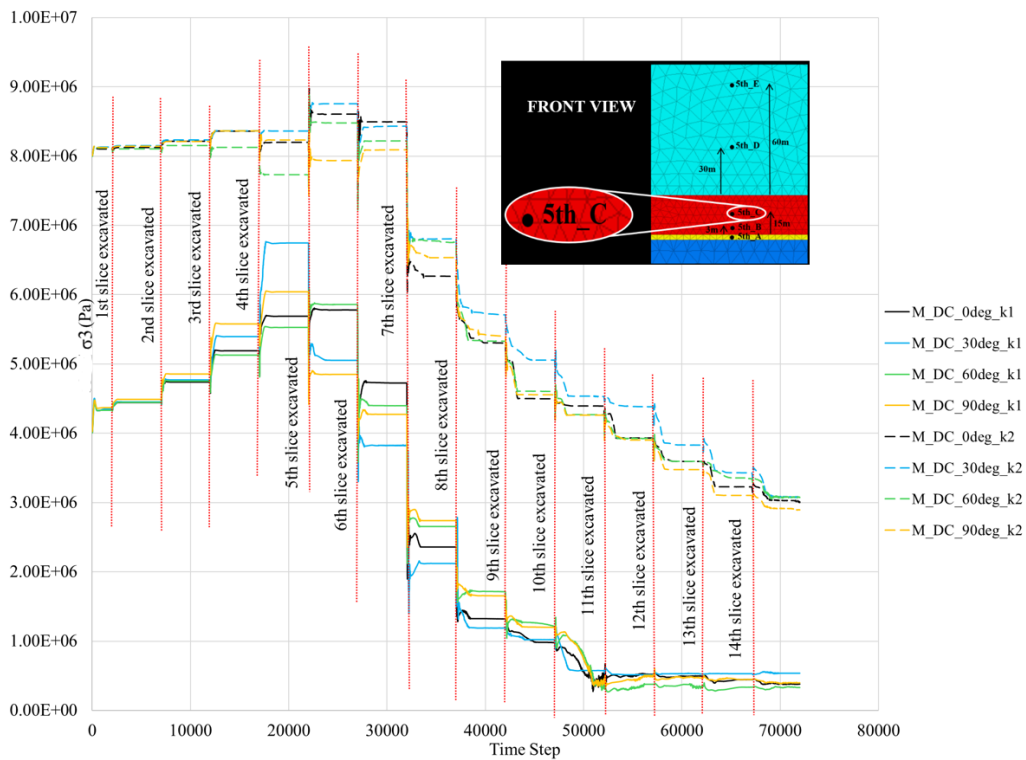


Figure 5.10. Comparison of σ_3 values (Pa) from the history point located above the 5th coal slice – the center of the immediate roof (5th_C) in different discontinuous cases

After the 5th slice was excavated, the mentioned two models with the highest stress accumulation - M_DC_30deg_k1 and M_DC_90deg_k1 showed more important changes as well. While they had respective reductions of 28% and 17% as a result

of decrease in the confining stresses, other two models showed the increasing behavior, in fact. Another point that takes attention is the fact that models, in general, did not completely show a very sharp decrease immediately after the excavation of the coal panel beneath the history point. While it was the case with the previous study of history points located on the immediate roof, models of this section preserved the effect of confining stresses until the advancement of another 20 m.

When analyzing discontinuum models with a k ratio of 2, it can be observed that there were not very important changes until the face of the 5th panel slice was reached. In this stage, data obtained from the models did not differ from each other at great rates as well. Despite this fact, we can say that models with the highest and lowest concentrations of σ_3 were M_DC_30deg_k2 and M_DC_60deg_k2, respectively. It was also the case after the exact advancement of 40 m among the models having hydrostatic stress conditions. After the 5th slice was excavated, a model with an orientation of 30° showed an increase of only 5% but preserved its place as the most concerning case when compared with another model. Another model in which minor principal data showed an increase of the same rate was the M_DC_0deg_k2, or in other words, having factures positioned perpendicular to the advancement direction. Confinement was decreased with low rates for almost all of the models until the 7th coal slice was excavated. While comparing with the previous set of models with k=1, similar behavior can be observed until the same stage. After the advancement of 70 m, the yieldability of the roof above the 10th slice decreased noticeably, approximately around the rate of 25%, from 8.5 MPa to 6.3 MPa for the model having a cleat orientation of 0°. Starting from that stage, confinement stresses declined gradually until the last stage of the excavation, while it was a sharp decrease for the models having hydrostatic stress conditions.

When hydrostatic stress condition was applied to the continuum models (Figure 5.11), data acquired from point 5th_C showed very similar patterns for all of the models until the panel slice underneath the same history point was excavated. Until that stage, after each excavation, minor principal stress values in the center of the roof increased gradually in the range of 5-10%.

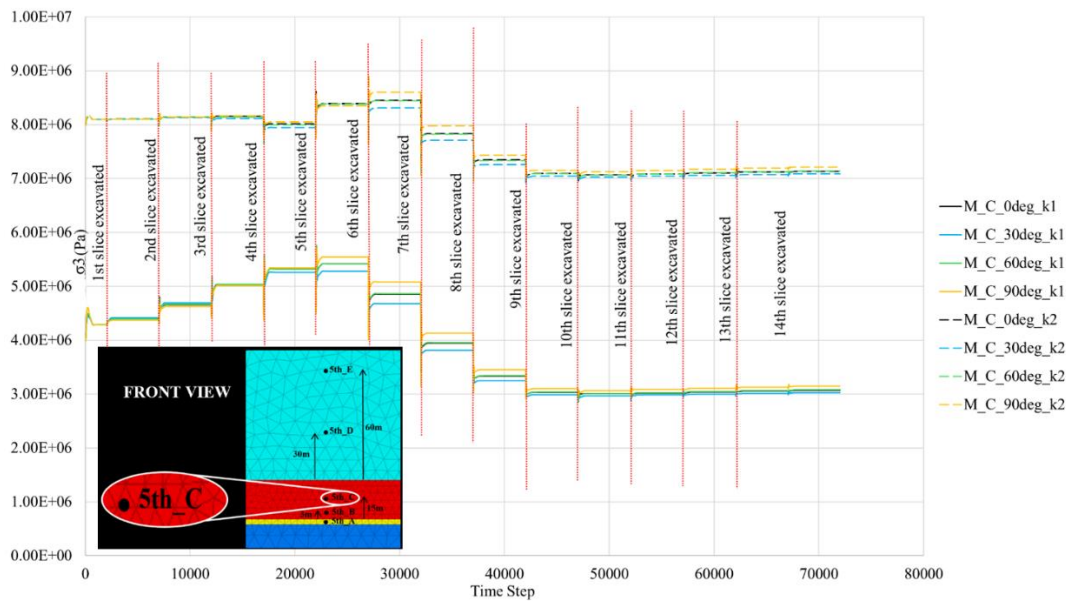


Figure 5.11. Comparison of σ_3 values (Pa) from the history point located above the 5th coal slice – the center of the immediate roof (5th_C) in different continuous cases

As the 5th slice was excavated, the model M_C_30deg_k1 had the lowest σ_3 concentration of 5.3 Mpa among the models, and the one M_C_90deg_k1 had the highest concentration of 5.55 MPa. After that stage, it is obvious that those models protect their places as the least and most concerning cases regarding the yieldability problems on the roof for the advancement of the next 20-30 m. However, during that stage, minor principal stress values got decreased gradually because the overlying rock mass experienced unloading. For example, the history point inside the model M_C_90deg_k1 showed decreases with the ordering of 7%, 20%, and 15% after the excavations of the 6th, 7th, and 8th slices, respectively. In contrast, those values were equal to 12%, 19%, and 15% for the data obtained from the history point inside the model M_C_30deg_k1.

Models with a horizontal to vertical in-situ stress ratio of 2 showed very small changes in the data collected from point 5th_C until the advancement of 40 m. In fact, when the face of the 5th panel slice was reached, there was a very poor decrease of 2-5%, which was later followed by an increase of approximately 5% when another

10 m was excavated. The highest recorded data belonged to the model M_C_90deg_k2, showing the value of 8.6 MPa after the 6th slice was excavated. At that exact moment, the model M_C_30deg_k2 was the model that accumulated the least amount of minor principal stresses of 8.3 MPa. The same pattern was observed for the previous set of continuum models with hydrostatic stress conditions. In fact, those two models took their places as most and least stress accumulating cases immediately after the 5th slice of coal got excavated, when with this model, it is happening after the advancement of 1 additional slice. Until the excavation of the 9th panel slice, this trend was preserved, but confining stresses got lesser. For both sets of models with two different stress conditions, excavation of the coal slices after the advancement of 90 m did not hugely affect the stress concentration data recorded from point 5th_C.

5.3.2 Comparison of σ_3 Values Acquired from the History Point 10th_C from the Continuum and Discontinuum models

Data acquired from the history point 10th_C from the discontinuum models showed that when the hydrostatic stress condition was present, a model having a fracture orientation of 30° accumulated more stress than other models until the face of the 10th slice was reached. From Figure 5.12, it can be seen that the exact model had the highest σ_3 value of 6.9 MPa, while the model that had the lowest stress value of 5.3 MPa was the one that had fractures positioned perpendicularly to the advancement direction. After the excavation of the 10th slice, M_DC_30deg_k1 suddenly decreased by 17%, which can be interpreted as a reduction in the yieldability of the roof. On the opposite, the spike can be observed in the data of the model M_DC_0deg_k1, and confinement was almost preserved for other models. After the advancement of another 10 m, the only model that did not show a sharp decrease was the one that had fractures parallel to the advancement direction; in other words, a model M_DC_90deg_k1. A sharp decrease from 6.4 MPa to 3.9 MPa was observed for the model having a fracture orientation of 60°.

History points inside roofs of the models having a k ratio of 2 did not show very sharp changes until the advancement of 90-100 m. When the face of the 10th slice was reached, the highest σ_3 data belonged to the model M_DC_60deg_k2 by having a value of 8.9 MPa.

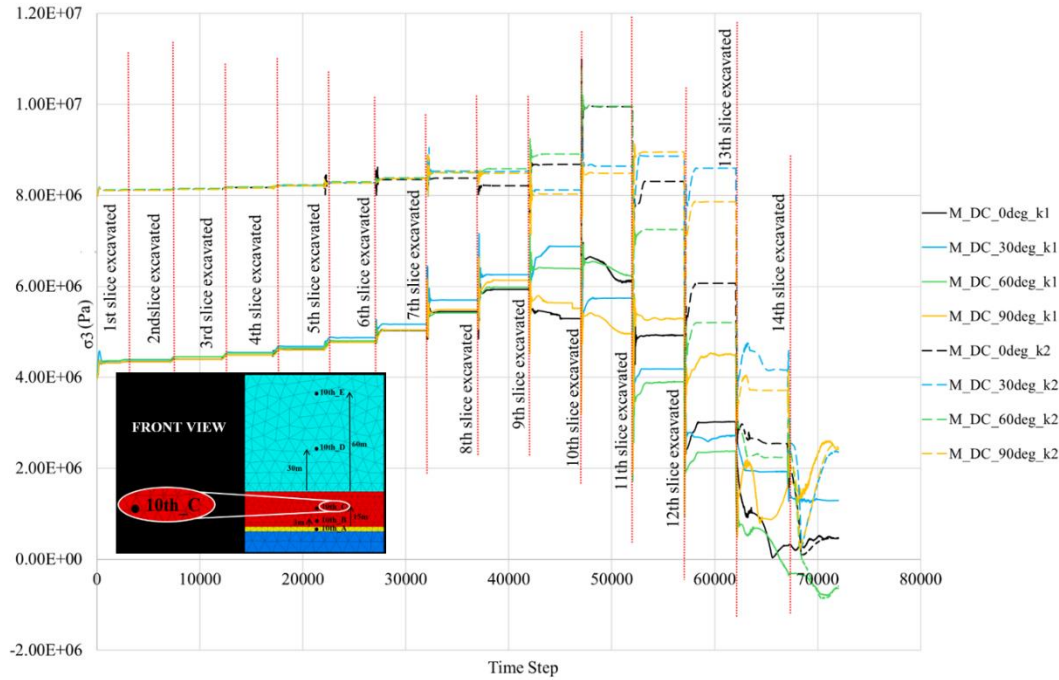


Figure 5.12. Comparison of σ_3 values (Pa) from the history point located above the 10th coal slice – the center of the immediate roof (10th_C) in different discontinuous cases

After the advancement of another 10 m, the exact model showed an increase of approximately 12% and reached the value of 9.9 MPa. The model having coal cleats with a fracture orientation of 0° shared the exact same position as the mentioned model after the excavation of the 10th slice. At that stage, the model with the lowest stress concentration of 8.5 MPa was the M_DC_90deg_k2. It can be observed that, after the excavation of the 11th panel slice, these two least and most stress-accumulated cases switched their places. While M_DC_0deg_k2 underwent a sharp decrease of 27% and became the least concerning case in terms of roof stability, a model with orientation of 90° showed a small increase and continued to accumulate

stress. For the advancement of the next 10 m, another decrease of 28% was observed for the model M_DC_60deg_k2, which means that it could not preserve confining stresses and deformed. A model with coal cleats of 90° also underwent a decrease from 8.95 MPa to 7.85MPa.

During the analysis of continuum models, it can be clearly seen from Figure 5.13 that while models with hydrostatic stress conditions showed an increase in minor principal stress values after each excavation stage, the second set of models with $k=2$ preserved the stress concentrations around the in-situ stress value of 8 MPa during the preliminary stages. The sharpest increase among the first set of models can be observed when the face of the 10th slice is reached. Until then, the model M_C_30deg_k1 had slightly higher values of minor principal stress, and the model M_C_90deg_k1 accumulated stress less than all other models, but it showed the highest increase of 21% when that particular face was reached. After the slice beneath point 10th_C was excavated, the mentioned model was able to preserve its confinement, while the model M_C_30deg_k1 showed a decrease of 14%. Other noticeable changes happened after the excavation of the 11th panel slice, which preserved the places of models M_C_30deg_k1 and M_C_90deg_k1 as the lowest and highest stress-bearing cases. While the model imitating cleats of 90° underwent a stress decrease of 37%, for the model representing 30°, this value was equal to 33%. These rates can be interpreted as the important deformation representatives after the advancement of a further 10 m that followed the excavation of a coal slice beneath the history point.

For the second set of models having a horizontal-to-vertical stress ratio of 2, stress behaviors started to differ from one another after the panel slice beneath the focused 10th history point was excavated. As was the case with the previous set of hydrostatic models, the sharpest increase belonged to the model M_C_90deg_k2. One point that takes attention is that the mentioned increase is not as sharp as was the case with the previous set of models; more specifically, it was equal to 13% and happened after the excavation of the 10th slice, while for the hydrostatic stress applied models, incrementations happened when the face of 10th slice was reached.

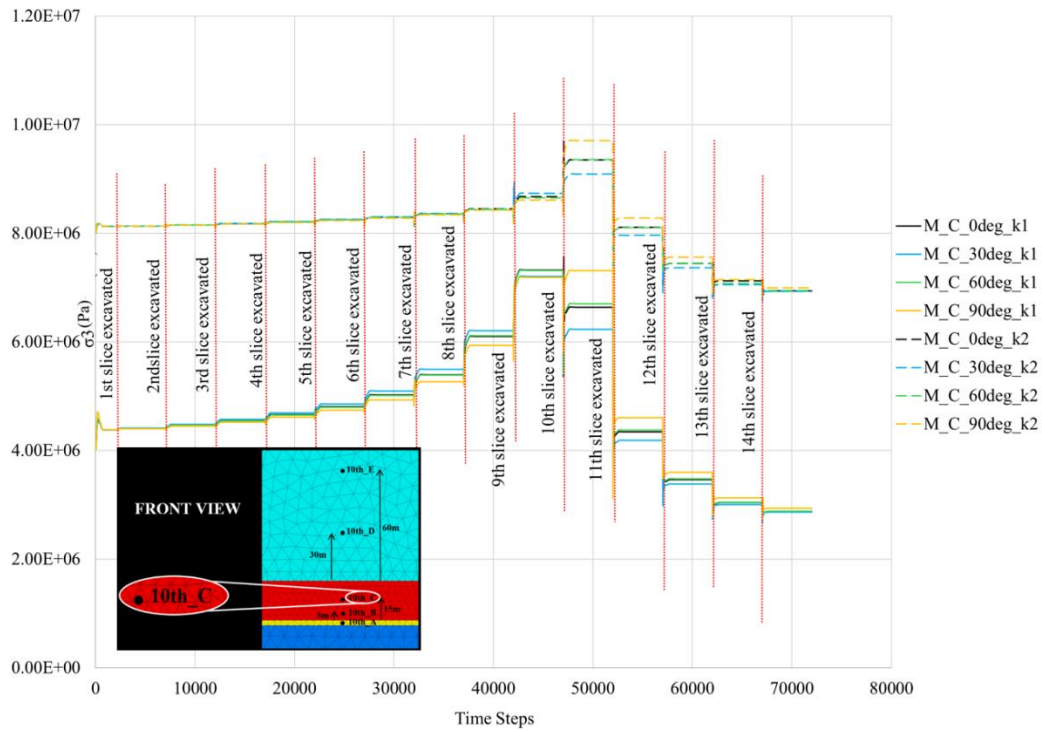


Figure 5.13. Comparison of σ_3 values (Pa) from the history point located above the 10th coal slice – the center of the immediate roof (10th_C) in different continuous cases

The poorest increase belonged to the model M_C_30deg_k2, with a rate of only 4%. Increases were followed by decreases of 15% and 12% after the advancement of another 10 m for the models M_C_30deg_k2 and M_C_90deg_k2, respectively. In general, it can be observed that while for the models having $k=1$, stress changes recorded from the history point 10th_C were sharper during the excavations around the 10th coal slice, that was not the case for the second group of models having $k=2$. They were accumulating σ_3 at higher rates, and the confining stresses decreased importantly during the last stages. While comparing data with discontinuum models, the ordering of the models from lowest to highest stress-bearing cases stayed the same during most of the excavation cases and belonged to the models that represented coal cleats of 30° and 90° for the continuum simulations.

Review of history points located in the center of the roof revealed that, as we go closer to the surface, recorded highest stress concentrations tend to appear not directly after the excavation of mentioned coal slices, but after further advancements of 10 m.

5.4 Analysis of Minor Principal Stresses at the Overburden and Deviatoric Stresses in Different Depths

Stress data obtained from the history points located in the overburden proves that the influence of excavation becomes lesser and lesser as we approach the topographic surface. This phenomenon can be clearly observed while comparing history points 5th_D and 5th_E, or 10th_D and 10th_E (Appendices A and B), which were located 30 and 60 m high on the overburden, respectively. For both continuum and discontinuum models, changes after the excavation stages were recognizable in the data obtained from points 5th_D and 10th_D when the hydrostatic stress condition was applied. However, continuum models had almost the same behavior, and stress paths were not distinguishable despite the imitated coal cleat angle. The measured highest value from point 5th_D (Figure A.2) among continuum models with hydrostatic stress condition was equal to 4.2 MPa, which was recorded after the excavation of the 5th slice itself and maintained its value for another advancement of 10 m. In contrast, discontinuum models showed slight differences with respect to each other (Figure A.1), and the highest stress concentration of 4.2 MPa also belonged to model M_DC_90deg_k1. After that stage, confining stresses began to decrease gradually until the excavation of the 9th panel slice.

Similar patterns can be observed while analyzing the data obtained from the history point 10th_D, which is located above the 10th coal slice. In general, stress confinement was preserved around the given in-situ stress value until the advancement of 60 m and increased afterward. For discontinuum models, a peak σ_3 value of 4.45 MPa was recorded (Figure A.3) in models with coal cleat degrees of 60° and 90° when the 10th panel slice was excavated and did not change for the further

advancement of 10 m. When comparing these results to continuum models, it can be observed that for all models, peak stress values around 4.2 MPa were reached (Figure A.4) after the excavation of the 11th coal slice. Results have also demonstrated that when the horizontal-to-vertical stress ratio equals 2, data obtained from points 5th_D and 10th_D in both continuum and discontinuum models did not show any important stress changes in the overburden after the excavation steps.

Overall, findings proved that the more distance from the excavation zones, the lesser effect can be observed in the minor principal stress patterns. It can be clearly observed during the analysis of data obtained from the history points 5th_E and 10th_E (Figure B.1, Figure B.2, Figure B.3, Figure B.4). In all continuum and discontinuum cases, whether the hydrostatic stress condition was present or not, all models demonstrated very similar behavior in the overburden, and infinitesimal changes were observed.

More detailed outcomes can be observed in the analysis of the deviatoric stresses based on the depth change. For that purpose, deviatoric stresses belonging to the continuum and discontinuum models with cleat orientation of 60° ($k=1$) was given in the Figure 5.14 and Figure 5.15. Series represent the deviatoric stresses calculated from data of different depths inside coal panel, roof and overburden related with the cross sectional plane of 10th coal slice. For the point 10th_A which was located in the center of 10th coal slice, both continuum and discontinuum models showed sharp changes in their deviatoric stresses after the advancement of 90 m and ended up having their maximum values of approximately 4.5 MPa. When it comes to the point 10th_B that was located in the immediate roof, differences between the continuum and discontinuum models can be clearly seen. While for the continuum simulation changes were gradual and smooth, discontinuum model showed more critical and complex behavior. Inside the continuum model, the highest deviatoric stress data from the history point 10th_B reached when the 10th coal slice itself was excavated, or in other words, rock mass beneath the mentioned point was removed. However, for the discontinuum model, the mentioned sharpest increase can be seen when the face of 10th coal slice was reached.

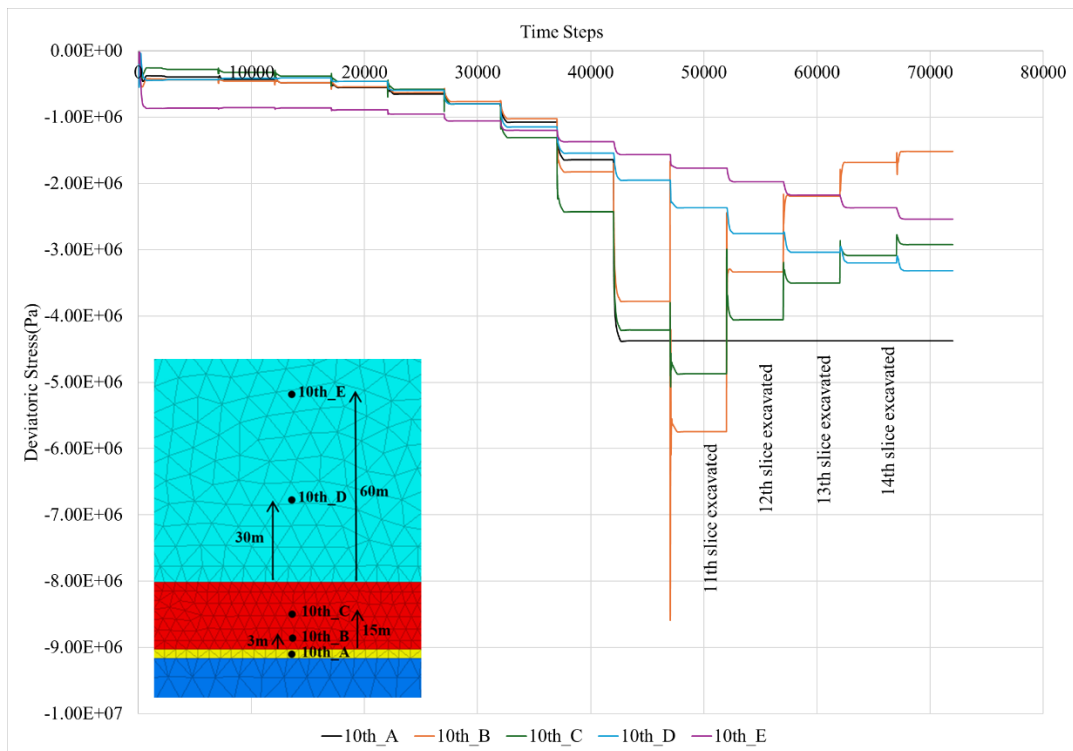


Figure 5.14. Deviatoric stress (Pa) analysis of points with different depths (Continuum model with orientation of 60° and $k=1$)

An increase of approximately 2.5 times from 2.5 MPa to 6.1 MPa was recorded after the 9th coal slice was excavated. Similar behavior was noticed for the deviatoric stresses from the point 10th_C located in the center of the roof. The continuum model showed increase of 16% in the roof after the 10th coal slice was excavated and by that, reached maximum deviatoric stress of 4.9 MPa. While compared with the discontinuum model, it can be observed that the sharpest increase of 60% was recorded after the excavation of 9th coal slice. In fact, the maximum value of approximately 5.3 MPa was preserved for the further advancement of 10 m.

Analysis of the points located on the overburden shows that, for both continuum and discontinuum cases stress fluctuations were not very significant and they demonstrate similar type of behavior. To conclude, the discontinuum model generally showed frequent sharp changes compared to the continuum model. The

continuum model represented more uniform and stable behavior, while deviatoric stresses in the discontinuum model had more complex and significant changes related with the presence of fracture sets and joints.

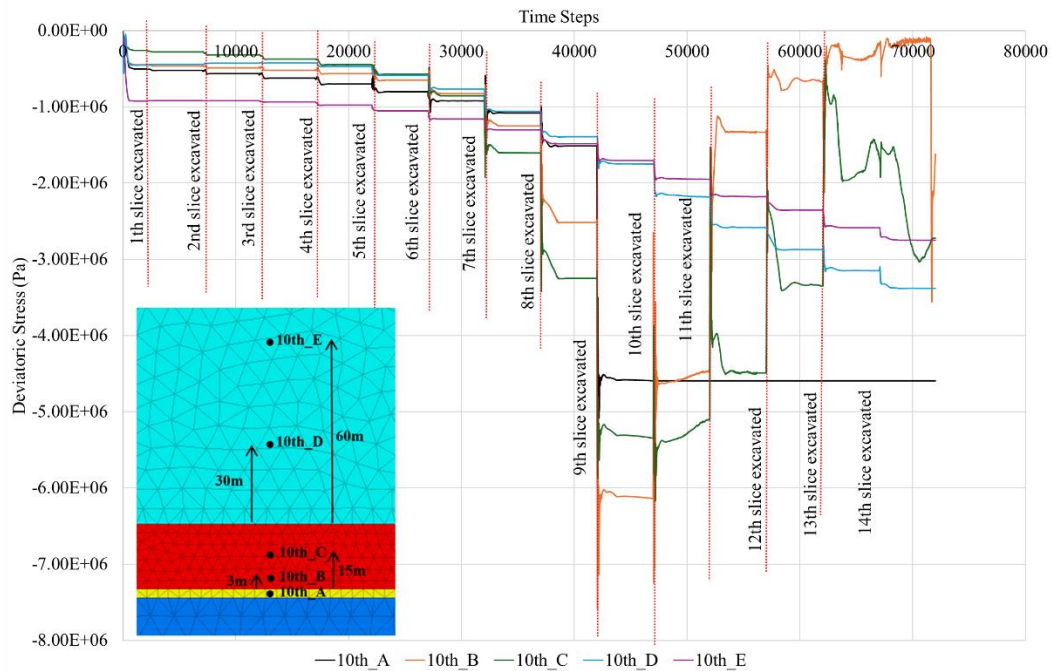


Figure 5.15. Deviatoric stress (Pa) analysis of points with different depths (Discontinuum model with orientation of 60° and $k=1$)

As consideration of discontinuities significantly impacts the stress distribution and overall stability, carried review highlights the limitations of the continuum modeling of fractured media one more time. Even after application of experimental data trends from laboratory test, continuum models could not show very similar outcomes to the discontinuum ones. It was proven that modeling of the fractured material in discontinuum environment gives more accurate and precise outcomes with respect to continuum medium.

CHAPTER 6

CONCLUSIONS

Using both experimental research and numerical simulations based on discrete fracture network (DFN) analysis, we have conducted an extensive assessment of coal cleat systems within longwall mines. Because of the structural nature of coal, various limitations have arisen during the previous studies. By combining 3D printing and molding techniques, we have proposed a new approach that enables the creation of samples with numerous connectivity types, angles, and designs. The study of complex behavior of cleated rock-like structures during laboratory experiments included UCS and static deformability tests. Some of the key findings in the experimental stage are:

- For the angular samples, linear and polynomial relationships between the fracture orientations and parameters such as E , ν , and UCS were obtained. Both LC and HC samples having fracture orientations of 90° had the highest Modulus of Elasticity and Poisson's ratio.
- It was proven that for almost all sample types HC ones showed higher outcomes in difference with the LC samples.
- Axial strain concentrated around the center of the sample 1.5-2 times more with respect to the points located far away from the midpoint for sample having fracture orientation of 0° .
- Analysis of blocked samples proved that fracture density or cleat dimensions influenced the strength of rock-like sample. Coarse-blocked samples deformed at higher rates when compared with fine-blocked ones. However, the mentioned factors did not play a huge role during the analysis of E and ν . In fact, BLL sample types for both coarse and finer block types demonstrated higher values of Modulus of Elasticity and Poisson's ratio with respect to BLS sample types.

Chapter 4 covers all the above-mentioned outcomes in a more detailed way. Numerical part of our study focused on the comparison of the continuous and discontinuous modeling of the fractured rock-like samples. The main goal here was to find out how accurately continuum-based code was able to simulate the behavior of discontinuous samples. For this purpose, data trends of angled samples obtained from the experimental part was modified and were entered to the continuum model. History points in the crucial zones as face, immediate roof and overburden in 16 different numerical simulations of Longwall Mine were reviewed in detail. Most concerning cases in terms of face and roof problems, stress accumulations after excavation stages for each case were studied. Outcomes showed that:

- When the obtained data trends from experimental part were used as input parameters in continuum models, outcomes were inconsistent with the results of discontinuum models in most of the cases. This concludes that the discontinuum modeling gives more critical results in fractured coal modeling.
- In general, discontinuum models showed frequent sharp changes after each excavation stages compared to the continuum models. Continuum models represented more uniform and stable behavior, while stresses in the discontinuum models had more complex and significant changes related with the presence of fracture sets and joints.
- For the entrance slices of the coal seam, the most problematic discontinuum case in terms of face problems was the model having fracture orientation of 90° when k was equal to 1. For the further excavation stages, recorded highest data at the face belonged to the discontinuum model with 30° ($k=1$). For mentioned preliminary stages, continuum simulations imitating also 90° demonstrate similar results by being most concerning case for both $k=1,2$. From those results, we can conclude that continuum simulations demonstrate more closer results to the ones of discontinuum models only for the preliminary stages of excavation inside panel when $k=1$, while it was not the case for further development.

- At the immediate roof, this relationship was in fact vice-versa. Results demonstrate that continuum models represent the behavior of fractured rock more accurately for the further development stages. When the face of 10th slice was reached, most concerning cases regarding problems in the immediate roof in both discontinuum and continuum models was the models with fracture orientation of 90°.
- It was also proved that data trends obtained from history points inside the overburden from same sub-grouped models behave in a very similar way. Additionally, there is lesser of an impact on the history points as they got farther from the excavation zones.

It is undeniable that inaccuracies during the experimental stage, such as sample preparation, data acquisition, and their application to numerical models, can result in infinitesimal errors among outcomes. Further studies could focus on the alternative approaches for the creation of coal-like material in the laboratory environment by testing out new designs, printing methods, and different fracture connectivity types. Also, new combined numerical methods could be proposed for the imitation of discontinuous medium in the continuum environment.

In summary, this thesis uses a combination of numerical and experimental analyses to better understand the behavior of coal cleats in longwall mines. We hope that the outcomes gathered from this study will contribute to the underground coal mining methods and make processes more efficient, safe and sustainable.

REFERENCES

- Andersson, J., & Dverstorp, B. (1987). Conditional simulations of fluid flow in three-dimensional networks of discrete fractures. *Water Resources Research*, 23(10), 1876–1886. <https://doi.org/10.1029/wr023i010p01876>
- Brook, M., Hebblewhite, B., & Mitra, R. (2016). Cleat aperture-size distributions: A case study from the Late Permian Rangal Coal Measures, Bowen Basin, Australia. *International Journal of Coal Geology*, 168, 186–192. <https://doi.org/10.1016/j.coal.2016.11.009>
- Cao, A., Liu, Y., Jiang, S., Qi, H., Peng, Y., Bai, X., & Yang, X. (2021). Numerical investigation on the influence of two combined faults and their structure features on rockburst mechanism. *Minerals*, 11(12), 1438. <https://doi.org/10.3390/min11121438>
- Cao, W., Lei, Q., & Cai, W. (2021). Stress-dependent deformation and permeability of a fractured coal subject to Excavation-Related loading paths. *Rock Mechanics and Rock Engineering*, 54(8), 4299–4320. <https://doi.org/10.1007/s00603-021-02520-0>
- Chen, Y., Zhang, Y., & Li, X. (2019). Experimental study on the influence of bedding angle on gas permeability in coal. *Journal of Petroleum Science and Engineering*, 179, 173–179. <https://doi.org/10.1016/j.petrol.2019.04.010>
- Cheng, X., Luan, H., Chen, L., Jiang, Y., & Han, W. (2021). Numerical investigation on mechanical properties of inhomogeneous coal under uniaxial compression and the role of cleat distribution. *Bulletin of*

Engineering Geology and the Environment, 80(9), 7009–7027.

<https://doi.org/10.1007/s10064-021-02357-5>

Crump. (1992). *Apparatus and method for creating three-dimensional objects*

(Patent No. U.S. Patent No. 5,121,329). U.S. Patent and Trademark Office.

Cundall, P., & Strack, O. D. L. (1979). A discrete numerical model for granular assemblies. *Geotechnique*, 29(1), 47–65.

<https://doi.org/10.1680/geot.1979.29.1.47>

Dawson, G. K. W., & Esterle, J. (2010). Controls on coal cleat spacing.

International Journal of Coal Geology, 82(3–4), 213–218.

<https://doi.org/10.1016/j.coal.2009.10.004>

Dershowitz, W., & Einstein, H. H. (1988). Characterizing rock joint geometry with joint system models. *Rock Mechanics and Rock Engineering*, 21(1), 21–51.

<https://doi.org/10.1007/bf01019674>

Durucan, Ş., & Edwards, J. (1986). The effects of stress and fracturing on the permeability of coal. *Mining Science & Technology*, 3(3), 205–216.

[https://doi.org/10.1016/s0167-9031\(86\)90357-9](https://doi.org/10.1016/s0167-9031(86)90357-9)

Einstein, H. H., Veneziano, D., Baecher, G. B., & O'Reilly, K. J. (1983). The effect of discontinuity persistence on rock slope stability. *International Journal of Rock Mechanics and Mining Sciences & Geomechanics Abstracts*, 20(5), 227–236.

[https://doi.org/10.1016/0148-9062\(83\)90003-7](https://doi.org/10.1016/0148-9062(83)90003-7)

Elmo, D., Stead, D., Eberhardt, E., & Vyazmensky, A. (2013). Applications of Finite/Discrete Element Modeling to rock Engineering Problems.

International Journal of Geomechanics, 13(5), 565–580.

[https://doi.org/10.1061/\(asce\)gm.1943-5622.0000238](https://doi.org/10.1061/(asce)gm.1943-5622.0000238)

Elsworth, D. (1986). A hybrid boundary element-finite element analysis procedure for fluid flow simulation in fractured rock masses. *International Journal for Numerical and Analytical Methods in Geomechanics*, 10(6), 569–584.

<https://doi.org/10.1002/nag.1610100603>

Feng, X., Gong, Y., Zhou, Y., Li, Z., & Liu, X. (2019). The 3D-Printing technology of geological models using Rock-Like materials. *Rock Mechanics and Rock Engineering*, 52(7), 2261–2277.

<https://doi.org/10.1007/s00603-018-1703-y>

Fereshtenejad, S., & Song, J. (2016). Fundamental Study on Applicability of Powder-Based 3D Printer for Physical Modeling in Rock Mechanics. *Rock Mechanics and Rock Engineering*, 49(6), 2065–2074.

<https://doi.org/10.1007/s00603-015-0904-x>

Gao, F., Stead, D., & Coggan, J. (2014). Evaluation of coal longwall caving characteristics using an innovative UDEC Trigon approach. *Computers and Geotechnics*, 55, 448–460. <https://doi.org/10.1016/j.compgeo.2013.09.020>

Gao, Y., Wu, T., & Zhou, Y. (2020). Application and prospective of 3D printing in rock mechanics: A review. *International Journal of Minerals, Metallurgy and Materials/International Journal of Minerals Metallurgy and Materials*, 28(1), 1–17. <https://doi.org/10.1007/s12613-020-2119-8>

Gell, E. M., Walley, S. M., & Braithwaite, C. (2019). Review of the validity of the use of artificial specimens for characterizing the mechanical properties of

rocks. *Rock Mechanics and Rock Engineering*, 52(9), 2949–2961.
<https://doi.org/10.1007/s00603-019-01787-8>

Ghazvinian, A., & Hadei, M. R. (2012). Effect of discontinuity orientation and confinement on the strength of jointed anisotropic rocks. *International Journal of Rock Mechanics and Mining Sciences*, 55, 117–124.
<https://doi.org/10.1016/j.ijrmms.2012.06.008>

Gosselin, C., Duballet, R., Roux, P., Gaudillière, N., Dirrenberger, J., & Morel, P. (2016). Large-scale 3D printing of ultra-high performance concrete – a new processing route for architects and builders. *Materials & Design*, 100, 102–109. <https://doi.org/10.1016/j.matdes.2016.03.097>

Guo, H., Yuan, L., Shen, B., Qu, Q., & Xue, J. (2012). Mining-induced strata stress changes, fractures and gas flow dynamics in multi-seam longwall mining. *International Journal of Rock Mechanics and Mining Sciences*, 54, 129–139. <https://doi.org/10.1016/j.ijrmms.2012.05.023>

Hodder, K., Nychka, J. A., & Chalaturnyk, R. (2018). Process limitations of 3D printing model rock. *Progress in Additive Manufacturing*, 3(3), 173–182.
<https://doi.org/10.1007/s40964-018-0042-6>

Hosseini, E., Sarmadivaleh, M., & Chen, Z. (2021). Developing a new algorithm for numerical modeling of discrete fracture network (DFN) for anisotropic rock and percolation properties. *Journal of Petroleum Exploration and Production Technology*, 11(2), 839–856. <https://doi.org/10.1007/s13202-020-01079-w>

Hou, L., Liu, X., Liang, L., Xiong, J., Zhang, P., Xie, B., & Li, D. (2020). Investigation of coal and rock geo-mechanical properties evaluation based

on the fracture complexity and wave velocity. *Journal of Natural Gas Science and Engineering*, 75, 103133.
<https://doi.org/10.1016/j.jngse.2019.103133>

Huang, Y., Yang, S., Tian, W., Zeng, W., & Yu, L. (2015). An experimental study on fracture mechanical behavior of rock-like materials containing two unparallel fissures under uniaxial compression. *Acta Mechanica Sinica*, 32(3), 442–455. <https://doi.org/10.1007/s10409-015-0489-3>

Hull, C. (1986). *Apparatus for production of three-dimensional objects by stereolithography* (U.S. Patent No. 4,575,330). U.S. Patent and Trademark Office.

Jiang, C., & Zhao, G. (2014). A preliminary study of 3D printing on rock mechanics. *Rock Mechanics and Rock Engineering*, 48(3), 1041–1050. <https://doi.org/10.1007/s00603-014-0612-y>

Jiang, L., Wang, P., Zheng, P., Luan, H., & Zhang, C. (2019). The influence of different advancing directions on the mining effect is caused by a fault. *Advances in Civil Engineering*, 2019, 1–10. <https://doi.org/10.1155/2019/7306850>

Jiang, Q., Feng, X., Song, L., Gong, Y., Zheng, H., & Cui, J. (2015). Modeling rock specimens through 3D printing: Tentative experiments and prospects. *Acta Mechanica Sinica*, 32(1), 101–111. <https://doi.org/10.1007/s10409-015-0524-4>

Jiang, Q., Liu, X., Yan, F., Yang, Y., Xu, D., & Feng, G. (2020). Failure performance of 3DP physical Twin-Tunnel model and corresponding safety

factor evaluation. *Rock Mechanics and Rock Engineering*, 54(1), 109–128.
<https://doi.org/10.1007/s00603-020-02244-7>

Jing, L., & Hudson, J. (2002). Numerical methods in rock mechanics. *International Journal of Rock Mechanics and Mining Sciences*, 39(4), 409–427.
[https://doi.org/10.1016/s1365-1609\(02\)00065-5](https://doi.org/10.1016/s1365-1609(02)00065-5)

Ju, Y., Wang, Y., Su, C., Zhang, D., & Ren, Z. (2019). Numerical analysis of the dynamic evolution of mining-induced stresses and fractures in multilayered rock strata using continuum-based discrete element methods. *International Journal of Rock Mechanics and Mining Sciences*, 113, 191–210.
<https://doi.org/10.1016/j.ijrmms.2018.11.014>

Karami, A., & Stead, D. (2007). Asperity degradation and damage in the Direct shear Test: A hybrid FEM/DEM approach. *Rock Mechanics and Rock Engineering*, 41(2), 229–266. <https://doi.org/10.1007/s00603-007-0139-6>

Kazemian, A., Yuan, X., Cochran, E., & Khoshnevis, B. (2017). Cementitious materials for construction-scale 3D printing: Laboratory testing of fresh printing mixture. *Construction and Building Materials*, 145, 639–647.
<https://doi.org/10.1016/j.conbuildmat.2017.04.015>

Kong, L., Ostadhassan, M., Li, C., & Tamimi, N. (2018). Can 3-D printed gypsum samples replicate natural rocks? An experimental study. *Rock Mechanics and Rock Engineering*, 51(10), 3061–3074. <https://doi.org/10.1007/s00603-018-1520-3>

Laubach, S. E., Marrett, R., Olson, J. E., & Scott, A. R. (1998). Characteristics and origins of coal cleat: A review. *International Journal of Coal Geology*, 35(1–4), 175–207. [https://doi.org/10.1016/s0166-5162\(97\)00012-8](https://doi.org/10.1016/s0166-5162(97)00012-8)

- Lavoine, E., Davy, P., Darcel, C., & Munier, R. (2020). A discrete fracture network model with Stress-Driven nucleation: impact on clustering, connectivity, and topology. *Frontiers in Physics*, 8.
<https://doi.org/10.3389/fphy.2020.00009>
- Liu, L., Li, H., Chen, S., Shao, Z., Zhou, C., & Fu, S. (2021). Effects of bedding planes on mechanical characteristics and crack evolution of rocks containing a single pre-existing flaw. *Engineering Geology*, 293, 106325.
<https://doi.org/10.1016/j.enggeo.2021.106325>
- Long, J. C., Gilmour, P. W., & Witherspoon, P. (1985). A model for steady fluid flow in random Three-Dimensional networks of Disc-Shaped fractures. *Water Resources Research*, 21(8), 1105–1115.
<https://doi.org/10.1029/wr021i008p01105>
- Long, J. C., Remer, J., Wilson, C. R., & Witherspoon, P. (1982). Porous media equivalents for networks of discontinuous fractures. *Water Resources Research*, 18(3), 645–658. <https://doi.org/10.1029/wr018i003p00645>
- Ma, F., Sun, L. H., & Li, D. (2011). Numerical simulation analysis of covering rock strata as mining steep-inclined coal seam under fault movement. *Transactions of Nonferrous Metals Society of China*, 21, s556–s561.
[https://doi.org/10.1016/s1003-6326\(12\)61640-9](https://doi.org/10.1016/s1003-6326(12)61640-9)
- Ma, T., Xu, H., Guo, C., Fu, X., Liu, W., & Yang, R. (2020). A discrete fracture modeling approach for analysis of coalbed methane and water flow in a fractured coal reservoir. *Geofluids*, 2020, 1–15.
<https://doi.org/10.1155/2020/8845348>

- Meng, Z., Shi, X., & Li, G. (2016). Deformation, failure, and permeability of coal-bearing strata during longwall mining. *Engineering Geology*, 208, 69–80. <https://doi.org/10.1016/j.enggeo.2016.04.029>
- Meng, Z., Zhang, J., & Wang, R. (2011). In-situ stress, pore pressure and stress-dependent permeability in the Southern Qinshui Basin. *International Journal of Rock Mechanics and Mining Sciences*, 48(1), 122–131. <https://doi.org/10.1016/j.ijrmms.2010.10.003>
- Min, K., & Jing, L. (2004). Stress dependent mechanical properties and bounds of poisson's ratio for fractured rock masses investigated by a DFN-DEM technique. *International Journal of Rock Mechanics and Mining Sciences*, 41, 390–395. <https://doi.org/10.1016/j.ijrmms.2004.03.072>
- Moreno, L., Tsang, Y., Tsang, C., Hale, F., & Neretnieks, I. (1988). Flow and tracer transport in a single fracture: A stochastic model and its relation to some field observations. *Water Resources Research*, 24(12), 2033–2048. <https://doi.org/10.1029/wr024i012p02033>
- Niu, Q., Jiang, L., Li, C., Zhao, Y., Wang, Q., & Yuan, A. (2023). Application and prospects of 3D printing in physical experiments of rock mass mechanics and engineering: materials, methodologies and models. *International Journal of Coal Science & Technology/International Journal of Coal Science & Technology*, 10(1). <https://doi.org/10.1007/s40789-023-00567-8>
- Noack, K. (1998). Control of gas emissions in underground coal mines. *International Journal of Coal Geology*, 35(1–4), 57–82. [https://doi.org/10.1016/s0166-5162\(97\)00008-6](https://doi.org/10.1016/s0166-5162(97)00008-6)

- Paul, S., & Chatterjee, R. (2011). Determination of in-situ stress direction from cleat orientation mapping for coal bed methane exploration in south-eastern part of Jharia coalfield, India. *International Journal of Coal Geology*, 87(2), 87–96. <https://doi.org/10.1016/j.coal.2011.05.003>
- Quist, J., & Evertsson, M. (2016). Cone crusher modeling and simulation using DEM. *Minerals Engineering*, 85, 92–105. <https://doi.org/10.1016/j.mineng.2015.11.004>
- Shreedharan, S., & Kulatilake, P. H. (2015). Discontinuum–Equivalent continuum analysis of the stability of tunnels in a deep coal mine using the distinct element method. *Rock Mechanics and Rock Engineering*, 49(5), 1903–1922. <https://doi.org/10.1007/s00603-015-0885-9>
- Smith, L., & Schwartz, F. W. (1984). An analysis of the influence of fracture geometry on mass transport in fractured media. *Water Resources Research*, 20(9), 1241–1252. <https://doi.org/10.1029/wr020i009p01241>
- Song, G., Chugh, Y. P., & Wang, J. (2017). A numerical modeling study of longwall faces stability in mining thick coal seams in China. *International Journal of Mining and Mineral Engineering*, 8(1), 35. <https://doi.org/10.1504/ijmme.2017.082682>
- Song, G., Han, Y., Li, L., & Yang, Y. (2021). A study of coal cleats on longwall face stability in mining thick coal seams. *Arabian Journal of Geosciences*, 14(12). <https://doi.org/10.1007/s12517-021-07026-1>
- Tang, Q., Xie, W., Jing, S., Wang, X., & Su, Z. (2024). Experimental and Numerical Investigation on the Mechanical Behavior of Rock-Like Material

with Complex Discrete Joints. *Rock Mechanics and Rock Engineering*.
<https://doi.org/10.1007/s00603-024-03784-y>

Tang, Z. C., & Wong, L. N. Y. (2015). Influences of normal loading rate and shear velocity on the shear behavior of artificial rock joints. *Rock Mechanics and Rock Engineering*, 49(6), 2165–2172. <https://doi.org/10.1007/s00603-015-0822-y>

Van Nierop, M., Glover, G., Hinde, A., & Moys, M. (2001). A discrete element method investigation of the charge motion and power draw of an experimental two-dimensional mill. *International Journal of Mineral Processing*, 61(2), 77–92. [https://doi.org/10.1016/s0301-7516\(00\)00028-4](https://doi.org/10.1016/s0301-7516(00)00028-4)

Vardar, O., Zhang, C., Canbulat, I., & Hebblewhite, B. (2019). Numerical modelling of strength and energy release characteristics of pillar-scale coal mass. *Journal of Rock Mechanics and Geotechnical Engineering*, 11(5), 935–943. <https://doi.org/10.1016/j.jrmge.2019.04.003>

Wang, C., Zhang, J., Zang, Y., Zhong, R., Wang, J., Wu, Y., Jiang, Y., & Chen, Z. (2021). Time-dependent coal permeability: Impact of gas transport from coal cleats to matrices. *Journal of Natural Gas Science and Engineering*, 88, 103806. <https://doi.org/10.1016/j.jngse.2021.103806>

Wang, H., Shi, R., Lu, C., Jiang, Y., Deng, D., & Zhang, D. (2019). Investigation of sudden faults instability induced by coal mining. *Safety Science*, 115, 256–264. <https://doi.org/10.1016/j.ssci.2019.01.019>

Wang, J., & Park, H. (2002). Fluid permeability of sedimentary rocks in a complete stress-strain process. *Engineering Geology*, 63(3–4), 291–300.
[https://doi.org/10.1016/s0013-7952\(01\)00088-6](https://doi.org/10.1016/s0013-7952(01)00088-6)

- Wang, P., Jiang, L., Li, X., Qin, G., & Wang, E. (2018). Physical simulation of mining effect caused by fault tectonics. *Arabian Journal of Geosciences*, 11(23). <https://doi.org/10.1007/s12517-018-4088-z>
- Wang, S., Elsworth, D., & Liu, J. (2013). Permeability evolution during progressive deformation of intact coal and implications for instability in underground coal seams. *International Journal of Rock Mechanics and Mining Sciences*, 58, 34–45. <https://doi.org/10.1016/j.ijrmms.2012.09.005>
- Wang, X., & Cai, M. (2019). A DFN–DEM multi-scale modeling approach for simulating tunnel excavation response in jointed rock masses. *Rock Mechanics and Rock Engineering*, 53(3), 1053–1077. <https://doi.org/10.1007/s00603-019-01957-8>
- Wu, Q., Wu, Q., Yuan, A., & Wu, Y. (2020). Analysis of mining effect and fault stability under the influence of normal faults. *Geotechnical and Geological Engineering*, 39(1), 49–63. <https://doi.org/10.1007/s10706-020-01400-8>
- Wu, Z., Zhang, B., Weng, L., Liu, Q., & Wong, L. N. Y. (2019). A new way to replicate the highly stressed soft rock: 3D printing exploration. *Rock Mechanics and Rock Engineering*, 53(1), 467–476. <https://doi.org/10.1007/s00603-019-01926-1>
- Xu, N., Zhang, J., Tian, H., Mei, G., & Ge, Q. (2016). Discrete element modeling of strata and surface movement induced by mining under open-pit final slope. *International Journal of Rock Mechanics and Mining Sciences*, 88, 61–76. <https://doi.org/10.1016/j.ijrmms.2016.07.006>
- Xu, X., Sarmadivaleh, M., Li, C., Xie, B., & Iglauer, S. (2016). Experimental study on physical structure properties and anisotropic cleat permeability

estimation on coal cores from China. *Journal of Natural Gas Science and Engineering*, 35, 131–143. <https://doi.org/10.1016/j.jngse.2016.08.050>

Yavuz, H. (2004). An estimation method for cover pressure re-establishment distance and pressure distribution in the goaf of longwall coal mines. *International Journal of Rock Mechanics and Mining Sciences*, 41(2), 193–205. [https://doi.org/10.1016/s1365-1609\(03\)00082-0](https://doi.org/10.1016/s1365-1609(03)00082-0)

Zhang, Q., & Zhao, J. (2013). A review of dynamic experimental techniques and mechanical behaviour of rock materials. *Rock Mechanics and Rock Engineering*, 47(4), 1411–1478. <https://doi.org/10.1007/s00603-013-0463-y>

Zhang, X., Jiang, Y., Wang, G., Liu, J., Wang, D., Wang, C., & Sugimoto, S. (2018). Mechanism of shear deformation, failure and energy dissipation of artificial rock joint in terms of physical and numerical consideration. *Geosciences Journal*, 23(3), 519–529. <https://doi.org/10.1007/s12303-018-0043-y>

Zhao, J., Xiao, J., Lee, M. L., & Ma, Y. (2016). Discrete element modeling of a mining-induced rock slide. *SpringerPlus*, 5(1). <https://doi.org/10.1186/s40064-016-3305-z>

Zhao, L., Jin, X., & Liu, X. (2020). Numerical research on wear characteristics of drum based on discrete element method (DEM). *Engineering Failure Analysis*, 109, 104269. <https://doi.org/10.1016/j.engfailanal.2019.104269>

Zhao, Y., Song, H., Liu, S., Zhang, C., Dou, L., & Cao, A. (2019). Mechanical anisotropy of coal with considerations of realistic microstructures and external loading directions. *International Journal of Rock Mechanics and*

Mining Sciences, 116, 111–121.

<https://doi.org/10.1016/j.ijrmms.2019.03.005>

Zhou, A., Hu, J., Wang, K., & Du, C. (2023). Analysis of fault orientation and gas migration characteristics in front of coal mining face: Implications for coal-gas outbursts. *Process Safety and Environmental Protection*, 177, 232–245.
<https://doi.org/10.1016/j.psep.2023.07.011>

Zhou, T., & Zhu, J. (2017). Identification of a suitable 3D printing material for mimicking brittle and hard rocks and its brittleness enhancements. *Rock Mechanics and Rock Engineering*, 51(3), 765–777.
<https://doi.org/10.1007/s00603-017-1335-7>

Zhu, J., Zhou, T., Liao, Z., Sun, L., Li, X., & Chen, R. (2018). Replication of internal defects and investigation of mechanical and fracture behaviour of rock using 3D printing and 3D numerical methods in combination with X-ray computerized tomography. *International Journal of Rock Mechanics and Mining Sciences*, 106, 198–212.
<https://doi.org/10.1016/j.ijrmms.2018.04.022>

APPENDICES

A. Analysis of Minor Principal Stresses from the History Points Located at Overburden (30 m high on the overburden) in Different Scenarios

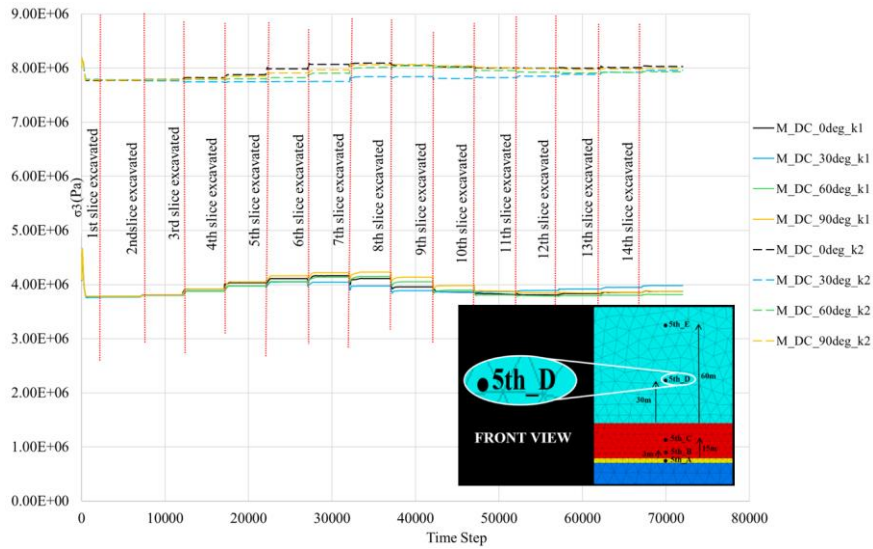


Figure A.1 Comparison of σ_3 values (Pa) from the history point located above the 5th coal slice - 30 m high on the overburden (5th_D) in different discontinuous cases

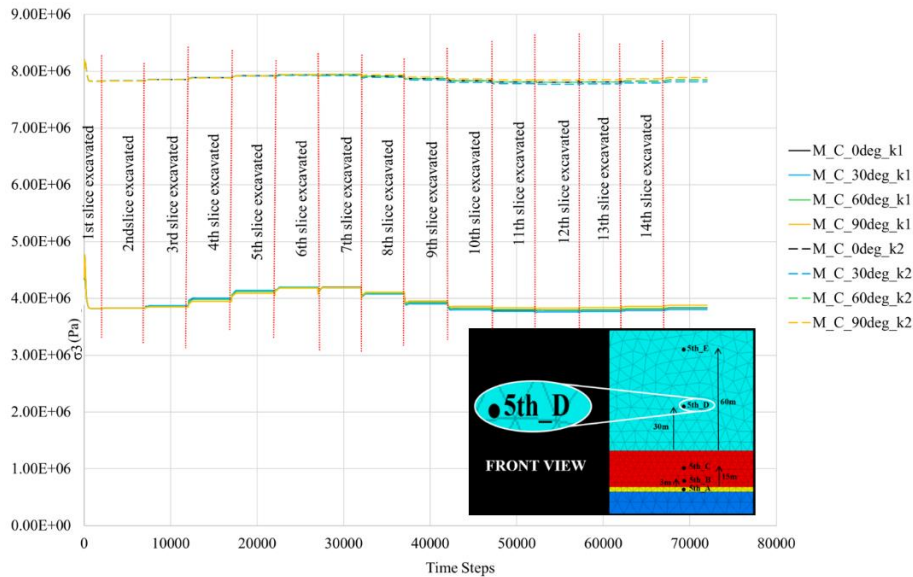


Figure A.2 Comparison of σ_3 values (Pa) from the history point located above the 5th coal slice - 30 m high on the overburden (5th_D) in different continuous cases

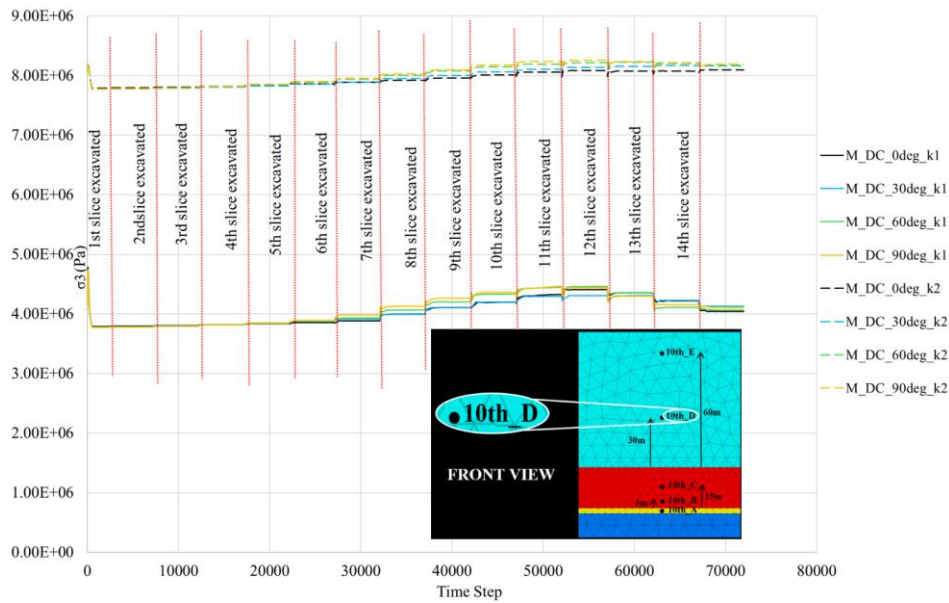


Figure A.3 Comparison of σ_3 values (Pa) from the history point located above the 10th coal slice - 30 m high on the overburden (10th_D) in different discontinuous cases

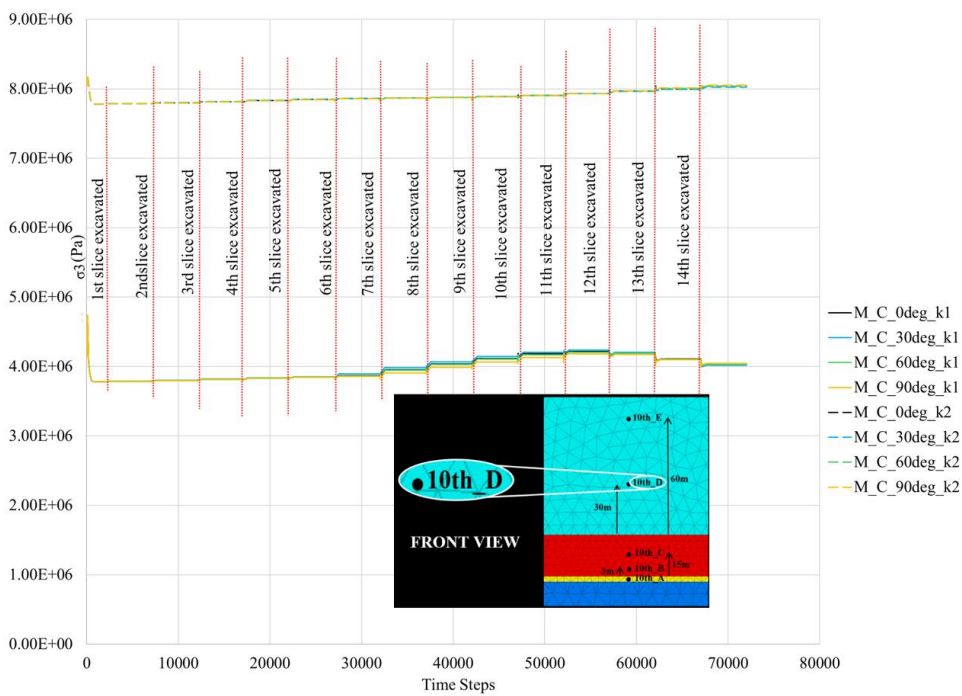


Figure A.4 Comparison of σ_3 values (Pa) from the history point located above the 10th coal slice - 30 m high on the overburden (10th_D) in different continuous cases

B. Analysis of Minor Principal Stresses from the History Points Located at Overburden (60 m high on the overburden) in Different Scenarios

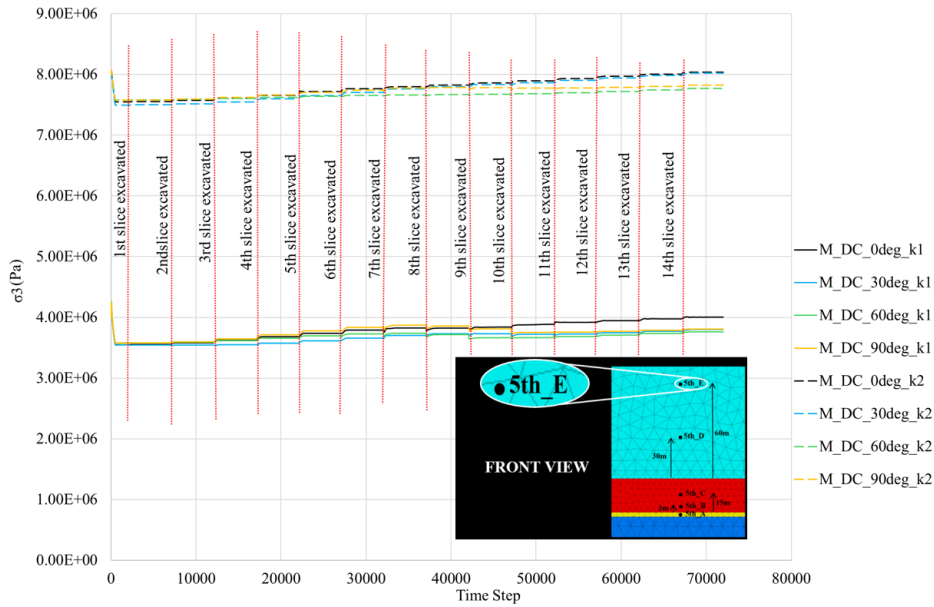


Figure B.1 Comparison of σ_3 values (Pa) from the history point located above the 5th coal slice - 60 m high on the overburden (5th_E) in different discontinuous cases

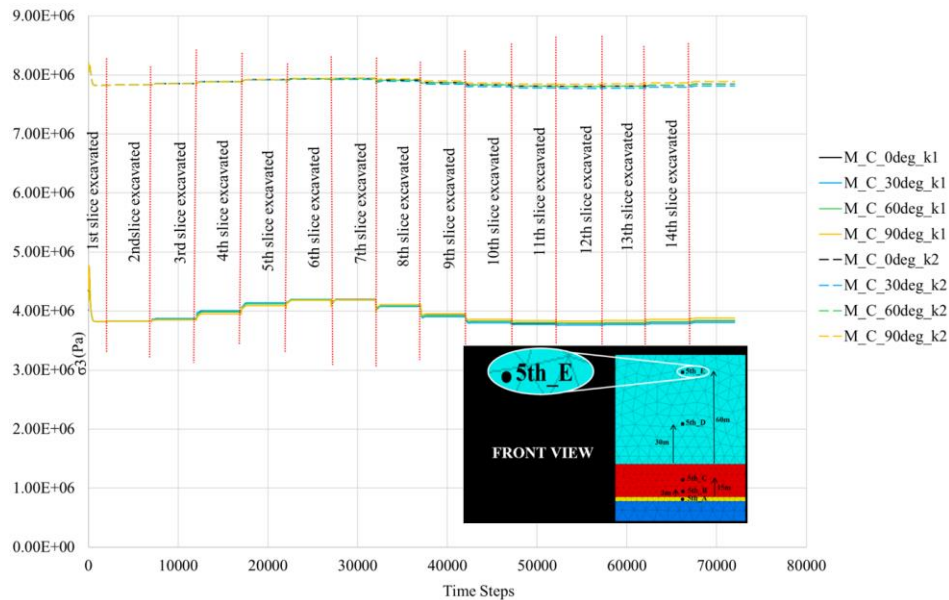


Figure B.2 Comparison of σ_3 values (Pa) from the history point located above the 5th coal slice - 60 m high on the overburden (5th_E) in different continuous cases

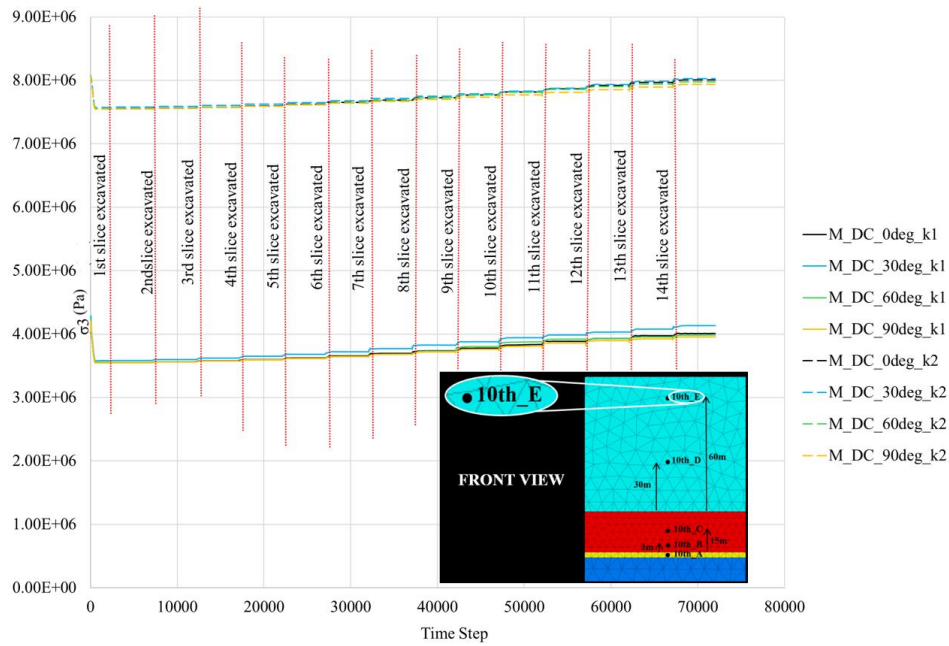


Figure B.3 Comparison of σ_3 values (Pa) from the history point located above the 10th coal slice - 60 m high on the overburden (10th_E) in different discontinuous cases

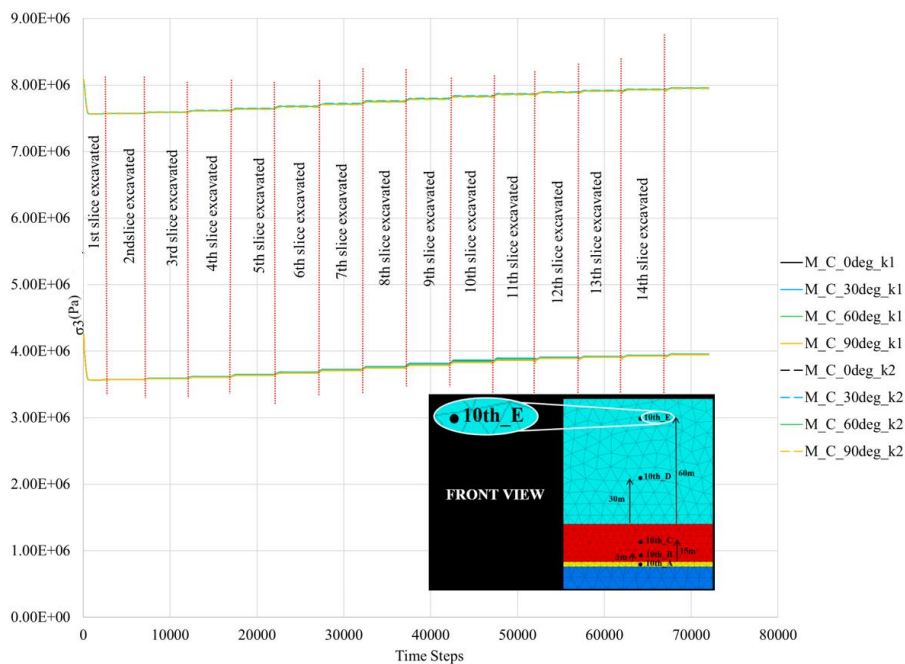


Figure B.4 Comparison of σ_3 values (Pa) from the history point located above the 10th coal slice - 60 m high on the overburden (10th_E) in different continuous cases